TECHNISCHE UNIVERSITÄT WIEN

Diplomarbeit

On Multiphase Flow and the Dynamic Temperature Distribution in Proton Exchange Membrane Fuel Cells

zum Zwecke der Erlangung des akademischen Grades eines
Diplom-Ingenieurs

ausgeführt am
Institut für Strömungsmechanik und Wärmeübertragung
der Technischen Universtität Wien

durch
Florian Altmann
Mat.Nr.: 51831288

unter der Leitung von
Ao.Univ.Prof. Dipl.-Ing. Dr.techn. Stefan Braun

Wien, 30. März 2022

Florian Altmann

Stefan Braun

Danksagung

Ich möchte mich an dieser Stelle bei all jenen Menschen bedanken, die mich bei der Erstellung dieser Arbeit unterstützt und motiviert haben.

Zuerst gebührt mein Dank den Herren Prof. Dr. Stefan Braun, Dr. Dominik Murschenhofer und DI Dominik Kuzdas, die diese Diplomarbeit so engagiert betreut haben und immer, bei allen Fragen und Nöten erreichbar waren. Danke für das Vertrauen und Interesse, das mir und meiner Arbeit entgegengebracht wurde, für die mir gebotenen Freiräume, für die intensiven Diskussionen und das gemeinsame Streben. Die Zusammenarbeit hat große Freude gemacht und war unheimlich inspirierend. Herzlichen Dank dafür!

Weiters möchte ich mich bei Fani dafür bedanken, dass sie die, für sie völlig fachfremde Diplomarbeit, Korrektur gelesen hat und viele wichtige Bemerkungen zur sprachlichen Gestaltung beisteuerte.

Besonders inniger Dank gilt meiner Freundin Leni, für ihre Ausdauer, für ihren Beistand in schwierigen Phasen, fürs Zuhören und Motivieren. Die gemeinsame Zeit hat mir wahnsinnig viel Kraft gegeben. Danke fürs immer da sein!

Nicht zuletzt möchte ich mich bei meinen Eltern, Edith und Hans, bedanken. Sie haben mich in jeder nur erdenklichen Hinsicht unterstützt und motiviert. Ohne sie wäre mein Studium und diese Arbeit nicht möglich gewesen.

Abstract

Proton Exchange Membrane Fuel Cells (PEMFCs) are a promising alternative power source for mobile and stationary devices. Their dynamic operation, however, is still very challenging, since unmeant destructive states reduce durability and uncontrolled formation of liquid water in the porous electrodes affects fuel cell performance. The prediction of the spatio-temporal temperature and gas distribution within the PEMFC is crucial in both cases. Therefore, a dynamic multiphase flow extension to the linearised in time (LIT) model by Murschenhofer et al. [1] is proposed in this work. For each domain the governing differential equations are derived from 3D integral conservation laws following a quasi-2D approach. Effects such as convective and diffusive transport of mass, heat and enthalpy, as well as heat generation by electrochemical half-reactions, finite proton conductivity in the membrane and phase change are considered.

The non-isothermal single phase case of the model is further implemented in Matlab®. Application of a Chebyshev spectral collocation method, linearisation of the nonlinear governing equations with respect to the previous time step, and using adaptive time stepping, assures fast computation. The extended model is validated in terms of predicted temperature distributions versus 3D steady-state simulations from existing literature. The dynamic thermal behavior due to prescribed steep time gradients in current density and relative humidity is found to be in good qualitative agreement with results published by other authors. With its very low computational cost, the presented model is especially developed for comprehensive parameter studies, control unit adjustments or state predicitons.

Kurzfassung

Polymerelektrolytmembran-Brennstoffzellen (PEMFCs) sind eine vielversprechende alternative Energiequelle für ortsfeste und mobile Anwendungszwecke. Der dynamische Betrieb erweist sich jedoch als schwierig, da gewisse Zustände Schädigungen in der Zelle herbeiführen können, die die Lebensdauer und Leistung beeinträchtigen. Die unkontrollierte Bildung von Flüssigwasser kann die Leistungsabgabe der Brennstoffzelle weiter reduzieren. In beiden Fällen ist die Vorhersage der zeitlichen und räumlichen Gas- und Temperaturverteilung entscheidend.

Diese Arbeit präsentiert daher eine Mehrphasenerweiterung zum Linarised-in-Time (LIT) Modell von Murschenhofer et al. [1]. Die differentielle Form der Modellgleichungen werden einem quasi-2D Ansatz folgend aus den integralen 3D Erhaltungssätzen hergeleitet. Berücksichtigt werden unter anderem der konvektive und diffusive Masse-, Wärme- und Enthalpietransport, sowie die Wärmeentwicklung durch elektrochemische Halbzellenreaktionen, endliche Protonenleitfähigkeit in der Membran und Phasenumwandlung.

Der Spezialfall nichtisothermer Einphasenströmung wird im Anschluss in Matlab® implementiert. Die nichtlinearen Modellgleichungen werden dafür mit Bezug auf den vorhergehenden Zeitschritt linearisiert. Die räumliche Diskretisierung erfolgt mittels Tschebyscheff Spektralmethoden. Durch die Verwendung eines variablen Zeitschritts kann die Rechenzeit weiters erheblich minimiert werden. Die Modellvalidierung für stationäre Temperaturverteilungen erfolgt gegen Ergebnisse hochauflösender 3D Simulationen aus bestehender Literatur. Das dynamische Verhalten bei Vorgabe von starken zeitlichen Änderungen der Stromdichte und relativen Einlassfeuchtigkeit zeigt weiters gute qualitative Übereinstimmung mit Resultaten aus anderen Publikationen. Aufgrund des sehr geringen Rechenaufwands eignet sich das vorgestellte Modell besonders für Parameterstudien, zur Anpassung von Regeleinheiten oder zur Zustandsvorhersage.

Contents

Nomenclature

Generally, bold faces and superscript tilde denote vector and dimensional quantities, respectively.

Latin symbols

$\tilde{\mathrm{EW}}$	equivalent weight [$\mathrm{kg\,mol^{-1}}$]
$\tilde{\boldsymbol{f}}$	volumetric force [$\mathrm{kg\,m^{-2}\,s^{-2}}$]
$\tilde{\boldsymbol{j}}$	diffusion flux [$\mathrm{kg\,m^{-2}\,s^{-1}}$]
$\tilde{\boldsymbol{q}}$	heat flux [$\mathrm{W\,m^{-2}}$]
$\tilde{\boldsymbol{r}}$	enthalpy diffusion flux [$\mathrm{W\,m^{-2}}$]
$\tilde{\boldsymbol{u}}$	velocity [$\mathrm{m\,s^{-1}}$]
$\tilde{\boldsymbol{w}}$	drift velocity [$\mathrm{m\,s^{-1}}$]
$\tilde{a}_{\mathrm{C}}\tilde{L}_{\mathrm{C}}$	electrode roughness, meaning catalyst surface area per electrode geometric area [-]
$\tilde{c}_{\mathrm{p}}$	isobaric specific heat capacity [$\mathrm{J\,kg^{-1}\,K^{-1}}$]
$\tilde{E}$	electric potential [V]
$\tilde{G}$	Gibbs free energy [$\mathrm{J\,mol^{-1}}$]
$\tilde{H}$	height [m]
$\tilde{i}$	current density [$\mathrm{A\,m^{-2}}$]
$\tilde{i}_0$	exchange current density [$\mathrm{A\,m^{-2}}$]
$\tilde{J}_k^{\alpha}$	interphase species transfer [$\mathrm{kg\,m^{-3}\,s}$]
$\tilde{k}$	thermal conductivity [$\mathrm{W\,m^{-1}\,K}$]
$\tilde{L}$	gas channel length [m]
$\tilde{M}$	molar mass [$\mathrm{kg\,mol^{-1}}$]
$\tilde{p}$	pressure [Pa]
$\tilde{p}_{\mathrm{c}}$	capillary pressure [Pa]
$\tilde{Q}$	heat source/sink [$\mathrm{J\,mol^{-1}}$], [$\mathrm{J\,kg^{-1}}$], [$\mathrm{W\,mol^{-1}}$], [$\mathrm{W\,kg^{-1}}$]
$\tilde{R}_{\mathrm{c}}$	thermal contact resistance [$\mathrm{m^2\,K\,W^{-1}}$]
$\tilde{R}_{\mathrm{PEM}}$	membrane proton resistance [Ω]
$\tilde{S}$	entropy [$\mathrm{J\,mol^{-1}\,K}$]

$\tilde{T}$	absolute temperature [K]
$\tilde{t}$	time [s]
$\tilde{V}$	volume [m^3]
$\tilde{W}$	width [m]
$\tilde{W}_{\mathrm{el}}$	electric work [J]
$\boldsymbol{n}$	normal unit vector [-]
a_{w}	water activity [-]
C_{drag}	electro-osmotic drag coefficient [-]
f	fitting factor [-]
$J(s)$	Leverett J-function [-]
K	dimensionless group [-]
N	number of computational nodes [-]
n	number of electrons per molecule [-], time step [-]
s	phase saturation [-]
$\tilde{h}$	specific enthalpy [$\mathrm{J\,kg^{-1}}$]

Greek symbols

α	time step ratio [-]
α_i	transfer coefficient for electrode i [-]
χ	volume fraction [-]
Δ	difference, e.g. change of enthalpy
γ	correction factor [-]
γ_{C}	pressure dependency factor for chemical reaction [-]
ι	stoichiometric factor [-]
κ_{r}	relative permeability [-]
λ	normalised membrane water content [-]
θ_{c}	contact angle [-]
$\tilde{\alpha}$	convective heat transfer coefficient [$\mathrm{W\,m^{-2}\,K^{-1}}$]
$\tilde{\eta}$	overpotential [V]

$\tilde{\Gamma}$	general source term
$\tilde{\kappa}$	permeability of the porous medium [m^2]
$\tilde{\mu}$	dynamic viscosity [Pa s]
$\tilde{\nu}$	kinematic viscosity [$m^2\,s^{-1}$]
$\tilde{\rho}\tilde{\phi}$	general density
$\tilde{\rho}\tilde{\Psi}$	general force
$\tilde{\Sigma}$	general flux
$\tilde{\sigma}_{\mathrm{PEM}}$	membrane proton conductivity [$S\,m^{-1}$]
$\tilde{\theta}$	general mass flow density
$\tilde{\varsigma}$	surface tension [$kg\,s^{-2}$]
$\tilde{\boldsymbol{\psi}}$	capillary diffusion flux [$kg\,m^{-2}\,s^{-1}$]
$\tilde{\boldsymbol{\sigma}}, \tilde{\boldsymbol{\sigma}}'$	stress tensor, deviatoric stress tensor [Pa]
ε	porosity [-]
ζ	relative mobility [-]

Miscellaneous

$\Delta\tilde{H}$	change of enthalpy [$J\,mol^{-1}$]
$\tilde{\dot{m}}$	mass transfer rate [$kg\,m^{-3}\,s^{-1}$]
$\tilde{\mathcal{D}}$	diffusion coefficient [$m^2\,s^{-1}$]
$\tilde{\mathcal{E}}$	phase interaction power [W]
$\tilde{\mathcal{L}}$	mechanical power [W]
$\tilde{\mathcal{Q}}$	heat power [W]
$\tilde{\mathcal{S}}$	surface of discontinuity [m^2]

Subscripts and superscripts

α	species α, cathode: O_2, N_2, H_2O, anode: H_2, N_2, H_2O
β	reactant β, cathode: O_2, anode: H_2
k	phase k
*	fitted variable
act	activation

amb	ambient
eff	effective
el	electric
f	formation
g	gas phase
irr	irreversible
l	liquid phase
lv, vl	liquid to vapour (evaporation), vapour to liquid (condensation)
reac	chemical reaction
s	solid phase (GDL matrix)
sat	saturation
sorp	sorption
tot	total
w	water

Abbreviations

e^-	electron
H_2O	water
H_2	hydrogen
H^+	proton
N_2	nitrogen
O_2	oxygen
Pt	platinum
A, ANO	anode
BP	bipolar plate
C, CAT	cathode
CCL	cathode catalyst layer
CL	catalyst layer
COP	coefficient of performance

CV	control volume
EB	energy balance
EOM	equation of motion
EOS	equation of state
FC	fuel cell
GC	gas channel
GDL	gas diffusion layer
HFM	homogeneous flow model
LHS	left hand side
LIT	linearised in time
LMB	liquid phase mass balance
MEA	membrane electrode assembly
MMM	multiphase mixture model in capillary porous media
OC	open circuit
PDE	partial differential equation
PEM	proton exchange membrane
PEMFC	proton exchange membrane fuel cell
PMB	partial mass balance
RH	relative humidity
RHS	right hand side
SL	inner slice
TCR	thermal contact resistance
TMB	total mass balance

Physical constants

$\tilde{\mathcal{R}} = 8.314\,\mathrm{J\,mol^{-1}\,K^{-1}}$, gas constant

$\tilde{F} = 96\,485.34\,\mathrm{C\,mol^{-1}}$, Faraday constant

$\tilde{N}_\mathrm{A} = 6.022 \times 10^{23}\,\mathrm{mol^{-1}}$, Avogadro's constant

$\tilde{q}_\mathrm{el} = 1.6021 \times 10^{-19}\,\mathrm{C}$, elementary charge

1
Introduction

Proton exchange membrane fuel cells (PEMFCs) are a promising power source for mobile and stationary devices. Their high energy density and high efficiency are the main advantages, low operating noise and the relative simplicity due to no moving parts are further convenient properties. When hydrogen (H_2) from low emission sources is used as fuel, PEMFCs are a climate friendly electricity generation alternative and can help to further establish green mobility and improve the handling of demand/supply fluctuations in an electrical grid.

In recent years, fundamental knowledge about fuel cell (FC) operating conditions has been gained through both experimental and theoretical work. However, operating FCs dynamically is still very challenging. The issue of reduced durability and performance caused by unmeant destructive operating states or adverse water management is hardly tackled successfully. On the one hand, the catalyst layers (CLs) and proton exchange membrane (PEM) have to be sufficiently moistened to avoid dehydration and damaging, on the other hand, water flooding must be prevented in order to keep FC performance stable. For both, successful water management and the prevention of material damaging, the dynamic temperature distribution in the membrane electrode assembly (MEA) is of key interest, [2].

To further establish PEMFCs as an alternative power source, the challenges of dynamic operation conditions have to be overcome. This makes it necessary to investigate and understand transient fuel cell behaviour caused by numerous complex and coupled physio-chemical phenomena, such as

- convective and diffusive reactant gas transport,
- electrochemical reactions,
- generation, accumulation and conduction of heat,
- formation and transport of liquid water,
- alternation of load and FC cooling.

To this end, a physical-mathematical FC model with minimum computation time is desirable to perform widespread parameter studies and to design necessary FC testing strategies. Such a model can further be used for FC control unit adjustments and online monitoring.

Murschenhofer et al. [1] presented a real-time capable quasi-2D PEMFC model that considers effects such as multicomponent diffusion in porous layers, membrane water transport driven by diffusion and electro-osmotic drag as well as membrane nitrogen crossover forced by partial pressure differences. The governing equations are linearised with respect to the previous time step to avoid numerically expensive Newton iterations. A solution method based on Chebyshev collocation minimises the required nodes and assures fast computation.

Based on their work a non-isothermal multiphase flow model is developed in this thesis to gain deeper insights into dynamic FC behaviour. The aim is to find a more general multiphase formulation of the governing equations which still only requires low computational resources and contains

the single phase formulation as a special case, as well as to bridge the gap between numerically expensive, highly complex 3D models and fast 0D/1D models which lack spatial resolution.

On the outset of this work a general description of the functional principle and thermodynamics of a PEMFC is given following [3]. The main sources of heat, relevant for the dynamic temperature distribution in the cell, are further discussed.

1.1 Functional principle of a PEMFC

At the heart of a PEMFC is a polymer electrolyte membrane (PEM) which is squeezed between two porous, electrically conductive electrodes. The PEM is almost impermeable to gases but takes up water in a dissolved/liquid state and conducts protons. The electrodes are made of carbon cloth or carbon fiber paper. At the interface to the PEM the carbon is coated with Platinum (Pt) which serves as a catalyst. This very thin layer is the catalyst layer (CL) where the electrochemical reactions take place.

Gaseous H_2 is fed through the porous electrodes, so called gas diffusion layers (GDLs), on the anode side of the PEMFC until it reaches the CL where it splits up into its constituents - protons and electrons. This is the oxidation reaction

$$H_2 \rightarrow 2\,H^+ + 2\,e^-\,. \tag{1.1}$$

Protons travel through the PEM while electrons travel in the other direction, through the electrode GDL to the bipolar plate (BP). Via an outside electric circuit the electrons perform electric work and reach the other side (cathode) BP, then GDL and finally CL.

Through the cathode electrode, gaseous oxygen (O_2) is fed to the CL. Together with the electrons coming from the outside electric circuit and the protons coming from the membrane, pure water (H_2O) is formed. This is the reduction reaction

$$\frac{1}{2}\,O_2 + 2\,H^+ + 2\,e^- \rightarrow H_2O\,. \tag{1.2}$$

Reduction and oxidation half-cell reactions on the anode and cathode side, respectively, run simultaneously and result in the overall reaction

$$\frac{1}{2}\,O_2 + H_2 \rightarrow H_2O\,, \tag{1.3}$$

which generates a continuous electric current. Hence, a FC is an electrochemical energy converter which converts the chemical energy of fuel directly into electric energy. To generate sufficient electrical power, several single cells are connected to form a FC stack. Such a PEMFC stack and the involved reactants to generate an electric current are depicted schematically in fig. 1.

The cathode side reactant gas O_2 is typcially fed to the system as a constituent of humidified air. Hence and due to the production of water, a multicomponent gas mixture of O_2, N_2 and H_2O, is found in the PEMFC cathode. H_2 is also fed in humidified form to the anode side to increase FC performance. As N_2 and H_2O are transported through the PEM, a mixture of H_2, N_2 and H_2O is found on the anode side. Depending on the thermodynamic condition present in the different PEMFC domains, liquid water is to be formed or evaporated. Once the pores in the GDL and CL are filled with liquid water, reactant gas transport is hindered and the CL reaction surface area decreases, which results in an overall FC performance drop. This effect is referred to as water flooding.

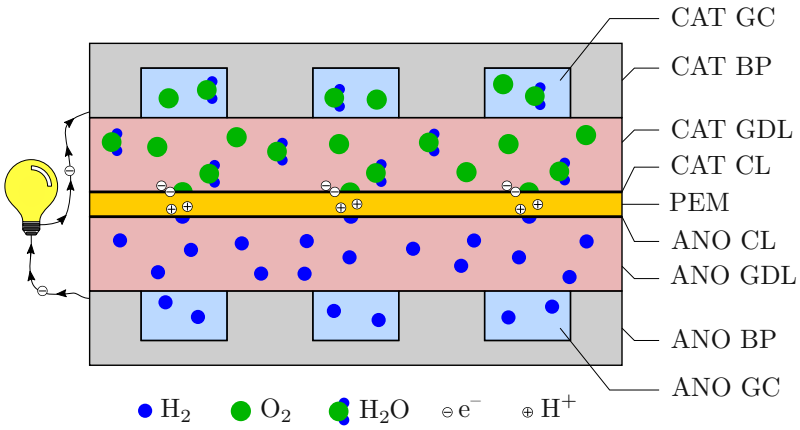

Figure 1: PEMFC schematic.

Water flooding also occurs in the gas channels (GCs). The GCs are inserted into the BPs sitting on top of the GDLs and distribute the reactant gases over the whole membrane electrode assembly (MEA). The BPs not only collect the generated electrical current, but also conduct the released heat within the PEMFC to the cooling system attached on top. The main portion of the total heat flux is directly transferred via the BP-GDL interface, while a small fraction takes the detour over the GC before it is finally collected by the BP.

1.2 PEMFC thermodynamics

Enthalpy and entropy of reaction

The overall PEMFC reaction (1.3) is an exothermic process as the combustion of H_2, but its constituting half-cell reactions take place spatially separated. In contrast to combustion, this allows the direct conversion of released chemical reaction energy into electrical work.

The enthalpy of a chemical reaction $\Delta_{\text{reac}}\tilde{H}$ is the difference between the enthalpy of formation $\Delta_{\text{f}}\tilde{H}$ of products and reactants. For the PEMFC or H_2 combustion reaction this means

$$\Delta_{\text{reac}}\tilde{H} = \Delta_{\text{f}}\tilde{H}(\text{H}_2\text{O}) - \Delta_{\text{f}}\tilde{H}(\text{O}_2) - \Delta_{\text{f}}\tilde{H}(\text{H}_2)\,. \tag{1.4}$$

Similarly the reaction entropy $\Delta_{\text{reac}}\tilde{S}$, corresponding to the reversible entropy production, is defined as the difference between the formation entropies $\Delta_{\text{f}}\tilde{S}$ of products and reactants

$$\Delta_{\text{reac}}\tilde{S} = \Delta_{\text{f}}\tilde{S}(\text{H}_2\text{O}) - \Delta_{\text{f}}\tilde{S}(\text{O}_2) - \Delta_{\text{f}}\tilde{S}(\text{H}_2)\,. \tag{1.5}$$

The values of $\Delta_{\text{f}}\tilde{H}$ and $\Delta_{\text{f}}\tilde{S}$ for the PEMFC's reactant gases are shown in table 1. By definition the enthalpy of formation of the elements is equal to zero. Therefore, evaluation of equation (1.4) yields $\Delta_{\text{f}}\tilde{H}(l) = -286.02\,\text{kJ mol}^{-1}$ for the formation of liquid water. The minus sign, by convention, indicates an exothermic process as energy is released by the reaction. If not liquid, but gaseous water is produced in the reaction, the reaction enthalpy decreases to $\Delta_{\text{f}}\tilde{H}(g) = -241.98\,\text{kJ mol}^{-1}$. The difference between $\Delta_{\text{f}}\tilde{H}(l)$ and $\Delta_{\text{f}}\tilde{H}(g)$ is the heat of evaporation of water $\Delta_{\text{lv}}\tilde{H} = 44.04\,\text{kJ mol}^{-1}$, [3].

	$\Delta_f \tilde{H}$ [kJ mol^{-1}]	$\Delta_f \tilde{S}$ [kJ mol^{-1} K^{-1}]
O_2	0	0.13066
H_2	0	0.20517
liquid H_2O	-286.02	0.06996
vapour H_2O	-241.98	0.18884

Table 1: Enthalpies and entropies of formation for PEMFC reactants and products at $\tilde{T}_0 = 25\,°C$ and $\tilde{p} = 1\,\text{bar}$, [3].

Theoretical electrical work and FC potential

There are losses in the conversion of reaction enthalpy into electrical work due to the creation of entropy $\Delta_{reac}\tilde{S}$. The portion of reaction enthalpy that can be converted into electricity corresponds to the Gibbs free energy

$$\Delta_{reac}\tilde{G} = \Delta_{reac}\tilde{H} - \tilde{T}\,\Delta_{reac}\tilde{S}\,. \tag{1.6}$$

Therefore, at $\tilde{T}_0 = 25\,°C$ and $\tilde{p} = 1\,\text{bar}$, out of $286.02\,\text{kJ mol}^{-1}$ of available energy, $237.34\,\text{kJ mol}^{-1}$ can be converted into electrical energy. The remaining $48.68\,\text{kJ mol}^{-1}$ are converted into heat. If no other (irreversible) losses appear in the PEMFC a maximum theoretical efficiency factor (COP) can be calculated by

$$\text{COP}_{max} = \frac{\Delta_{reac}\tilde{G}}{\Delta_{reac}\tilde{H}} = 83\,\%\,. \tag{1.7}$$

The total electrical charge transferred in a FC reaction per mol of H_2 consumed is equal to

$$q_{el,tot} = n\tilde{N}_A\tilde{q}_{el} = n\tilde{F}\,. \tag{1.8}$$

Here, $n = 2$ is the number of electrons per molecule of H_2, $\tilde{N}_A$ is Avogadro's constant and $\tilde{q}_{el}$ is the elementary charge. The latter two can be combined to form Faraday's constant $\tilde{F}$.

Electrical work is the product of charge and electric potential $\tilde{E}$. Hence, the maximum electrical work per consumed mol of H_2 in a PEMFC is

$$\tilde{W}_{el} = n\tilde{F}\tilde{E}\,. \tag{1.9}$$

As mentioned before, $\Delta_{reac}\tilde{G}$ corresponds to the maximum amount of electrical energy generated in a PEMFC. The theoretical potential of a FC then can be calculated by

$$\tilde{E}_{OC} = \frac{\Delta_{reac}\tilde{G}}{n\tilde{F}} = 1.23\,\text{V}\,. \tag{1.10}$$

1.3 PEMFC losses and heat sources

Half-cell reactions

As mentioned previously, not all of the chemical energy is converted into electricity due to the creation of entropy by reversible processes, but is released as reaction heat. This is quantified by

$$\tilde{Q}_{reac} = -\tilde{T}\,\Delta_{reac}\tilde{S}\,. \tag{1.11}$$

However, for accurately mapping FC behaviour, it is necessary to attribute heat sources precisely to their origin, in this case half-cell reaction. Total cell reaction entropy defined in equation

(1.5) is the sum of the anode and cathode half-cell reaction entropies $\Delta^{\mathrm{A}}_{\mathrm{reac}}\tilde{S}$ and $\Delta^{\mathrm{C}}_{\mathrm{reac}}\tilde{S}$, respectively. Ramousse et al. [4] point out that in contrast to the well known total reaction entropy of $\Delta_{\mathrm{reac}}\tilde{S} = -163.2\,\mathrm{J\,mol^{-1}\,K^{-1}}$ at $\tilde{T} = 353\,\mathrm{K}$ and $\tilde{p} = 1\,\mathrm{bar}$, values for the half-cell reaction entropies vary substantially in different publications. Table 2 summarises these discrepancies. Due to the lack of reliable data, the anodic half-cell reaction is often assumed to be isothermal, $\tilde{Q}^{\mathrm{A}}_{\mathrm{reac}} = 0$. Consequently, the entropy of water production is fully attributed to the cathode half-cell reaction.

Publication	$\Delta_{\mathrm{reac}}\tilde{S}^{\mathrm{A}}$ [$\mathrm{J\,mol^{-1}\,K^{-1}}$]	$\Delta_{\mathrm{reac}}\tilde{S}^{\mathrm{C}}$ [$\mathrm{J\,mol^{-1}\,K^{-1}}$]
1	-133.2	-30
2	-42.5	-120.7
3	0.104	-163.304
4	69.1	-232.3
5	84.7	-247.9
Calculation by [4]	-226.0	62.8

Table 2: Half-cell reaction entropies from different publications summarised in [4].

The heat fluxes generated by the half-cell reaction j under reversible conditions depend on the cell current density $\tilde{i}$ and are given by

$$\tilde{q}^{j}_{\mathrm{reac}} = -\tilde{T}\,\Delta^{j}_{\mathrm{reac}}\tilde{S}\,\frac{\tilde{i}}{2\tilde{F}}\,. \tag{1.12}$$

Electrochemical activation of reactions

Additional to the losses from reversible processes in the electrochemical half-cell reactions, irreversibilities are responsible for a part of the energy degradation which is converted into heat, [4],

$$\tilde{Q}^{j}_{\mathrm{irr}} = -\tilde{T}\,\Delta^{j}_{\mathrm{irr}}\,\tilde{S}\,. \tag{1.13}$$

These irreversibilities generate overpotentials $\tilde{\eta}^{j}$ at the electrodes and depend on current density, geometrical parameters and properties of the reactants, such as temperature, pressure and concentration. They are calculated from the Butler-Volmer equation, or can be approximated with the Tafel equation, [3],

$$\tilde{\eta}^{j} = \frac{\tilde{\mathcal{R}}\tilde{T}}{\alpha_j\tilde{F}}\ln\left(\frac{\tilde{i}}{\tilde{i}_0}\right), \tag{1.14}$$

where $\tilde{\mathcal{R}}$ is the gas constant, α_j is the transfer coefficient and $\tilde{i}_0$ is the exchange current density. Because of the more sluggish oxygen reduction reaction, polarisation losses at the anode side are comparatively small and therefore often neglected, [3].

The resulting heat flux caused by overpotentials from activation of reactions is given by

$$\tilde{q}^{j}_{\mathrm{act}} = \tilde{\eta}^{j}\,\tilde{i} \tag{1.15}$$

for each of the corresponding half-cells j.

Joule effect

Proton conductivity $\tilde{\sigma}$ in a PEM is finite and in most cases is estimated to depend on temperature and water content λ. Several correlations are summarised in [4]. Humidified membranes show increased conductivity and therefore reduce the voltage drop and energy loss to heat. The corresponding total membrane resistance is calculated by integrating local proton resistance over the membrane height $\tilde{H}_{\mathrm{PEM}}$,

$$\tilde{R}_{\mathrm{PEM}} = \int_0^{\tilde{\mathrm{H}}_{\mathrm{PEM}}} \frac{1}{\tilde{\sigma}(\tilde{T}(\tilde{x}), \lambda(\tilde{x}))} \mathrm{d}\tilde{x}\,, \tag{1.16}$$

whereas the local heat flux is given by

$$\tilde{q}_{\mathrm{Joule}} = \frac{\tilde{i}^2}{\tilde{\sigma}}\,. \tag{1.17}$$

Due to electric resistance, similar heat sources are found in the electrode GDLs and BPs, but can often be neglected as the materials in these domains are good electrical conductors. Finite proton conductivity and the previously mentioned electrochemical activation of reactions have direct impact on the cell potential: The voltage drops due to the membrane resistance $\tilde{R}_{\mathrm{PEM}}$ and the overpotential from equation (1.14) reduce the theoretical cell potential to the the actual cell potential, [3],

$$\tilde{E}_{\mathrm{cell}} = \tilde{E}_{\mathrm{OC}} - \tilde{i}\left(\tilde{\eta}^{\mathrm{C}} + \tilde{R}_{\mathrm{PEM}}\right). \tag{1.18}$$

Membrane sorption and desorption

At the interface between GDL and PEM a further heat source/sink is found due to sorption and desorption of water into and from the membrane, respectively. These processes play an important role in the PEMFC because they determine the hydration and dehydration of the membrane. Their study is still relatively new and many characteristics remain unclear as reported by Jiao and Li [2].

Nonetheless, during these processes heat is released or consumed, depending on the physical conditions present at the GDL-PEM interface. Ramousse et al. [4] state that the sorption of water vapour releases heat, as a mechanism similar to condensation takes place when entering the membrane. This is also reflected in the values for the enthalpy of sorption $\Delta_{\mathrm{sorp}}\tilde{H}$, that are close to the latent heat of water. The sorption of liquid water is isothermal, whereas the desorption of membrane water into the gas phase consumes heat, as an evaporation-like effect takes place.

When the water flux at the GDL-PEM interface is known from a mass transport model, the generated heat flux due to sorption and desorption can be calculated.

Water condensation and evaporation

Water condensation takes place when the partial pressure of water vapour exceeds its saturation pressure $\tilde{p}_{\mathrm{sat}}$, which is a function of temperature. Several equations exist in the literature. The following expression is commonly used in PEMFC modelling and was proposed as a fitting curve by Springer et al. [5],

$$\begin{aligned}\tilde{p}_{\mathrm{sat}}(\tilde{T}) &= 101325 \\ &\times 10^{-2.1749+0.02953(\tilde{T}-273.15\,\mathrm{K})-9.1837\times10^{-5}(\tilde{T}-273.15\,\mathrm{K})^2+1.4454\times10^{-7}(\tilde{T}-273.15\,\mathrm{K})^3}\ [\mathrm{Pa}]\,.\end{aligned} \tag{1.19}$$

The heat released during condensation or consumed during evaporation depends on the mass transfer rate $\tilde{\dot{m}}_k$ between the two phases and can be defined as

$$\tilde{Q}_{\text{phase}} = \tilde{\dot{m}}_{\text{l}} \, \Delta_{\text{lv}} \tilde{H} \, . \tag{1.20}$$

Note that $\tilde{\dot{m}}_{\text{l}}$ is the mass transfer rate into the liquid phase, which is calculated from coupled mass transport equations. Positive $\tilde{\dot{m}}_{\text{l}}$ corresponds to condensation, meaning that heat is released and therefore $\tilde{Q}_{\text{phase}}$ must yield a positive value. Therefore, the latent heat of evaporation $\Delta_{\text{lv}} \tilde{H}$ is used in this definition. Its changes due to fluctuations in the PEMFC temperature field are small and thus can be neglected, [6].

2

Multiphase flow approach

In a PEMFC, water is present in different physical states and undergoes different phase change processes due to the varying operating conditions and material characteristics of its domains. For typical operating conditions, where cell temperature ranges from 60 to 80 °C, water in the GCs, GDLs and CLs exists in vapour and liquid form. Water vapour itself is part of a multicomponent gas mixture as described previously. The ionomer in the CL and PEM absorbs water in liquid state or bound to H^+ (e.g. H_3O^+), [2].

The following section covers a very general derivation of the basic equations used to describe multiphase and multicomponent momentum, heat and mass transport. The model equations for the gas channels and gas diffusion layers of a PEMFC, describing a three-component gas mixture and two-phase system, are then deduced from the corresponding 3D integral conservation laws. Dissolved water transport in the PEM is discussed in section 3.4.

2.1 Multiphase flows

Many different types of multiphase flows occur in nature and industrial processes. Two general topologies of multiphase flows can be identified at the outset, namely separated flows and disperse flows. The latter consist of finite particles, drops or bubbles (the disperse phase) distributed in a connected volume of the continuous phase. Separated flows, on the other hand, consist of continuous streams of different fluids separated by interfaces, [7].

Depending on the present conditions, variable approaches are necessary to describe multiphase flow phenomena. Traditionally, problems of multiphase flow are modelled by a multiphase approach, in which various phases are regarded as distinct fluids with individual thermo-physical properties and thus different phase velocities. The transport phenomena are then described by the basic conservation laws for each individual phase and appropriate interfacial conditions between the adjacent phases.

2.1.1 Mass balance of individual phases

The continuity equation for an individual phase k is given by

$$\frac{\partial(\tilde{\rho}_k \chi_k)}{\partial \tilde{t}} + \tilde{\nabla} \cdot (\tilde{\rho}_k \chi_k \tilde{\boldsymbol{u}}_k) = \tilde{\dot{m}}_k \,, \tag{2.1}$$

[7, 8]. Here, $\tilde{\rho}_k$, $\tilde{\boldsymbol{u}}_k$ and χ_k denote density, velocity and the volume fraction occupied by the individual phase k, respectively. The term $\tilde{\dot{m}}_k$ is called mass interaction term and describes the transfer rate of mass from all other phases to phase k, e.g. due to a phase change or chemical reaction. Since mass as a whole must be conserved, and creation of mass in one phase results in destruction of mass in the other phases, it follows that

$$\sum_k \tilde{\dot{m}}_k = 0. \tag{2.2}$$

2.1.2 Conservation of species within an individual phase

In general, an individual phase k consists of multiple components α, e.g. the gaseous phase is composed of multiple different gases. For each component or species α within phase k the continuity equation must apply as well, which can be written as

$$\frac{\partial(\tilde{\rho}_k \chi_k \xi_k^\alpha)}{\partial \tilde{t}} + \tilde{\nabla} \cdot (\tilde{\rho}_k \chi_k \xi_k^\alpha \tilde{\boldsymbol{u}}_k) = -\tilde{\nabla} \cdot \tilde{\boldsymbol{j}}_k^\alpha + \tilde{J}_k^\alpha \,, \tag{2.3}$$

[8]. Here ξ_k^α denotes the mass fraction of species α in phase k for which the closure condition

$$\sum_\alpha \xi_k^\alpha = 1 \tag{2.4}$$

holds. In the first term on the RHS, $\tilde{j}_k^\alpha$, represents a diffusive flux within the individual phase k due to molecular diffusion and/or hydrodynamic dispersion. It is usually expressed by Fick's law

$$\tilde{\boldsymbol{j}}_k^\alpha = -\tilde{\rho}_k \chi_k \tilde{\mathcal{D}}_k^\alpha \, \tilde{\nabla} \xi_k^\alpha \,, \tag{2.5}$$

where $\tilde{\mathcal{D}}_k^\alpha$ represents the diffusion coefficient of species α within phase k. The last term on the RHS, $\tilde{J}_k^\alpha$, denotes the interphase species transfer rate caused by phase change and/or chemical reactions. With a similar argument to equation (2.2) follows that

$$\sum_k \tilde{J}_k^\alpha = 0 \,. \tag{2.6}$$

Summation over all species α must result in the mass balance of the individual phase k (2.1). Hence,

$$\sum_\alpha \tilde{J}_k^\alpha = \tilde{\dot{m}}_k \,, \qquad \sum_\alpha \tilde{\boldsymbol{j}}_k^\alpha = 0 \,. \tag{2.7}$$

2.1.3 Equation of motion of individual phases

In general, the equation of motion for an individual phase k neglecting gravitational and external forces reads

$$\frac{\partial(\tilde{\rho}_k \chi_k \boldsymbol{u}_k)}{\partial \tilde{t}} + \tilde{\nabla} \cdot (\tilde{\rho}_k \chi_k \tilde{\boldsymbol{u}}_k \otimes \tilde{\boldsymbol{u}}_k) = \tilde{\boldsymbol{f}}_k + \tilde{\nabla} \cdot \tilde{\boldsymbol{\sigma}}_k \,, \tag{2.8}$$

[7]. Here, $\tilde{\boldsymbol{f}}_k$ denotes the force interaction term, which includes all volumetric forces imposed on phase k by other phases. As in the case of mass interaction $\tilde{\dot{m}}$, it follows that

$$\sum_k \tilde{\boldsymbol{f}}_k = 0 \,. \tag{2.9}$$

The last term on the RHS describes the contribution from surface forces on the fluid where $\tilde{\boldsymbol{\sigma}}$ denotes the stress tensor. The stress tensor itself can be decomposed into a pressure $\tilde{p}$ and deviatoric stress $\tilde{\boldsymbol{\sigma}}'$

$$\tilde{\boldsymbol{\sigma}} = -\tilde{p}\, \mathbb{1} + \tilde{\boldsymbol{\sigma}}' \,. \tag{2.10}$$

The actual equation of motion will differ for each multiphase transport problem, depending on the type of multiphase flow, physical properties of the fluid and emerging flow regimes or topologies, e.g. the additional pressure drop in a porous medium has to accounted for by an appropriate source term.

2.1.4 Energy balance of individual phases

As described by the equation for conservation of species within an individual phase, eq. (2.3), mass is transported by both, convection and diffusion. However, diffusing molecules in multicomponent mixtures not only carry along their mass but also energy, and thus changes in composition are accompanied by changes of the multicomponent mixture enthalpy $\tilde{h}_k$,

$$\tilde{h}_k = \sum_\alpha \xi_k^\alpha \tilde{h}_k^\alpha \,. \tag{2.11}$$

To account for the diffusion of enthalpy, the energy balance, e.g. as presented in [7], is extended to yield

$$\frac{\partial(\tilde{\rho}_k \chi_k \tilde{h}_k)}{\partial \tilde{t}} + \tilde{\nabla} \cdot \left(\tilde{\rho}_k \chi_k \tilde{h}_k \tilde{\boldsymbol{u}}_k\right) = -\tilde{\nabla} \cdot \left(\sum_\alpha \tilde{\boldsymbol{j}}_k^\alpha \tilde{h}_k^\alpha\right) + \tilde{\mathcal{L}}_k + \tilde{\mathcal{Q}}_k + \tilde{\mathcal{E}}_k \,, \tag{2.12}$$

where the first RHS term represents the enthalpy fluxes due to concentration gradients within the individual phase, [9]. $\tilde{\mathcal{L}}_k$ and $\tilde{\mathcal{Q}}_k$ denote the mechanical and heat power fed to phase k, respectively. The latter usually consists of a term that describes heat fluxes $\tilde{\boldsymbol{q}}$, e.g. arising from thermal conduction, and volumetric heat sources/sinks $\tilde{Q}_{\text{source}}$, e.g. from the latent heat of phase change or Joule heating,

$$\tilde{\mathcal{Q}}_k = -\tilde{\nabla} \cdot \tilde{\boldsymbol{q}}_k + \tilde{Q}_{\text{source},k} \,. \tag{2.13}$$

As for the mass interaction term in eq. (2.2), for the phase energy interaction term $\tilde{\mathcal{E}}_k$ the closure

$$\sum_k \tilde{\mathcal{E}}_k = 0. \tag{2.14}$$

must apply. Kinetic energy, dissipation, pressure and gravitational effects are neglected in the energy balance above.

2.2 Multiphase mixtures

The modelling of multiphase flows presents major challenges, since the mathematical description of phase interactions is very complex and large computational resources are required to compute the (coupled) governing equations of each individual phase. A more economic approach is to consider the multiple phases as constituents of a multiphase mixture. Such a model only consists of conservation equations for the multiphase mixture itself and is derived from a classical multiphase flow formulation. While certain effects regarding phase interactions can not be represented in a multiphase mixture model, the number of model equations is reduced, allowing an efficient alternative for theoretical analysis and numerical simulation, [7, 8, 10].

The definition of mixture properties is based on averaging physical quantities using phase saturations s_k that represent the volume fraction in the multiphase mixture of each individual phase k, e.g. the mixture density $\tilde{\rho}$ is defined as

$$\tilde{\rho} = \sum_k \tilde{\rho}_k s_k \,. \tag{2.15}$$

Other important mixture quantities are the mixture enthalphy $\tilde{h}$ and the mass fraction of species α ξ^α in the mixture. They are defined as

$$\tilde{\rho}\tilde{h} = \sum_k \tilde{\rho}_k s_k \tilde{h}_k \,, \tag{2.16}$$

$$\tilde{\rho}\xi^{\alpha} = \sum_{k} \tilde{\rho}_k s_k \xi_k^{\alpha} \,. \tag{2.17}$$

The velocities $\boldsymbol{u}_k$ and $\boldsymbol{u}_j$ of the respective phases k and j are different in general due to varying fluid properties. Hence, the corresponding relative velocity is calculated from

$$\tilde{\boldsymbol{u}}_k - \tilde{\boldsymbol{u}}_j = \tilde{\boldsymbol{u}}_{kj} \,, \tag{2.18}$$

whereas the drift velocity $\tilde{\boldsymbol{w}}_k$ of phase k is defined as the velocity of that phase in a frame of reference moving at the velocity of the mixture and thus is given by

$$\tilde{\boldsymbol{w}}_k = \tilde{\boldsymbol{u}}_k - \sum_{j} s_j \tilde{\boldsymbol{u}}_j, \qquad \sum_{k} \tilde{\boldsymbol{w}}_k = 0 \,. \tag{2.19}$$

2.3 Homogeneous flow model (HFM)

However, it is also possible that different phases are sufficiently well mixed and therefore the dispersed phase particle size is also small enough so as to eliminate any significant relative motion. Many bubbly or mist flows come close to this limit and can therefore, to a first approximation, be treated as homogeneous and thus $\tilde{\boldsymbol{u}}_k = \tilde{\boldsymbol{u}}$, [7].

This approximation is further used to describe the multiphase flow in the PEMFC GC. No other materials than the fluid itself appear in the channel, i.e. $\chi_k = s_k$. Consequently,

$$\sum_{k} s_k = 1 \,. \tag{2.20}$$

2.3.1 Total mass balance

From the continuity equation of an individual phase k, equation (2.1), the total mass balance is derived by summation over all phases k and using the identity of the mixture density (2.15). Hence, the mixture continuity equation reads

$$\frac{\partial \tilde{\rho}}{\partial \tilde{t}} + \tilde{\nabla} \cdot (\tilde{\rho}\tilde{\boldsymbol{u}}) = 0 \,. \tag{2.21}$$

2.3.2 Total species balance

For homogeneous flow conditions one finds

$$\frac{\partial (\tilde{\rho}\xi^{\alpha})}{\partial \tilde{t}} + \tilde{\nabla} \cdot (\tilde{\rho}\xi^{\alpha}\tilde{\boldsymbol{u}}) = - \tilde{\nabla} \cdot \left(\sum_{k} \tilde{\boldsymbol{j}}_k^{\alpha} \right) \tag{2.22}$$

by summation of the conservation of species equations, eq. (2.3), over all phases k and considering the definition of the multiphase mixture mass fractions, eq. (2.17). Further summation over all species α results in the total mass balance.

2.3.3 Equation of motion

For dispersed multiphase flow, the equation of motion for each phase k reads

$$\frac{\partial(\tilde{\rho}_k s_k \boldsymbol{u}_k)}{\partial \tilde{t}} + \tilde{\nabla} \cdot (\tilde{\rho}_k s_k \tilde{\boldsymbol{u}}_k \otimes \tilde{\boldsymbol{u}}_k) = \tilde{\boldsymbol{f}}_k - \delta_k \left\{ \tilde{\nabla} \tilde{p} - \tilde{\nabla} \cdot \tilde{\boldsymbol{\sigma}}' \right\}, \tag{2.23}$$

[7]. Here, the last term on the RHS represents the surface forces due to the divergence of the stress tensor $\tilde{\boldsymbol{\sigma}}$, which is further decomposed with the identity (2.10). Surface forces only effect the continuous phase ($\tilde{p} = \tilde{p}_\mathrm{C}$) and therefore

$$\delta_k = \begin{cases} 1, & \text{continuous phase,} \\ 0, & \text{dispersed phase.} \end{cases} \tag{2.24}$$

Summation of all individual phase equations finally yields the equation of motion for homogeneous flow when no external forces are applied to the fluid,

$$\frac{\partial(\tilde{\rho}\boldsymbol{u})}{\partial \tilde{t}} + \tilde{\nabla} \cdot (\tilde{\rho} \tilde{\boldsymbol{u}} \otimes \tilde{\boldsymbol{u}}) = -\tilde{\nabla} \tilde{p}_\mathrm{C} - \tilde{\nabla} \cdot \tilde{\boldsymbol{\sigma}}'_\mathrm{C} \,. \tag{2.25}$$

2.3.4 Total energy balance

The total energy balance is found by summation of all individual phase energy balances, eq. (2.12). If no external mechanical power is applied to the system, the total energy balance yields

$$\frac{\partial(\tilde{\rho}\tilde{h})}{\partial \tilde{t}} + \tilde{\nabla} \cdot \left(\tilde{\rho} \tilde{h} \tilde{\boldsymbol{u}} \right) = -\tilde{\nabla} \cdot \tilde{\boldsymbol{q}} - \tilde{\nabla} \cdot \left(\sum_k \sum_\alpha \tilde{\boldsymbol{j}}_k^\alpha \tilde{h}_k^\alpha \right) + \tilde{Q}_\mathrm{source} \,. \tag{2.26}$$

Here, $\tilde{\boldsymbol{q}}$ denotes the total heat flux and $\tilde{Q}_\mathrm{source}$ is the total volumetric heat source of all phases, see section 1.3. The second RHS term represents the previously discussed transport of enthalpy in the multiphase mixture due to diffusing multicomponent mixtures.

2.4 Multiphase mixture model in capillary porous media (MMM)

Within the porous GDL, the assumption of homogeneous flow cannot be maintained as capillary effects result in relative motions between the liquid and gaseous phase. To model the multiphase flow within the GDL domain, the multiphase mixture model (MMM) for multicomponent transport in capillary porous media, proposed by Wang and Cheng [8, 10], is adopted. The derivation of the MMM model equations is summarised in the following.

The porosity ε of a porous medium is defined as the ratio of void space volume to total volume

$$\varepsilon = \frac{\tilde{V}_0}{\tilde{V}} \,. \tag{2.27}$$

The total space occupied by phase k within a porous medium then is $\chi_k = \varepsilon s_k$. In the following ε is assumed to be constant everywhere in the porous medium. As for the homogeneous flow model

$$\sum_k s_k = 1 \tag{2.28}$$

must apply. Mixture quantities like density, enthalpy or mass fraction of species α are defined identically to the HFM. Additionally, a mass averaged mixture velocity is introduced as

$$\tilde{\rho}\tilde{\boldsymbol{u}} = \sum_k \tilde{\rho}_k s_k \tilde{\boldsymbol{u}}_k \,. \tag{2.29}$$

In the MMM the mixture kinematic viscosity $\tilde{\nu}$ is defined as

$$\tilde{\nu} = \left(\sum_k \frac{\kappa_{\mathrm{r}_k}}{\tilde{\nu}_k} \right)^{-1} , \tag{2.30}$$

where $\kappa_{\mathrm{r_k}}$ denotes the relative permeability of phase k, solely a function of phase saturation s_k, which accounts for the limited pore space available due to the presence of other phases. Together with the mixture kinematic viscosity $\tilde{\nu}$ and the individual phase kinematic viscosity $\tilde{\nu}_k$ the relative mobility of each phase ζ_k within the multiphase mixture is given by

$$\zeta_k = \frac{\kappa_{\mathrm{r}_k}}{\tilde{\nu}_k}\tilde{\nu} \,, \qquad \sum_k \zeta_k = 1 \,. \tag{2.31}$$

2.4.1 Equation of motion

The equation of motion in the MMM is derived from Darcy's law. Starting from the individual phase momentum balance

$$\tilde{\rho}_k s_k \tilde{\boldsymbol{u}}_k = -\frac{1}{\varepsilon}\frac{\tilde{\kappa}\,\kappa_{\mathrm{r}_k}}{\tilde{\nu}_k}\tilde{\nabla}\tilde{p}_k = -\frac{1}{\varepsilon}\frac{\tilde{\kappa}}{\tilde{\nu}}\zeta_k\tilde{\nabla}\tilde{p}_k \,, \tag{2.32}$$

where $\tilde{\kappa}$ is the total permeability of the porous medium, the mixture equation of motion is found by summation over all phases k and by applying the definitions for the relative mobility (2.31) and mixture velocity (2.29). When gravitational effects are neglected, it yields

$$\tilde{\rho}\tilde{\boldsymbol{u}} = -\frac{1}{\varepsilon}\frac{\tilde{\kappa}}{\tilde{\nu}}\tilde{\nabla}\tilde{p} \,. \tag{2.33}$$

The mixture pressure is defined such that the following differential equation holds

$$\tilde{\nabla}\tilde{p} = \sum_j \zeta_j \tilde{\nabla}\tilde{p}_j = \tilde{\nabla}\tilde{p}_k + \sum_j \zeta_j \tilde{\nabla}\tilde{p}_{\mathrm{c}jk} \,. \tag{2.34}$$

Here, $\tilde{p}_{\mathrm{c}jk} = \tilde{p}_k - \tilde{p}_j$ is the capillary pressure which represents the difference between the pressures of two adjacent phases k and j. It depends on pore geometry, physical properties of the fluid, e.g. surface tension $\tilde{\varsigma}_{jk} = \tilde{\varsigma}_{jk}(\xi^\alpha, \tilde{T})$, and phase saturations. Hence, the gradient of the capillary pressure can be expressed as

$$\tilde{\nabla}\tilde{p}_{\mathrm{c}jk} = \sum_i \frac{\partial \tilde{p}_{\mathrm{c}jk}}{\partial s_i}\tilde{\nabla}s_i + \frac{\partial \tilde{p}_{\mathrm{c}jk}}{\partial \tilde{\varsigma}_{jk}}\left[\sum_\alpha \frac{\partial \tilde{\varsigma}_{jk}}{\partial \xi^\alpha}\tilde{\nabla}\xi^\alpha + \frac{\partial \tilde{\varsigma}_{jk}}{\partial \tilde{T}}\tilde{\nabla}\tilde{T}\right]. \tag{2.35}$$

Substituting eq. (2.35) into (2.34) then yields

$$\tilde{\nabla}\tilde{p} = \tilde{\nabla}\tilde{p}_k + \sum_i \tilde{\mathrm{Ca}}_{ik}\tilde{\nabla}s_i + \sum_\alpha \tilde{\mathrm{Cs}}_{\alpha k}\tilde{\nabla}\xi^\alpha + \tilde{\mathrm{Ct}}_k\tilde{\nabla}\tilde{T} \,, \tag{2.36}$$

where $\tilde{\mathrm{Ca}}_{ik}$, $\tilde{\mathrm{Cs}}_{\alpha k}$ and $\tilde{\mathrm{Ct}}_k$ are called the capillary, solutal-capillary and thermo-capillary factors, respectively. They are given by

$$\tilde{\mathrm{Ca}}_{ik} = \sum_j \zeta_j \frac{\partial \tilde{p}_{cjk}}{\partial s_i}\,, \tag{2.37}$$

$$\tilde{\mathrm{Cs}}_{\alpha k} = \sum_j \zeta_j \frac{\partial \tilde{p}_{cjk}}{\partial \tilde{\zeta}_{jk}} \frac{\partial \tilde{\zeta}_{jk}}{\partial \xi^\alpha}\,, \tag{2.38}$$

$$\tilde{\mathrm{Ct}}_k = \sum_j \zeta_j \frac{\partial \tilde{p}_{cjk}}{\partial \tilde{\zeta}_{jk}} \frac{\partial \tilde{\zeta}_{jk}}{\partial \tilde{T}}\,. \tag{2.39}$$

Integration of eq. (2.36) results in the following explicit definition of the mixture pressure

$$\tilde{p} = \tilde{p}_k + \sum_i \int_0^{s_i} \tilde{\mathrm{Ca}}_{ik}\,\mathrm{d}s_i + \sum_\alpha \int_0^{\xi^\alpha} \tilde{\mathrm{Cs}}_{\alpha k}\,\mathrm{d}\xi^\alpha + \int_0^{\tilde{T}} \tilde{\mathrm{Ct}}_k\,\mathrm{d}\tilde{T}\,. \tag{2.40}$$

The difference in the gradients of the mixture pressure p and phase pressure p_k gives rise to the capillary diffusion flux $\tilde{\boldsymbol{\psi}}_k$,

$$\tilde{\boldsymbol{\psi}}_k = \frac{\tilde{\kappa}}{\tilde{\nu}} \zeta_k \left(\tilde{\nabla}\tilde{p} - \tilde{\nabla}\tilde{p}_k \right). \tag{2.41}$$

With the definitions of the equations of motions in eq. (2.32) and (2.33) one finds

$$\tilde{\rho}_k s_k \tilde{\boldsymbol{u}}_k = \frac{1}{\varepsilon}\tilde{\boldsymbol{\psi}}_k + \zeta_k \tilde{\rho}\tilde{\boldsymbol{u}}\,, \qquad \sum_k \tilde{\boldsymbol{\psi}}_k = 0\,. \tag{2.42}$$

Substituting the pressure gradients from eq(2.36) into (2.41) finally yields

$$\tilde{\boldsymbol{\psi}}_k = -\sum_i \left(\tilde{\rho}_k \tilde{\mathcal{D}}_{cik} \tilde{\nabla} s_i \right) - \sum_\alpha \left(\tilde{\rho}_k \tilde{\mathcal{D}}_{s\alpha k} \tilde{\nabla} \xi^\alpha \right) - \tilde{\rho}_k \tilde{\mathcal{D}}_{tk} \tilde{\nabla} \tilde{T}\,. \tag{2.43}$$

Here, $\tilde{\mathcal{D}}_{cik}$, $\tilde{\mathcal{D}}_{s\alpha k}$ and $\tilde{\mathcal{D}}_{tk}$ denote the capillary, solutal-capillary and thermo-capillary diffusion coefficients, respectively, which are given by

$$\tilde{\mathcal{D}}_{cik} = \frac{\tilde{\kappa}}{\tilde{\rho}_k \tilde{\nu}} \tilde{\zeta}_k \sum_j \zeta_j \left(-\frac{\partial \tilde{p}_{cjk}}{\partial s_i} \right), \tag{2.44}$$

$$\tilde{\mathcal{D}}_{s\alpha k} = \frac{\tilde{\kappa}}{\tilde{\rho}_k \tilde{\nu}} \tilde{\zeta}_k \sum_j \zeta_j \left(-\frac{\partial \tilde{p}_{cjk}}{\partial \tilde{\zeta}_{jk}} \frac{\partial \tilde{\zeta}_{jk}}{\partial \xi^\alpha} \right), \tag{2.45}$$

$$\tilde{\mathcal{D}}_{tk} = \frac{\tilde{\kappa}}{\tilde{\rho}_k \tilde{\nu}} \tilde{\zeta}_k \sum_j \zeta_j \left(-\frac{\partial \tilde{p}_{cjk}}{\partial \tilde{\zeta}_{jk}} \frac{\partial \tilde{\zeta}_{jk}}{\partial \tilde{T}} \right). \tag{2.46}$$

2.4.2 Total mass balance

To obtain the total mass balance of the multiphase mixture, again individual phase continuity equations are summed over each phase k similar to the HFM. The total mass balance is identical to the HFM formulation in equation (2.21) and reads

$$\frac{\partial \tilde{\rho}}{\partial \tilde{t}} + \tilde{\nabla} \cdot (\tilde{\rho}\tilde{\boldsymbol{u}}) = 0\,. \tag{2.47}$$

2.4.3 Total species balance

The total, multiphase equation for the conservation of species is obtained by summation of the individual phase equations (2.3) over all phases k,

$$\varepsilon \frac{\partial(\tilde{\rho}\xi^{\alpha})}{\partial \tilde{t}} + \varepsilon \, \tilde{\nabla} \cdot \left(\sum_k \tilde{\rho}_k s_k \xi_k^{\alpha} \tilde{\boldsymbol{u}}_k \right) = - \tilde{\nabla} \cdot \left(\sum_k \tilde{\boldsymbol{j}}_k^{\alpha} \right). \tag{2.48}$$

With the definition for the MMM phase velocity from (2.42) follows

$$\varepsilon \frac{\partial(\tilde{\rho}\xi^{\alpha})}{\partial \tilde{t}} + \varepsilon \, \tilde{\nabla} \cdot \left(\sum_k (\zeta_k \xi_k^{\alpha}) \tilde{\rho} \tilde{\boldsymbol{u}} \right) = - \tilde{\nabla} \cdot \left(\sum_k \tilde{\boldsymbol{j}}_k^{\alpha} \right) - \tilde{\nabla} \cdot \left(\sum_k \xi_k^{\alpha} \tilde{\boldsymbol{\psi}}_k \right). \tag{2.49}$$

By introducing a correction factor γ_{α} for species transport

$$\gamma_{\alpha} = \frac{\tilde{\rho} \sum_k \zeta_k \xi_k^{\alpha}}{\sum_k \tilde{\rho}_k s_k \xi_k^{\alpha}}, \tag{2.50}$$

the continuity equation for species α finally yields

$$\varepsilon \frac{\partial(\tilde{\rho}\xi^{\alpha})}{\partial \tilde{t}} + \varepsilon \, \tilde{\nabla} \cdot (\gamma_{\alpha} \tilde{\rho} \xi^{\alpha} \tilde{\boldsymbol{u}}) = - \tilde{\nabla} \cdot \left(\sum_k \tilde{\boldsymbol{j}}_k^{\alpha} \right) - \tilde{\nabla} \cdot \left(\sum_k \xi_k^{\alpha} \tilde{\boldsymbol{\psi}}_k \right). \tag{2.51}$$

2.4.4 Total energy balance

Similar to the HFM, the energy balance in the MMM is derived from the individual phase equation (2.12). Additionally, the solid matrix of the porous medium (fixed in space) has to be accounted for in terms of enthalpy $\tilde{h}_{\mathrm{s}}$ and thermal conduction due to its thermal conductivity $\tilde{k}_{\mathrm{s}}$. The total energy balance reads

$$\begin{aligned}(1-\varepsilon) \frac{\partial(\tilde{\rho}_{\mathrm{s}} \tilde{h}_{\mathrm{s}})}{\partial t} + \varepsilon \sum_k \frac{\partial(\tilde{\rho}_k s_k \tilde{h}_k)}{\partial \tilde{t}} + \varepsilon \, \tilde{\nabla} \cdot \left(\sum_k \tilde{\rho}_k s_k \tilde{h}_k \tilde{\boldsymbol{u}}_k \right) &= \tilde{\nabla} \cdot \left(\tilde{k}_{\mathrm{eff}} \tilde{\nabla} \tilde{T} \right) \\ &\quad - \tilde{\nabla} \cdot \left(\sum_k \sum_{\alpha} \tilde{\boldsymbol{j}}_k^{\alpha} \tilde{h}_k^{\alpha} \right) + \tilde{Q}_{\mathrm{source}}, \end{aligned} \tag{2.52}$$

where the solid matrix and all fluid phases are assumed to be in thermal equilibrium. Furthermore, $\tilde{k}_{\mathrm{eff}}$ denotes the effective thermal conductivity of the solid and fluid which is calculated with

$$\tilde{k}_{\mathrm{eff}} = \varepsilon \sum_k s_k \tilde{k}_k + (1-\varepsilon) \tilde{k}_{\mathrm{s}}. \tag{2.53}$$

Comparable with the species transport equation, eq. (2.50), a correction factor γ_{h} for enthalpy convective fluxes

$$\gamma_{\mathrm{h}} = \frac{\tilde{\rho} \sum_k \zeta_k \tilde{h}_k}{\sum_k \tilde{\rho}_k s_k \tilde{h}_k} \tag{2.54}$$

is introduced. By substituting the MMM phase velocity, eq. (2.42), the energy balance then can be rewritten to finally yield

$$(1-\varepsilon)\,\frac{\partial(\tilde{\rho}_{\mathrm{s}}h_{\mathrm{s}})}{\partial t}+\varepsilon\,\frac{\partial(\tilde{\rho}\tilde{h})}{\partial t}+\varepsilon\,\tilde{\nabla}\cdot\left(\gamma_{\mathrm{h}}\tilde{\rho}\tilde{h}\tilde{\boldsymbol{u}}\right)=\tilde{\nabla}\cdot\left(\tilde{k}_{\mathrm{eff}}\tilde{\nabla}\tilde{T}\right)$$
$$-\,\tilde{\nabla}\cdot\left(\sum_{k}\sum_{\alpha}\tilde{\boldsymbol{j}}_{k}^{\alpha}\tilde{h}_{k}^{\alpha}\right)-\tilde{\nabla}\cdot\left(\sum_{k}\tilde{h}_{k}\tilde{\boldsymbol{\psi}}_{k}\right)+\tilde{Q}_{\mathrm{source}}\,. \quad (2.55)$$

3
Physical-mathematical model

The multiphase flow equations presented in section 2 are further used to extend the isothermal singlephase model from Murschenhofer et al. [1]. Following their quasi-2D approach, the novel governing equations are presented in the following.

The modelled PEMFC single cell domain, which is bounded by the BPs, is depicted in figure 2. For the boundary planes perpendicular to the x_3-direction periodic boundary conditions are applied. Furthermore, mass exchange in x_1-direction only takes place via the GC in- and outlets. The governing equations are formulated individually for the GCs, GDLs and the PEM. The CLs are assumed to be infinitely thin and are used for the coupling of the GDL and PEM domains. Thus, the source terms that account for the electrochemical half-cell reactions appear as boundary/coupling conditions at the GDL-PEM interfaces.

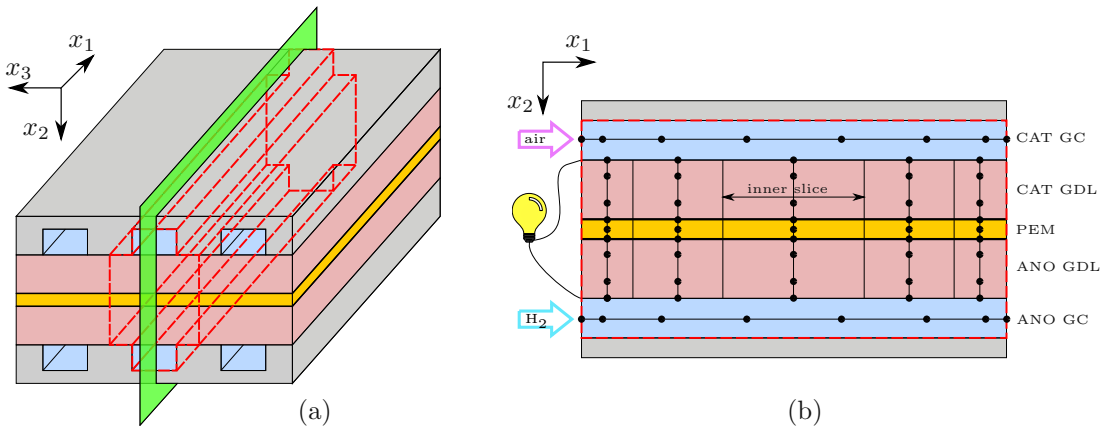

Figure 2: (a) 3D PEMFC geometry with the modelled (single cell) domain, bounded by dashed red lines and the considered 2D plane in green. (b) Discretised quasi-2D model domain with $N_{\mathrm{GC}}^{\mathrm{C,A}} = 8$, $N_{\mathrm{GDL}}^{\mathrm{C,A}} = 4$ and $N_{\mathrm{PEM}} = 3$ computation nodes for the gas channels, the GDLs and membrane, respectively, and the number of so-called 'inner slices' $N_{\mathrm{SL}} = 5$.

In the following, the multiphase mixture quantities are denoted without subscript, while (g) denotes the gas phase, (l) the liquid phase and (s) the solid GDL material. The phase saturation s, relative mobility ζ and mass transfer rate m are assigned to the liquid phase only and the subscript (l) is omitted. Consequently, gas phase saturation, gas phase relative mobility and gas phase mass transfer rate in the two-phase system are given by $1 - s$, $1 - \zeta$ and $1 - m$, respectively. Index β is used to indicate the reactant gas of the cathode side ($= \mathrm{O_2}$) and anode side ($= \mathrm{H_2}$), whereas $\alpha = \mathrm{O_2}, \mathrm{N_2}, \mathrm{H_2O}$ and $\alpha = \mathrm{H_2}, \mathrm{N_2}, \mathrm{H_2O}$, respectively.

The gas mixture is assumed to be composed of ideal gases and its properties such as viscosity, diffusion coefficients, specific heat capacities, etc. depend on the species distribution. All material properties are approximated to be constant within the expected operating temperature and

pressure range of the PEMFC, [6]. As the temperature changes and convective velocities in the gas channels are relatively low, the flow is treated as laminar, (hydrodynamically and thermally) locally fully developed and thus goverened by a paraboloid like velocity and temperature profile [11, 12]. Furthermore, for low velocities and small temperature changes, the flow can be assumed as incompressible and the gas density $\tilde{\rho}_\mathrm{g}$ depends on the species and temperature distribution only. Thus, as liquid water is also incompressible, the same follows for the multiphase mixture density $\tilde{\rho}$. Consequently, $\tilde{\rho}$ is a function of gas phase species distribution and liquid phase saturation s.

Diffusion coefficients of gases in liquids are only of a factor of 10^{-4} to those in gases [13]. Fickian diffusion fluxes within the liquid phase are therefore neglected. Besides, O_2, H_2 and N_2 are assumed to be unsoluble in the liquid phase, with the consequence that $\xi_\mathrm{l}^{\mathrm{H_2O}} = 1$. From the definition of multiphase mixture mass fractions (2.17) follows

$$\xi^\beta = \tilde{\rho}_\mathrm{g}(1-s)\xi_\mathrm{g}^\beta\,, \qquad \xi^{\mathrm{H_2O}} = \tilde{\rho}_\mathrm{l} s + \tilde{\rho}_\mathrm{g}(1-s)\xi_\mathrm{g}^{\mathrm{H_2O}}\,. \tag{3.1}$$

The third gas phase mass fraction $\xi_\mathrm{g}^{\mathrm{N_2}}$ is found from the closure condition

$$\xi_\mathrm{g}^\beta + \xi_\mathrm{g}^{\mathrm{N_2}} + \xi_\mathrm{g}^{\mathrm{H_2O}} = 1\,. \tag{3.2}$$

The species diffusion model from [1] is revised to account for the just mentioned restraint for diffusive fluxes due to the presence of liquid water, [14]. Hence, the multicomponent diffusion fluxes are expressed as

$$\tilde{\boldsymbol{j}}^\beta = -\tilde{\rho}_\mathrm{g}\left[(1-s)\varepsilon\right]^q \left(\tilde{\mathcal{D}}_{\beta,\beta}\,\tilde{\nabla}\xi_\mathrm{g}^\beta + \tilde{\mathcal{D}}_{\beta,\mathrm{H_2O}}\,\tilde{\nabla}\xi_\mathrm{g}^{\mathrm{H_2O}}\right), \tag{3.3}$$

$$\tilde{\boldsymbol{j}}^{\mathrm{H_2O}} = -\tilde{\rho}_\mathrm{g}\left[(1-s)\varepsilon\right]^q \left(\tilde{\mathcal{D}}_{\mathrm{H_2O},\beta}\,\tilde{\nabla}\xi_\mathrm{g}^\beta + \tilde{\mathcal{D}}_{\mathrm{H_2O},\mathrm{H_2O}}\,\tilde{\nabla}\xi_\mathrm{g}^{\mathrm{H_2O}}\right), \tag{3.4}$$

whereas the third flux is used to close the system,

$$\tilde{\boldsymbol{j}}^\beta + \tilde{\boldsymbol{j}}^{\mathrm{H_2O}} + \tilde{\boldsymbol{j}}^{\mathrm{N_2}} = \boldsymbol{0}\,. \tag{3.5}$$

Here, $q = 1.5$ is the Bruggeman exponent to account for the tortuosity of the porous GDL, [2]. In this context it is important to mention that the effect of Fickian gas phase diffusion is underestimated in the dimensionless groups of the multiphase model given in appendix C and [1]. Computed values for the binary diffusion coefficients $\tilde{\mathcal{D}}_{\beta,\beta}$, $\tilde{\mathcal{D}}_{\beta,\mathrm{H_2O}}$, $\tilde{\mathcal{D}}_{\mathrm{H_2O},\beta}$ and $\tilde{\mathcal{D}}_{\mathrm{H_2O},\mathrm{H_2O}}$ are up to 10^4 times the chosen reference binary diffusion coefficients $\tilde{\mathcal{D}}_r$. Thus, gas diffusion must be accounted for in both the GCs and GDLs. The associated diffusive enthalpy flux for the three component system at hand is given by

$$\tilde{\boldsymbol{r}} = \underbrace{(\tilde{h}_\mathrm{g}^\beta - \tilde{h}_\mathrm{g}^{\mathrm{N_2}})\,\tilde{\boldsymbol{j}}^\beta}_{\tilde{\boldsymbol{r}}^\beta} + \underbrace{(\tilde{h}_\mathrm{g}^{\mathrm{H_2O}} - \tilde{h}_\mathrm{g}^{\mathrm{N_2}})\,\tilde{\boldsymbol{j}}^{\mathrm{H_2O}}}_{\tilde{\boldsymbol{r}}^{\mathrm{H_2O}}}\,. \tag{3.6}$$

Heat fluxes due to thermal conduction are modelled with Fourier's law

$$\tilde{\boldsymbol{q}} = -\tilde{k}\,\tilde{\nabla}\tilde{T}\,, \tag{3.7}$$

where $\tilde{T}$ denotes the absolute temperature and $\tilde{k}$ is the multiphase mixture thermal conductivity, calculated similarly to mixture quantities defined in section 2.2. The gas mixture specific thermal conductivity $\tilde{k}_\mathrm{g}$ and specific heat capacity $\tilde{c}_{\mathrm{p_g}}$ are assumed to depend on species mass fractions only, e.g.

$$\tilde{c}_{\mathrm{p_g}} = \sum_\alpha \xi_\mathrm{g}^\alpha\,\tilde{c}_{\mathrm{p_g}}^\alpha\,. \tag{3.8}$$

As gas phase and liquid phase are in thermal equilibrium, one finds from definition (2.16) the multiphase mixture specific heat capacity $\tilde{c}_\mathrm{p}$

$$\tilde{\rho}\,\tilde{c}_\mathrm{p} = \tilde{\rho}_\mathrm{l}\,s\,\tilde{c}_{\mathrm{p_l}} + \tilde{\rho}_\mathrm{g}\,(1-s)\,\tilde{c}_{\mathrm{p_g}} \tag{3.9}$$

to further calculate the multiphase mixture specific enthalpy

$$\tilde{\rho}\tilde{h} = \tilde{\rho}\tilde{c}_\mathrm{p}\,\tilde{T}\,. \tag{3.10}$$

The liquid saturation s of the multiphase mixture is obtained following Wang et al. [15]: With the temperature dependent function for the saturation pressure $\tilde{p}_\mathrm{sat}$, eq. (1.19), the saturation mass fraction of water in the gas phase $\xi_\mathrm{sat}^{\mathrm{H_2O}}$ is given by the ideal gas law

$$\xi_\mathrm{g,sat}^{\mathrm{H_2O}} = \frac{\tilde{M}^{\mathrm{H_2O}}\,\tilde{p}_\mathrm{sat}(\tilde{T})}{\tilde{\mathcal{R}}\,\tilde{\rho}_\mathrm{g}\,\tilde{T}}\,. \tag{3.11}$$

Liquid saturation s then is calculated from the step function

$$s = \begin{cases} \frac{\tilde{\rho}_\mathrm{g}\left(\xi^{\mathrm{H_2O}} - \xi_\mathrm{g,sat}^{\mathrm{H_2O}}\right)}{\tilde{\rho}_\mathrm{l}\left(1-\xi^{\mathrm{H_2O}}\right) + \tilde{\rho}_\mathrm{g}\left(\xi^{\mathrm{H_2O}} - \xi_\mathrm{g,sat}^{\mathrm{H_2O}}\right)} & \text{if} \quad \xi_\mathrm{g}^{\mathrm{H_2O}} \geq \xi_\mathrm{g,sat}^{\mathrm{H_2O}}\,, \\ 0 & \text{if} \quad \xi_\mathrm{g}^{\mathrm{H_2O}} < \xi_\mathrm{g,sat}^{\mathrm{H_2O}}\,. \end{cases} \tag{3.12}$$

3.1 Quasi-2D approach

Starting from a typical 3D PEMFC (single cell) geometry as depicted e.g. in figure 2, a 2D domain is obtained by cutting through the channel's symmetry plane. Further, a quasi-2D approach, described by Kulikovsky [16], is applied by considering only the principle directions for gradients of the corresponding variables in each domain. These domains are treated quasi-1D with their model equations found from the full 3D conservation laws. The quasi-2D model is then obtained by connecting the two parallel gas channels with an arbitrary number of inner slices, each composed of cathode and anode GDLs, infinitely thin cathode and anode catalyst layers and a PEM in the middle, [1].

To get to the quasi-1D formulation of each domain cross-sectional averaging is applied to the relevant variables, e.g. for the velocity profile in the GC $\tilde{u}_1(\tilde{\boldsymbol{x}}, \tilde{t})$

$$\bar{\tilde{u}}_1(\tilde{x}_1, \tilde{t}) = \frac{1}{\tilde{W}_\mathrm{GC}\tilde{H}_\mathrm{GC}} \int_0^{\tilde{W}_\mathrm{GC}} \int_0^{\tilde{H}_\mathrm{GC}} \tilde{u}_1(\tilde{\boldsymbol{x}}, \tilde{t})\mathrm{d}\tilde{x}_2\mathrm{d}\tilde{x}_3\,. \tag{3.13}$$

Since the GC height $\tilde{H}_\mathrm{GC}$ and width $\tilde{W}_\mathrm{GC}$ are small compared to the GC length, $\tilde{H}_\mathrm{GC} \ll \tilde{L}$ and $\tilde{W}_\mathrm{GC} \ll \tilde{L}$, species variations along x_2 and x_3 are negligibly small compared to variations along x_1. Hence, species mass fractions ξ_g^α in the gas channel are assumed to depend on the main stream direction x_1 only

$$\xi_\mathrm{g}^\alpha = \bar{\xi}_\mathrm{g}^\alpha(\tilde{x}_1, \tilde{t})\,, \tag{3.14}$$

and thus, physical properties of the fluid, e.g. the specific heat capacity $\tilde{c}_\mathrm{p}$, diffusion coefficients $\tilde{\mathcal{D}}$ and dynamic viscosity $\tilde{\mu}$, are also functions of x_1 only. Although GC temperature variations in x_2 direction are typically non negligible due to the cooling heat flux between GDL and BP, spatial resolution of the temperature field in x_2 is avoided for better computational efficiency. Consequently,

the multicomponent gas mixture density is also assumed to depend on the main stream direction x_1 only,

$$\tilde{\rho}_\mathrm{g} = \bar{\tilde{\rho}}_\mathrm{g}(\tilde{x}_1, \tilde{t})\,. \tag{3.15}$$

Two kinds of temperature averages have to be considered, [17]: the cross-sectional averaged temperature $\bar{\tilde{T}}_\mathrm{A}$ and the adiabatic mixture temperature $\bar{\tilde{T}}_\mathrm{F}$. The latter determines the convective heat flux from the gas channels' fluid to the channel walls (the BP)

$$\tilde{q}_\mathrm{BP} = \tilde{\alpha}\,(\bar{\tilde{T}}_\mathrm{F} - \tilde{T}_\mathrm{BP})\,. \tag{3.16}$$

Here, $\tilde{\alpha}$ denotes the convective heat transfer coefficient. For the adiabatic mixture temperature $\tilde{T}_\mathrm{F}$ in the case of $\tilde{\rho} = \bar{\tilde{\rho}}(\tilde{x}_1, \tilde{t})$ and $\tilde{c}_\mathrm{p} = \bar{\tilde{c}}_\mathrm{p}(\tilde{x}_1, \tilde{t})$ follows

$$\bar{\tilde{T}}_\mathrm{F}(\tilde{x}_1, \tilde{t}) = \frac{1}{\tilde{W}_\mathrm{GC}\tilde{H}_\mathrm{GC}} \frac{1}{\bar{\tilde{u}}_1(\tilde{x}_1, \tilde{t})} \int_0^{\tilde{W}_\mathrm{GC}} \int_0^{\tilde{H}_\mathrm{GC}} \tilde{T}(\tilde{\boldsymbol{x}}, \tilde{t})\, \tilde{u}_1(\tilde{\boldsymbol{x}}, \tilde{t})\, \mathrm{d}\tilde{x}_2 \mathrm{d}\tilde{x}_3\,, \tag{3.17}$$

whereas the cross-sectional averaged temperature $\tilde{T}_\mathrm{A}$ is given by

$$\bar{\tilde{T}}_\mathrm{A}(\tilde{x}_1, \tilde{t}) = \frac{1}{\tilde{W}_\mathrm{GC}\tilde{H}_\mathrm{GC}} \int_0^{\tilde{W}_\mathrm{GC}} \int_0^{\tilde{H}_\mathrm{GC}} \tilde{T}(\tilde{\boldsymbol{x}}, \tilde{t})\, \mathrm{d}\tilde{x}_2 \mathrm{d}\tilde{x}_3\,. \tag{3.18}$$

For the scope of this work and pursued accuracy of the model however, differences between $\bar{\tilde{T}}_\mathrm{A}$ and $\bar{\tilde{T}}_\mathrm{F}$ are assumed to be negligible and hence $\bar{\tilde{T}} \equiv \bar{\tilde{T}}_\mathrm{A} = \bar{\tilde{T}}_\mathrm{F}$.

Since the saturation pressure $\tilde{p}_\mathrm{sat}$ is solely a function of $\bar{\tilde{T}}$, the liquid phase saturation s and all liquid and multiphase mixture variables in the GCs are also only functions of x_1. On the other hand, in the GDL and the PEM x_2 is found to be the principal direction for mass and energy transport, [16]. For sufficiently small widths of the inner slices $\tilde{W}_\mathrm{SL}$, the variables in the GDL and PEM depend on x_2 only.

3.2 Gas channel

The gas channel flow turns out to be laminar in general, [16], and is assumed to be locally fully developed,

$$\tilde{\boldsymbol{u}}(\tilde{\boldsymbol{x}}, \tilde{t}) = \tilde{u}_1(\tilde{\boldsymbol{x}}, \tilde{t})\, \boldsymbol{e}_1 \tag{3.19}$$

with the unit vector $\boldsymbol{e}_1 = (1, 0, 0)^T$. Even though mass and energy is exchanged with the GDL, the paraboloid like velocity and temperature profile, as well as the approximated validity of the no-slip condition is assumed to hold throughout, [1]. The situation is depicted schematically in fig. 3a, where an asymmetric temperature distribution is indicated due to $\tilde{T}_\mathrm{BP} \neq \tilde{T}_\mathrm{GDL}$. Homogeneous flow of the liquid water and multicomponent gas mixture is assumed further, $\tilde{u}_{\mathrm{l},1} = \tilde{u}_{\mathrm{g},1} = \tilde{u}_1$, with the liquid water dispersed as mist in the continuous gas phase.

In order to derive the governing equations for the gas channel, the integral formulation of e.g. the conservation of energy

$$\int_{\tilde{CV}} \frac{\partial(\tilde{\rho}\tilde{c}_\mathrm{p}\tilde{T})}{\partial\tilde{t}}\, \mathrm{d}\tilde{V} + \oint_{\partial\tilde{CV}} \tilde{\rho}\tilde{c}_\mathrm{p}\tilde{T}\, \tilde{\boldsymbol{u}} \cdot \boldsymbol{n}\, \mathrm{d}\tilde{S} = -\oint_{\partial\tilde{CV}} (\tilde{\boldsymbol{q}} + \tilde{\boldsymbol{r}}) \cdot \boldsymbol{n}\, \mathrm{d}\tilde{S} + \int_{\tilde{CV}} \tilde{Q}_\mathrm{source}\, \mathrm{d}\tilde{V} \tag{3.20}$$

is evaluated for the control volume $\tilde{CV}$ fixed in space, depicted in fig. 3a (red dashed rectangle), using the assumption that mass fractions, density and material properties only depend on x_1 and

by applying the definitions for the two cross-sectional averages of the temperature, eq. (3.17) and eq. (3.18), indicated in fig. 3b. Taylor series expansion at x_1^* in the limit $\Delta\tilde{x}_1 \to 0$ then yields the differential equation (bars omitted)

$$\frac{\partial(\tilde{\rho}\tilde{c}_\mathrm{p}\tilde{T})}{\partial\tilde{t}} + \frac{\partial(\tilde{\rho}\tilde{c}_\mathrm{p}\tilde{T}\tilde{u}_1)}{\partial\tilde{x}_1} = \frac{\partial}{\partial\tilde{x}_1}\left(\tilde{k}\,\frac{\partial\tilde{T}}{\partial\tilde{x}_1}\right) - \frac{\partial\tilde{r}_1}{\partial\tilde{x}_1} - \frac{\tilde{\alpha}}{\tilde{H}_\mathrm{GC}}\left(\tilde{T}-\tilde{T}_\mathrm{BP}\right) - 2\frac{\tilde{\alpha}}{\tilde{W}_\mathrm{GC}}\left(\tilde{T}-\tilde{T}_\mathrm{BP}\right) + \Delta_\mathrm{lv}\tilde{H}\,\dot{\tilde{m}}$$
$$- \frac{\tilde{\alpha}_\mathrm{GDL}}{\tilde{H}_\mathrm{GC}}\left(\tilde{T}-\tilde{T}_\mathrm{GDL}\right) - \frac{\tilde{W}_\mathrm{GDL}}{\tilde{W}_\mathrm{GC}\tilde{H}_\mathrm{GC}}\left[\varepsilon\tilde{\rho}_\mathrm{GDL}\tilde{c}_\mathrm{p}\tilde{T}\tilde{u}_{2,\mathrm{GDL}} + \tilde{r}_{2,\mathrm{GDL}}\right], \quad (3.21)$$

where the last two RHS terms represent the coupling between the gas channel and GDL in terms of convective heat transfer as well as convective and diffusive enthalpy transport.

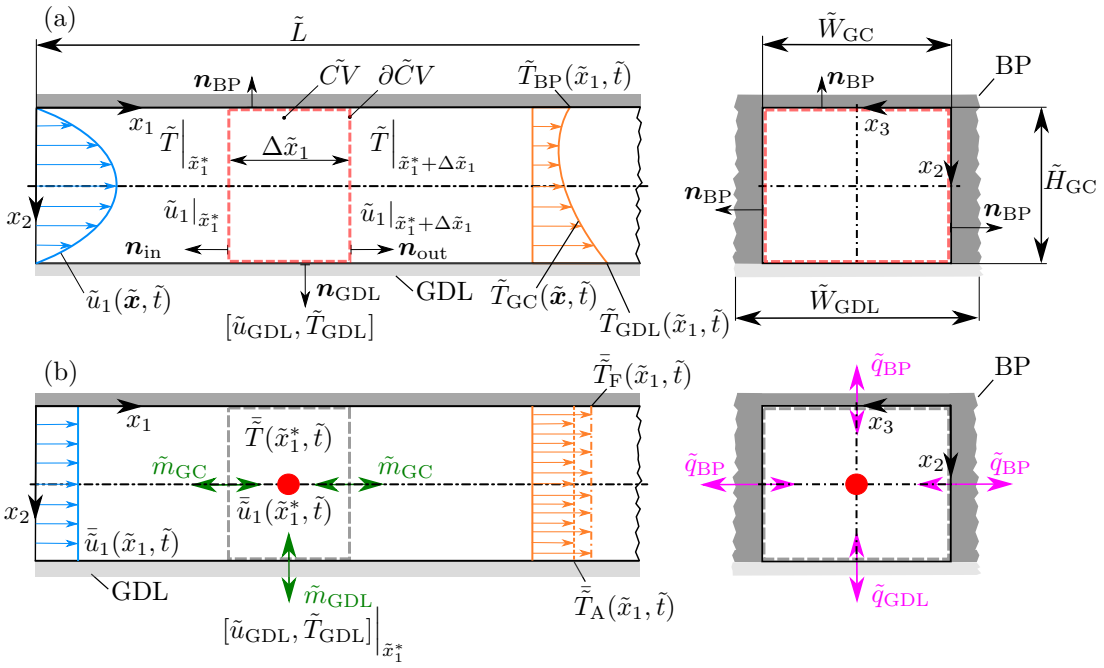

Figure 3: Schematic velocity and temperature distribution in the gas channel. (a) displays the paraboloid velocity and temperature distribution. (b) represents the quasi-1D formulation with cross-sectional averaged variables and the relevant mass (green) and heat (magenta) exchange of the $\tilde{CV}$.

Inserting the continuity equation, e.g. derived in [1], further simplifies eq. (3.21) and introduction of characteristic reference values, see apendix C, finally yields the governing equation in dimensionless form. The corresponding dimensionless groups of each term allow to identify negligible effects, e.g. thermal conduction in the fluid, to be omitted in the presented governing equations. Fig. 3b shows the relevant convective heat transfer, as well as the convective and diffusive mass transport mechanisms in magenta and green, respectively.

3.2.1 Governing equations

A detailed derivation of all the governing equations in the GC domain is given in appendix A.1. The corresponding dimensionless groups K are defined in appendix C. Summarising, with the use of characteristic reference values, the dimensionless form of the governing equations for the gas channels on both the the cathode and anode side can be written as:

Total mass balance:

$$\frac{\partial \rho}{\partial t} + \frac{\partial(\rho u_1)}{\partial x_1} = -K_{\mathrm{cm}}\, \varepsilon \rho_{\mathrm{GDL}} u_{2,\mathrm{GDL}}\,, \tag{3.22}$$

Liquid phase mass balance:

$$\frac{\partial s}{\partial t} + \frac{\partial(s u_1)}{\partial x_1} = \dot{m} - K_{\mathrm{cl1}}\, \psi_{2,\mathrm{GDL}} - K_{\mathrm{cl2}}\, \varepsilon\, \zeta_{\mathrm{GDL}} \rho_{\mathrm{GDL}} u_{2,\mathrm{GDL}}\,, \tag{3.23}$$

Species mass balances, $\beta = \mathrm{O_2/H_2}$:

$$(1-s)\rho_{\mathrm{g}} \left[\frac{\partial \xi_{\mathrm{g}}^{\beta}}{\partial t} + u_1 \frac{\partial \xi_{\mathrm{g}}^{\beta}}{\partial x_1} \right] = -K_{\mathrm{cs1}} \frac{\partial j_1^{\beta}}{\partial x_1} + K_{\rho}\, \xi_{\mathrm{g}}^{\beta} \dot{m} - K_{\mathrm{cs2}}\, j_{2,\mathrm{GDL}}^{\beta}\,, \tag{3.24}$$

$$(1-s)\rho_{\mathrm{g}} \left[\frac{\partial \xi_{\mathrm{g}}^{\mathrm{H_2O}}}{\partial t} + u_1 \frac{\partial \xi_{\mathrm{g}}^{\mathrm{H_2O}}}{\partial x_1} \right] = -K_{\mathrm{cs1}} \frac{\partial j_1^{\mathrm{H_2O}}}{\partial x_1} - K_{\rho} \left(1 - \xi_{\mathrm{g}}^{\mathrm{H_2O}}\right) \dot{m} - K_{\mathrm{cs2}}\, j_{2,\mathrm{GDL}}^{\mathrm{H_2O}}\,, \tag{3.25}$$

Energy balance:

$$\begin{aligned} \rho \frac{\partial (c_{\mathrm{p}} T)}{\partial t} + \rho u_1 \frac{\partial (c_{\mathrm{p}} T)}{\partial x_1} = &-K_{\mathrm{ce1}} \frac{\partial (T j_1^{\beta})}{\partial x_1} - K_{\mathrm{ce2}} \frac{\partial (T j_1^{\mathrm{H_2O}})}{\partial x_1} - K_{\mathrm{ce3}} (T - T_{\mathrm{BP}}) - 2\, K_{\mathrm{ce4}} (T - T_{\mathrm{BP}}) \\ &- K_{\mathrm{ce5}} (T - T_{\mathrm{GDL}}) + K_{\mathrm{ce6}}\, \dot{m} - K_{\mathrm{ce7}}\, T j_{2,\mathrm{GDL}}^{\beta} - K_{\mathrm{ce8}}\, T j_{2,\mathrm{GDL}}^{\mathrm{H_2O}}\,, \end{aligned} \tag{3.26}$$

Momentum balance:

$$\frac{\partial(\rho u_1)}{\partial t} + F_{u^2} \frac{\partial(\rho u_1^2)}{\partial x_1} + \frac{\partial p_{\mathrm{g}}}{\partial x_1} = -K_{\mathrm{cu}}\, \mu_{\mathrm{g}} u_1\,, \tag{3.27}$$

Equation of state:

$$p_{\mathrm{g}} = K_{\mathrm{ceos}}\, T \rho_{\mathrm{g}} \sum_{\alpha} \frac{\xi_{\mathrm{g}}^{\alpha}}{M^{\alpha}}\,, \tag{3.28}$$

Closure equation:

$$\sum_{\alpha} \xi_{\mathrm{g}}^{\alpha} = 1\,, \tag{3.29}$$

Multiphase mixture density:

$$\rho = \frac{1}{K_{\rho}}\, s + \rho_{\mathrm{g}} (1 - s)\,. \tag{3.30}$$

Here, F_{u^2} is the shape factor for fully developed laminar flow in a rectangular duct, [1], and M^α denotes the molar mass of species α.

In total, the GC model consists of nine coupled non-linear governing equations. Six of which are partial differential equations (PDEs) for mass, heat and momentum transfer. The other three are algebraic expressions for the equation of state, the gas mass fraction closure condition and multiphase mixture (MM) density ρ. If the liquid water saturation s, eq. (3.12), is calculated in an explicit manner from previous time step variables, nine unknowns are identified:

- velocity u_1,
- pressure p,
- gas density ρ_g,
- β mass fraction ξ_g^β,
- N_2 mass fraction $\xi_\mathrm{g}^{\mathrm{O}_2}$,
- H_2O mass fraction $\xi_\mathrm{g}^{\mathrm{H_2O}}$,
- temperature T,
- MM density ρ,
- mass transfer rate $\dot{m}$.

The last column represent the additional unknowns for the non-isothermal multiphase flow extension to the Murschenhofer et al. model [1]. Newly added equations are the liquid phase mass balance, eq. (3.23), energy balance, eq. (3.26), and the expression for the MM density, eq. (3.30).

3.3 Gas diffusion layer

The multiphase mixture model in capillary porous media (MMM) , [8], is used to describe multiphase flow phenomena in the GDL domain. Due to the absence of side walls within a GDL slice, the velocity and temperature profile is assumed to be constant in x_1 and x_3-direction. Therefore, within the quasi-2D concept the GDL can immediately be treated 1D for each slice and all variables depend on x_2 only.

The kinematic viscosity $\tilde{\nu}$ of the multiphase mixture is computed from eq. (2.30),

$$\tilde{\nu} = \left(\frac{\kappa_{\mathrm{r_l}}}{\tilde{\nu}_\mathrm{l}} + \frac{\kappa_{\mathrm{r_g}}}{\tilde{\nu}_\mathrm{g}} \right)^{-1} . \tag{3.31}$$

The kinematic viscosity of the gas phase $\tilde{\nu}_\mathrm{g}$ is obtained from the relation $\tilde{\mu}_\mathrm{g} = \tilde{\rho}_\mathrm{g}\tilde{\nu}_\mathrm{g}$, since a model to calculate the dynamic viscosity of the gas phase $\tilde{\mu}_\mathrm{g}$ is already implemented in the singlephase model, [1]. In the present work, it is assumed that the relative permeabilities of the liquid phase $\kappa_{\mathrm{r_l}}$ and gas phase $\kappa_{\mathrm{r_g}}$ are proportional to the cube of phase saturations, [18]. Hence,

$$\kappa_{\mathrm{r_l}} = s^3 , \qquad \kappa_{\mathrm{r_g}} = (1-s)^3 . \tag{3.32}$$

With the relative permeability of the liquid phase $\kappa_{\mathrm{r_l}}$, the mobility of the liquid phase ζ is calculated from eq. (2.31) to yield

$$\zeta = \frac{s^3}{\tilde{\nu}_\mathrm{l}} \tilde{\nu} . \tag{3.33}$$

Capillary, solutal- and thermal-capillary effects on the multiphase mixture pressure $\tilde{p}$, defined in eq. (2.40), are found to be negligible wihtin the scope of this model. Hence, the multiphase mixture pressure is set to be equal to the gas phase pressure, $\tilde{p} = \tilde{p}_\mathrm{g}$. To capture multiphase transport processes in the GDL however, the gradient of the capillary pressure $\tilde{p}_\mathrm{c}$ becomes relevant. For the two-phase system at hand, the capillary pressure can be expressed as a function of the surface

tension $\tilde{\varsigma}_\mathrm{l}$ of liquid water, contact angle θ_c between GDL material and liquid water, GDL porosity ε, as well as GDL total permeability $\tilde{\kappa}$ and liquid saturation s, [18],

$$\tilde{p}_\mathrm{c} = \tilde{\varsigma}_\mathrm{l} \cos(\theta_\mathrm{c}) \left(\frac{\varepsilon}{\tilde{\kappa}}\right)^{1/2} J(s)\,. \tag{3.34}$$

The Leverett J-function $J(s)$ further depends on whether the porous material is hydrophilic, $\theta_\mathrm{c} < 90°$, or hydrophobic, $\theta_\mathrm{c} > 90°$. It reads

$$J(s) = \begin{cases} 1.417(1-s) - 2.120(1-s)^2 + 1.263(1-s)^3, & \theta_c < 90°\,, \\ 1.417s - 2.120s^2 + 1.263s^3, & \theta_c > 90°\,. \end{cases} \tag{3.35}$$

With the help of eq. (2.43) one finds the liquid phase capillary diffusion flux $\tilde{\psi}$ in the GDL

$$\tilde{\psi}_2 = \frac{\sqrt{\varepsilon\tilde{\kappa}}\,\cos(\theta_\mathrm{c})\,\tilde{\varsigma}_\mathrm{l}}{\tilde{\nu}}\,\zeta(1-\zeta)\,J'(s)\,\frac{\partial s}{\partial \tilde{x}_2}\,, \tag{3.36}$$

where $J'(s)$ represents the derivative of the Leverett J-function with respect to s, which is given by

$$J'(s) = \begin{cases} -0.966 + 3.338s - 3.789s^2 & \theta_c < 90°\,, \\ 1.417 - 4.24s + 3.789s^2 & \theta_c > 90°\,. \end{cases} \tag{3.37}$$

Finally, the necessary correction factors for the species advection of reactants β and H_2O, as well as enthalpy fluxes read

$$\gamma_\beta = \frac{\tilde{\rho}\,(1-\zeta)}{\tilde{\rho}_\mathrm{g}\,(1-s)}\,, \tag{3.38}$$

$$\gamma_{\mathrm{H_2O}} = \frac{\tilde{\rho}\left(\zeta + (1-\zeta)\,\xi_\mathrm{g}^{\mathrm{H_2O}}\right)}{\tilde{\rho}_\mathrm{l}\,s + \tilde{\rho}_\mathrm{g}\,(1-s)\,\xi_\mathrm{g}^{\mathrm{H_2O}}}\,, \tag{3.39}$$

$$\gamma_\mathrm{h} = \frac{\tilde{\rho}\left(\zeta\,c_{\mathrm{p_l}} + (1-\zeta)\,c_{\mathrm{p_g}}\right)}{\tilde{\rho}_\mathrm{l}\,s\,c_{\mathrm{p_l}} + \tilde{\rho}_\mathrm{g}\,(1-s)\,c_{\mathrm{p_g}}}\,. \tag{3.40}$$

Although the equation of motion in the MMM is derived from Darcy's law, this work assumes the validity of the full momentum equation proposed in the single phase model [1], in which the additional pressure drop due to the GDL's porosity is considered by a source term. The single phase viscosity $\tilde{\mu}_\mathrm{g}$ is replaced by the multiphase mixture viscosity computed from eq. (3.31). A similar approach is found in the work by Pasaogullari and Wang, [18].

3.3.1 Governing equations

A detailed derivation for the governing equations in the GDL domain can be found in appendix A.2. The corresponding dimensionless groups are defined in appendix C. Summarising, with the use of characteristic reference values, the dimensionless form of the governing equations for the gas diffusion layers can be written as:

Total mass balance:

$$\frac{\partial \rho}{\partial t} + \frac{\partial(\rho u_2)}{\partial x_2} = 0\,, \tag{3.41}$$

Liquid phase mass balance:

$$\frac{\partial s}{\partial t} + K_\rho \frac{\partial(\zeta \rho u_2)}{\partial x_2} = \dot{m} - \frac{K_{\mathrm{gl}}}{\varepsilon} \frac{\partial \psi_2}{\partial x_2}\,, \tag{3.42}$$

Species mass balances, $\beta = \mathrm{O_2/H_2}$:

$$\varepsilon \left[\frac{\partial(\rho_\mathrm{g}(1-s)\xi_\mathrm{g}^\beta)}{\partial t} + \frac{\partial(\gamma_\beta \rho_\mathrm{g}(1-s)\xi_\mathrm{g}^\beta u_2)}{\partial x_2} \right] = -\frac{\partial j_2^\beta}{\partial x_2} + K_{\mathrm{gs}} \frac{\partial(\xi_\mathrm{g}^\beta \psi_2)}{\partial x_2}\,, \tag{3.43}$$

$$\begin{aligned} \frac{\varepsilon}{K_\rho} \left[\frac{\partial s}{\partial t} + \frac{\partial(\gamma_{\mathrm{H_2O}} s u_2)}{\partial x_2} \right] + \varepsilon \left[\frac{\partial(\rho_\mathrm{g}(1-s)\xi_\mathrm{g}^{\mathrm{H_2O}})}{\partial t} + \frac{\partial(\gamma_{\mathrm{H_2O}} \rho_\mathrm{g}(1-s)\xi_\mathrm{g}^{\mathrm{H_2O}} u_2)}{\partial x_2} \right] = \\ - \frac{\partial j_2^{\mathrm{H_2O}}}{\partial x_2} - K_{\mathrm{gs}} \frac{\partial}{\partial x_2}\big((1-\xi_\mathrm{g}^{\mathrm{H_2O}})\psi_2\big)\,, \end{aligned} \tag{3.44}$$

Energy balance:

$$\begin{aligned} K_{\mathrm{ge1}}\,(1-\varepsilon)\,\frac{\partial T}{\partial t} + \varepsilon \left[\frac{\partial(\rho c_\mathrm{p} T)}{\partial t} + \frac{\partial(\gamma_\mathrm{h} \rho c_\mathrm{p} T u_2)}{\partial x_2} \right] = -K_{\mathrm{ge2}} \frac{\partial(T j_2^\beta)}{\partial x_2} - K_{\mathrm{ge3}} \frac{\partial(T j_2^{\mathrm{H_2O}})}{\partial x_2} \\ + K_{\mathrm{ge4}} \frac{\partial}{\partial x_2} \left(k_{\mathrm{eff}} \frac{\partial}{\partial x_2} T \right) + K_{\mathrm{ge5}}\,\varepsilon\,\dot{m} - K_{\mathrm{ge6}} \frac{\partial(T\psi_2)}{\partial x_2} + K_{\mathrm{ge7}} \frac{\partial(c_{\mathrm{p_g}} T \psi_2)}{\partial x_2}\,, \end{aligned} \tag{3.45}$$

Momentum balance:

$$\frac{\partial(\rho u_2)}{\partial t} + F_{u^2} \frac{\partial(\rho u_2^2)}{\partial x_2} + \frac{\partial p}{\partial x_2} = -K_{\mathrm{gu1}}\,\mu u_2 + K_{\mathrm{gu2}} \frac{\partial}{\partial x_2} \left(\mu \frac{\partial u_2}{\partial x_2} \right), \tag{3.46}$$

Equation of state:

$$p = K_{\mathrm{geos}}\, T \rho_\mathrm{g} \sum_\alpha \frac{\xi_\mathrm{g}^\alpha}{M^\alpha}\,, \tag{3.47}$$

Closure equation:

$$\sum_\alpha \xi_\mathrm{g}^\alpha = 1\,, \tag{3.48}$$

Multiphase mixture density:

$$\rho = \frac{1}{K_\rho}\, s + \rho_\mathrm{g}(1-s)\,. \tag{3.49}$$

As in the GC, the GDL model consists of six PDEs for mass, heat and momentum transfer, and three algebraic expressions for the equation of state, the gas mass fraction closure condition and multiphase mixture (MM) density ρ. If the liquid water saturation s, eq. (3.12), is calculated in an explicit manner from previous time step variables, nine unknowns are identified:

- velocity u_2,
- β mass fraction ξ_{g}^{β},
- temperature T,
- pressure p,
- N_2 mass fraction $\xi_{\mathrm{g}}^{\mathrm{O_2}}$,
- MM density ρ,
- gas density ρ_{g},
- H_2O mass fraction $\xi_{\mathrm{g}}^{\mathrm{H_2O}}$,
- mass transfer rate $\dot{m}$.

The dimensionless form of the Fickian diffusion fluxes that appear in the governing equations of the GC, $a = 1$, and GDL, $a = 2$, read

$$j_a^{\beta} = -(\varepsilon(1-s))^q \rho_{\mathrm{g}} \left(\mathcal{D}_{\beta,\beta} \frac{\partial \xi_{\mathrm{g}}^{\beta}}{\partial x_a} + \mathcal{D}_{\beta,\mathrm{H_2O}} \frac{\partial \xi_{\mathrm{g}}^{\mathrm{H_2O}}}{\partial x_a} \right), \tag{3.50}$$

$$j_a^{\mathrm{H_2O}} = -(\varepsilon(1-s))^q \rho_{\mathrm{g}} \left(\mathcal{D}_{\mathrm{H_2O},\beta} \frac{\partial \xi_{\mathrm{g}}^{\beta}}{\partial x_a} + \mathcal{D}_{\mathrm{H_2O},\mathrm{H_2O}} \frac{\partial \xi_{\mathrm{g}}^{\mathrm{H_2O}}}{\partial x_a} \right), \tag{3.51}$$

whereas the third flux is used to close the system,

$$j_a^{\beta} + j_a^{\mathrm{H_2O}} + j_a^{\mathrm{N_2}} = 0\,. \tag{3.52}$$

Furthermore, the dimensionless form of the capillary diffusion flux, found in the GDL governing equations and GC-GDL coupling conditions, is given by

$$\psi_2 = \frac{\zeta(1-\zeta)}{\nu} J'(s) \frac{\partial s}{\partial x_2}\,. \tag{3.53}$$

3.4 Membrane

The model for water and nitrogen transport in the membrane, adopted from Murschenhofer et al. [1], is further developed to also account for conservation of energy and to resolve the temperature field within the PEM.

3.4.1 Mass transport

Within the membrane, water transport is driven by electro-osmotic drag, proportional to the current density $\tilde{i}$, and diffusion due to concentration gradients. Convective transport caused by pressure differences plays a minor role in PEMFCs and is therefore neglected. Hence, the membrane water flux $\tilde{j}_{\mathrm{w}}$ reads

$$\tilde{j}_{\mathrm{w}} = -\tilde{M}_{\mathrm{H_2O}} \left(C_{\mathrm{drag}}(\lambda) \frac{\tilde{i}}{\tilde{F}} + \frac{\tilde{\rho}_{\mathrm{PEM}}}{\tilde{\mathrm{EW}}} \tilde{D}_{\mathrm{w}}(\lambda) \frac{\partial \lambda}{\partial \tilde{x}_2} \right), \tag{3.54}$$

[1]. The chosen orientation of the coordinate system leads to a negative membrane water crossover from anode to cathode and a positive one vice versa. The electro-osmotic drag coefficient C_{drag} and water diffusion coefficient $\tilde{\mathcal{D}}_{\mathrm{w}}$ are functions of the normalised water content λ, which is defined as the number of water molecules per sulfonic acid groups present in the polymer, $\lambda = n_{\mathrm{H_2O}}/n_{\mathrm{SO_3H}}$.

Based on a general conservation law of the form given in equation (3.63), with $\tilde{j}_{\mathrm{w}}$ as the only transport mechanism, one finds the dimensionless formulation of the normalised membrane water content transport equation, [1],

$$\frac{\partial \lambda}{\partial t} = K_{\mathrm{mw}} \frac{\partial \lambda}{\partial x_2} i + \left(\frac{\partial \lambda}{\partial x_2} \right)^2 + \lambda \frac{\partial^2 \lambda}{\partial x_2^2}\,. \tag{3.55}$$

The membrane is also permeable for N_2, with the concentration gradient as the driving force. A linear distribution of N_2 accross the membrane is assumed. By this an additional transport equation in the PEM domain is avoided and the cross-over flux $\tilde{j}^{N_2}_{cross}$ appears as a coupling condition at the GDL-PEM interface only, [1]:

$$\tilde{j}^{N_2}_{cross} = \tilde{M}^{N_2} \tilde{k}_{N_2}(\lambda) \frac{\tilde{p}^{C}_{N_2} - \tilde{p}^{A}_{N_2}}{\tilde{H}_{PEM}} \,. \tag{3.56}$$

Here, $\tilde{p}^{C}_{N_2}$ and $\tilde{p}^{A}_{N_2}$ denote the N_2 partial pressure at the cathode and anode side, respectively. $\tilde{k}_{N_2}$ is the membrane permeance of N_2, also a function of λ, [1], and $\tilde{H}_{PEM}$ is the membrane height.

3.4.2 Energy transport

The energy balance within the PEM domain is found from evaluating the 3D integral conservation law

$$\int_{\tilde{CV}} \left(\tilde{\rho}_{PEM}\, \tilde{c}_p^{PEM} \frac{\partial \tilde{T}}{\partial \tilde{t}} + \frac{\tilde{\rho}_{PEM} \tilde{M}^{H_2O}}{E\tilde{W}} \tilde{c}_p^{w} \frac{\partial(\lambda \tilde{T})}{\partial \tilde{t}} \right) d\tilde{V} + \oint_{\partial \tilde{CV}} \tilde{c}_p^{w}\, \tilde{T}\, \tilde{\boldsymbol{j}}_w \cdot \boldsymbol{n}\, d\tilde{S} = \\ + \oint_{\partial \tilde{CV}} \left(\tilde{k}_{PEM}(\lambda)\, \tilde{\nabla} \tilde{T} \right) \cdot \boldsymbol{n}\, d\tilde{S} + \int_{\tilde{CV}} \frac{\tilde{i}^2}{\tilde{\sigma}(\lambda, \tilde{T})}\, d\tilde{V} \,, \tag{3.57}$$

for a control volume $\tilde{CV}$ fixed in space, similarly to the approach in eq. (3.21). The first LHS integral accounts for the accumulated enthalpy in the dry membrane (left) and additional enthalpy due to a certain water content λ (right). Considering the discussion of PEM water uptake in the work of Ramousse et al. [4], the specific heat capacity of the water phase $\tilde{c}_p^{w}$ is assumed to be equal to that of liquid water. Enthalpy transport is only due to electro-osmotic drag and diffusion of membrane water. Dimensional analysis confirms the negligibility of resolving nitrogren (enthalpy) transport in the PEM.

An empirical, linear function proposed by Burheim et al. [19] is used to relate the thermal conductivity of the PEM $\tilde{k}_{PEM}$ to the membrane water content λ,

$$\tilde{k}_{PEM}(\lambda) = 0.177 + 3.7 \times 10^{-3} \lambda \left[\frac{W}{m\,K} \right] . \tag{3.58}$$

The rightmost integral represents the heat source term due to the Joule effect. The correlation of PEM proton conductivity $\tilde{\sigma}$, membrane hydration and temperature is adopted from [1] and reads

$$\tilde{\sigma} = (-0.326 f_{PEM,1} + 0.5139 f_{PEM,2} \lambda) \exp\left(\frac{1286}{303} - \frac{1286K}{\tilde{T}} \right) \left[\frac{S}{m} \right] , \tag{3.59}$$

where $f_{PEM,1}$ and $f_{PEM,2}$ are fitting parameters which enable the adjustment of the model to a specific FC.

By means of characteristic reference quantities, the dimensionless formulation of the PEM energy balance then yields

$$K_{me1} \frac{\partial T}{\partial t} + \frac{\partial(\lambda T)}{\partial t} = K_{me2}\, i\, \frac{\partial(\lambda T)}{\partial x_2} + \frac{\partial}{\partial x_2} \left(\lambda T \frac{\partial \lambda}{\partial x_2} \right) - K_{me3} \frac{\partial}{\partial x_2} \left(k_{PEM} \frac{\partial T}{\partial x_2} \right) + K_{me4} \frac{i^2}{\sigma} \,. \tag{3.60}$$

Hence, the extended PEM model consists of two non-linear PDEs, which are solved for the variables temperature T and normalised membrane water content λ.

3.5 Electrochemical model

The electrochemical model from Murschenhofer et al. [1] remains unchanged for the multiphase extension and is summarised in the following. Due to the non-isothermal model formulation the temperature $\tilde{T}$ is an intrinsic unknown and thus must be accounted for in the linearisation of the equations, see section 4.2.

As shown in eq. (1.18) the cell potential $\tilde{E}_{\text{cell}}$ is computed by subtracting electrochemical activation losses and Ohmic losses from the open-circuit cell potential $\tilde{E}_{\text{OC}}$

$$\tilde{E}_{\text{cell}} = \tilde{E}_{\text{OC}} - \frac{\tilde{\mathcal{R}}\tilde{T}}{\alpha_{\text{C}}\tilde{F}} \ln\left(\frac{\tilde{i}}{\tilde{i}_0}\right) - \tilde{i}\int_0^{\tilde{H}_{\text{PEM}}} \frac{\mathrm{d}\tilde{x}_2}{\tilde{\sigma}(\lambda)} \,. \tag{3.61}$$

Here, the exchange current density $\tilde{i}_0$ is defined as

$$\tilde{i}_0 = \tilde{i}_{0,r}\tilde{a}_{\text{C}}\tilde{L}_{\text{C}}\left(\frac{\tilde{p}^{\text{O}_2}}{\tilde{p}_r^{\text{O}_2}}\right)^{\gamma_{\text{C}}} \exp\left[-\frac{\tilde{E}_{\text{act}}}{\tilde{\mathcal{R}}\tilde{T}}\left(1 - \frac{\tilde{T}}{\tilde{T}_{0,r}}\right)\right] . \tag{3.62}$$

The parameters $i_{0,r}$, α_{C}, $\tilde{a}_{\text{C}}$ and γ_{C} are further fitting parameters to adjust the polarisation curve of the PEMFC model.

3.6 Coupling conditions

On the anode and the cathode side, the associated models for the GC and GDL are governed by a system of nine coupled equations, six PDEs and three algebraic equations. Two additional PDEs describe the water transport and conservation of energy in the membrane. The electro-chemical model is governed by one PDE and one algebraic equation. These model equations are valid in different domains and must be merged by appropriate coupling conditions at the corresponding interfaces.

The coupling of the conservation laws (PDEs) is achieved by following Kotchine's theorem, [20]: At a surface of discontinuity $\tilde{\mathcal{S}}$, which separates the total control volume $\tilde{CV}$ into two partial control volumes $\tilde{CV}_1$ and $\tilde{CV}_2$, application of a general balance equation of the form

$$\frac{\mathrm{d}}{\mathrm{d}t}\int_{\tilde{CV}} \tilde{\rho}\tilde{\phi}\,\mathrm{d}\tilde{V} + \oint_{\partial\tilde{CV}} \tilde{\theta}\tilde{\phi}\,\mathrm{d}\tilde{S} = \int_{\tilde{CV}} \tilde{\rho}\tilde{\Psi}\,\mathrm{d}\tilde{V} + \oint_{\partial\tilde{CV}} \tilde{\Sigma}\,\mathrm{d}\tilde{S} \tag{3.63}$$

to both, the total control volume $\tilde{CV}$ and the partial ones, $\tilde{CV}_1$ and $\tilde{CV}_2$, yields the jump condition

$$\tilde{\Sigma}_2 - \tilde{\Sigma}_1 = \tilde{\theta}_2\tilde{\phi}_2 - \tilde{\theta}_1\tilde{\phi}_1 \,. \tag{3.64}$$

Here, $\tilde{\rho}\tilde{\phi}$, $\tilde{\rho}\tilde{\Psi}$, $\tilde{\Sigma}$ denote a generalised density, generalised (volumetric) force and generalised flux perpendicular to the closed surface, respectively, and $\tilde{\theta}$ is the mass flow density

$$\tilde{\theta} = \tilde{\rho}\,(\tilde{\boldsymbol{v}} - \tilde{\boldsymbol{v}}_{\text{CV}}) \cdot \boldsymbol{n} \,, \tag{3.65}$$

with control volume velocity $\tilde{\boldsymbol{v}}_{\text{CV}}$ ($= 0$ in the present work) and normal unit vector $\tilde{\boldsymbol{n}}$ on the closed surface $\partial\tilde{CV}$. $\Sigma_2 - \Sigma_1$ and $\tilde{\theta}_2\tilde{\phi}_2 - \tilde{\theta}_1\tilde{\phi}_1$ represent the jump of the respective quantity at $\tilde{\mathcal{S}}$. The corresponding variables for the present work are identified directly from the integral versions of the conservation laws derived in section 2.

3.6.1 Interface BP-GC-GDL

The quasi-1D GC model already takes into account the coupling of mass flows at the interface due to the integral formulation of the conservation of multiphase mixture mass, liquid phase mass and species. The coupling of heat fluxes however, is more elaborate as their distribution in the (x_2, x_3)-plane must be accounted for: One part of the heat flux emitted by the GDL is conducted directly to the BP, while the remaining part, together with mass and enthalpy, is transferred to the GC. The situation is depicted in figure 4.

Due to the high thermal conductivity, the temperature in the BPs, $\tilde{T}_{\mathrm{BP}}$, is assumed to be constant along the x_2- and x_3-direction and further serves as a boundary condition. As a result of the quasi-2D model formulation, temperature at the BP-GC-GDL interface is discontinuous in general

$$\tilde{T}_{\mathrm{BP}} \neq \tilde{T}_{\mathrm{GC}} \neq \tilde{T}_{\mathrm{GDL}} \,. \tag{3.66}$$

The temperature jump will strongly depend on the geometry of the interface at hand, which is accounted for parametrically due to the model formulation based on 3D integral conservation laws.

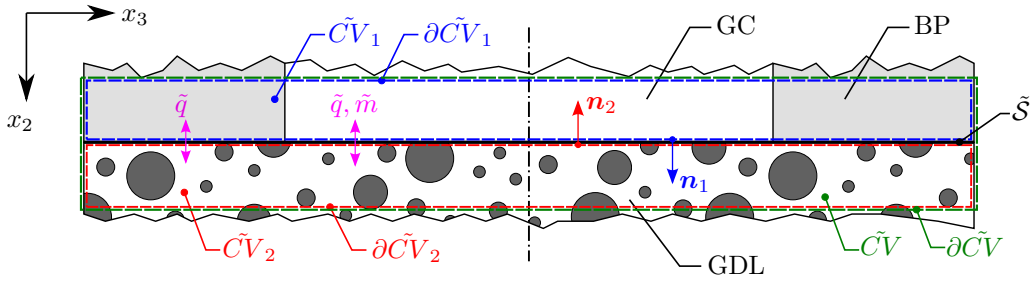

Figure 4: BP-GC-GDL interface at the cathode side, representing a surface of discontinuity $\tilde{\mathcal{S}}$ and the respective (partial) control volumes for the derivation of the coupling conditions using Kotchine's theorem.

However, the variable values for the pressure and gas species mass fractions in the GC and GDL are equal at $\tilde{\mathcal{S}}$:

$$\tilde{p}_{\mathrm{GC}} = \tilde{p}_{\mathrm{GDL}} \,, \qquad \tilde{\xi}^{\alpha}_{\mathrm{g,GC}} = \tilde{\xi}^{\alpha}_{\mathrm{g,GDL}} \,. \tag{3.67}$$

Since $\tilde{T}_{\mathrm{GC}} \neq \tilde{T}_{\mathrm{GDL}}$, densities, liquid saturations and multiphase mixture species mass fractions have to be determined from the corresponding constitutive relationships.

Applying Kotchine's theorem (3.64) to the energy balance yields the coupling condition at the BP-GC-GDL interface for both the cathode and anode side:

$$\begin{aligned} &- \tilde{q}_{\mathrm{GDL}} + \tilde{q}^{i}_{\mathrm{BP}} + \tilde{q}^{i}_{\mathrm{GC}} - \tilde{j}^{\beta}\Big(\tilde{c}^{\beta}_{\mathrm{p_g}} - \tilde{c}^{\mathrm{N_2}}_{\mathrm{p_g}}\Big)\Big(\tilde{T}_{\mathrm{GDL}} - \tilde{T}_{\mathrm{GC}}\Big) - \tilde{j}^{\mathrm{H_2O}}\Big(\tilde{c}^{\mathrm{H_2O}}_{\mathrm{p_g}} - \tilde{c}^{\mathrm{N_2}}_{\mathrm{p_g}}\Big)\Big(\tilde{T}_{\mathrm{GDL}} - \tilde{T}_{\mathrm{GC}}\Big) \\ &\quad - \tilde{\psi}\tilde{c}_{\mathrm{p_l}}\Big(\tilde{T}_{\mathrm{GDL}} - \tilde{T}_{\mathrm{GC}}\Big) + \tilde{\psi}\tilde{c}_{\mathrm{p_g}}\Big(\tilde{T}_{\mathrm{GDL}} - \tilde{T}_{\mathrm{GC}}\Big) = \varepsilon\gamma_{\mathrm{h}}\tilde{\rho}\tilde{u}_2\Big(\tilde{c}_{\mathrm{p,GDL}}\tilde{T}_{\mathrm{GDL}} - \tilde{c}_{\mathrm{p,GC}}\tilde{T}_{\mathrm{GC}}\Big) \,. \end{aligned} \tag{3.68}$$

The corresponding heat fluxes at the interface are

$$\tilde{q}^{\mathrm{C}}_{\mathrm{BP}} = \frac{\tilde{W}_{\mathrm{BP}}}{\tilde{W}_{\mathrm{GDL}}}\frac{1}{\tilde{R}_{\mathrm{c}}}\Big(\tilde{T}_{\mathrm{BP}} - \tilde{T}_{\mathrm{GDL}}\Big) \,, \qquad \tilde{q}^{\mathrm{C}}_{\mathrm{GC}} = \frac{\tilde{W}_{\mathrm{GC}}}{\tilde{W}_{\mathrm{GDL}}}\tilde{\alpha}\Big(\tilde{T}_{\mathrm{GC}} - \tilde{T}_{\mathrm{GDL}}\Big) \,, \qquad \tilde{q}_{\mathrm{GDL}} = -\tilde{k}_{\mathrm{eff}}\frac{\partial\tilde{T}_{\mathrm{GDL}}}{\partial\tilde{x}_2} \,, \tag{3.69}$$

where the thermal contact resistance (TCR) $\tilde{R}_c$ between BP and GDL, [21], and the convective heat transfer between GC and GDL are accounted for, [17]. Due to the orientation of the coordinate system, $\tilde{q}^{\mathrm{C}}_{\mathrm{BP}} = -\tilde{q}^{\mathrm{A}}_{\mathrm{BP}}$ and $\tilde{q}^{\mathrm{C}}_{\mathrm{GC}} = -\tilde{q}^{\mathrm{A}}_{\mathrm{GC}}$.

3.6.2 Interface GDL-PEM

The catalyst layers are assumed to be infinitely thin and therefore the source terms accounting for the electrochemical half-cell reactions and sorption mechanisms appear at the interface GDL-PEM, directly at a surface of discontinuity $\tilde{\mathcal{S}}$. It is assumed that there are no convective fluxes through the PEM, only the water flux due to electro-osmotic drag and diffusion, as well as nitrogen crossover. The total mass flux of species α in the GDL domains, driven by convection, capillary diffusion and Fickian diffusion, is given by

$$\tilde{j}^{\alpha}_{\mathrm{tot}} = \varepsilon\gamma_{\alpha}\xi^{\alpha}\tilde{\rho}\tilde{u}_2 + \left(\xi^{\alpha}_{\mathrm{l}} - \xi^{\alpha}_{\mathrm{g}}\right)\tilde{\psi}_2 + \tilde{j}^{\alpha}_2 \,. \tag{3.70}$$

For the total flux of liquid water ($\xi^{\mathrm{H_2O}}_{\mathrm{l}} = 1$) follows

$$\tilde{j}^{\mathrm{H_2O}}_{\mathrm{l}} = \tilde{\psi}_2 + \varepsilon\zeta\tilde{\rho}\tilde{u}_2 \,. \tag{3.71}$$

Applying Kotchine's theorem (3.64) to the conservation equations for the species α and the liquid phase yields the coupling conditions for mass fluxes on the cathode side:

$$\tilde{j}^{\mathrm{O_2}}_{\mathrm{tot}} = \frac{\tilde{i}\tilde{M}^{\mathrm{O_2}}}{4\tilde{F}} \,, \qquad \tilde{j}^{\mathrm{N_2}}_{\mathrm{tot}} = \tilde{j}^{\mathrm{N_2}}_{\mathrm{cross}} \,, \qquad \tilde{j}^{\mathrm{H_2O}}_{\mathrm{tot}} = \tilde{j}_{\mathrm{w}} - \frac{\tilde{i}\tilde{M}^{\mathrm{H_2O}}}{2\tilde{F}} \,, \qquad \tilde{j}^{\mathrm{H_2O}}_{\mathrm{l}} = s\left(\tilde{j}_{\mathrm{w}} - \frac{\tilde{i}\tilde{M}^{\mathrm{H_2O}}}{2\tilde{F}}\right) . \tag{3.72}$$

Similarly follows for the anode side:

$$\tilde{j}^{\mathrm{H_2}}_{\mathrm{tot}} = -\frac{\tilde{i}\tilde{M}^{\mathrm{H_2}}}{2\tilde{F}} \,, \qquad \tilde{j}^{\mathrm{N_2}}_{\mathrm{tot}} = \tilde{j}^{\mathrm{N_2}}_{\mathrm{cross}} \,, \qquad \tilde{j}^{\mathrm{H_2O}}_{\mathrm{tot}} = \tilde{j}_{\mathrm{w}} \,, \qquad \tilde{j}^{\mathrm{H_2O}}_{\mathrm{liq}} = s\tilde{j}_{\mathrm{w}} \,. \tag{3.73}$$

The GDLs and PEM are assumed to be in thermal equilibrium at the respective interfaces, $\tilde{T}_{\mathrm{GDL}} = \tilde{T}_{\mathrm{PEM}}$. For the coupling of the energy balances the enthalpy flux due to nitrogen crossover is found to be negligible. Again, Kotchine's theorem applied to the energy balance yields the respective coupling conditions. For the cathode side follows

$$\begin{aligned} &- \tilde{j}_{\mathrm{w}}\tilde{c}^{\mathrm{w}}_{\mathrm{p}}\tilde{T} - \tilde{q}_{\mathrm{PEM}} + \tilde{j}^{\mathrm{O_2}}(\tilde{c}^{\mathrm{O_2}}_{\mathrm{p_g}} - \tilde{c}^{\mathrm{N_2}}_{\mathrm{p_g}})\tilde{T} + \tilde{j}^{\mathrm{H_2O}}(\tilde{c}^{\mathrm{H_2O}}_{\mathrm{p_g}} - \tilde{c}^{\mathrm{N_2}}_{\mathrm{p_g}})\tilde{T} + \tilde{\psi}\left(\tilde{c}^{\mathrm{H_2O}}_{\mathrm{p_l}} - \tilde{c}_{\mathrm{p_g}}\right)\tilde{T} \\ &\qquad - \tilde{c}^{\mathrm{O_2}}_{\mathrm{p_g}}\tilde{T}\frac{\tilde{i}\tilde{M}^{\mathrm{O_2}}}{4\tilde{F}} + \tilde{c}^{\mathrm{H_2O}}_{\mathrm{p}}\tilde{T}\frac{\tilde{i}\tilde{M}^{\mathrm{H_2O}}}{2\tilde{F}} + \tilde{q}_{\mathrm{GDL}} + \tilde{q}^{\mathrm{C}}_{\mathrm{reac}} + \tilde{q}^{\mathrm{C}}_{\mathrm{pol}} + \tilde{q}^{\mathrm{C}}_{\mathrm{sorp}} = -\varepsilon\gamma_{\mathrm{h}}\tilde{\rho}\tilde{c}_{\mathrm{p}}\tilde{T}\tilde{u}_2 \,, \end{aligned} \tag{3.74}$$

and for the anode side follows

$$\begin{aligned} &- \tilde{j}^{\mathrm{H_2}}(\tilde{c}^{\mathrm{H_2}}_{\mathrm{p_g}} - \tilde{c}^{\mathrm{N_2}}_{\mathrm{p_g}})\tilde{T} - \tilde{j}^{\mathrm{H_2O}}(\tilde{c}^{\mathrm{H_2O}}_{\mathrm{p_g}} - \tilde{c}^{\mathrm{N_2}}_{\mathrm{p_g}})\tilde{T} - \tilde{\psi}\left(\tilde{c}^{\mathrm{H_2O}}_{\mathrm{p_l}} - \tilde{c}_{\mathrm{p_g}}\right)\tilde{T} - \tilde{q}_{\mathrm{GDL}} + \tilde{j}_{\mathrm{w}}\tilde{c}^{\mathrm{w}}_{\mathrm{p}}\tilde{T} + \tilde{q}_{\mathrm{PEM}} \\ &\qquad - \tilde{c}^{\mathrm{H_2}}_{\mathrm{p_g}}\tilde{T}\frac{\tilde{i}\tilde{M}^{\mathrm{H_2}}}{2\tilde{F}} + \tilde{q}^{\mathrm{A}}_{\mathrm{reac}} + \tilde{q}^{\mathrm{A}}_{\mathrm{sorp}} = \varepsilon\gamma_{\mathrm{h}}\tilde{\rho}\tilde{c}_{\mathrm{p}}\tilde{T}\tilde{u}_2 \,, \end{aligned} \tag{3.75}$$

where the heat fluxes due to thermal conduction in the PEM and GDL are given by

$$\tilde{q}_{\mathrm{PEM}} = -\tilde{k}_{\mathrm{PEM}}(\lambda)\,\frac{\partial\tilde{T}}{\partial\tilde{x}_2} \qquad \text{and} \qquad \tilde{q}_{\mathrm{GDL}} = -\tilde{k}_{\mathrm{GDL}}\,\frac{\partial\tilde{T}}{\partial\tilde{x}_2} \,. \tag{3.76}$$

The different amounts of created entropy for liquid and gaseous water product, $\Delta^i_{\text{reac}}\tilde{S}_\text{l}$ and $\Delta^i_{\text{reac}}\tilde{S}_\text{g}$, respectively, are accounted for in the heat flux source terms $\tilde{q}^\text{i}_{\text{reac}}$ of the corresponding electrode i,

$$\tilde{q}^i_{\text{reac}} = -T\Big(s\,\Delta^i_{\text{reac}}\tilde{S}_\text{l} + (1-s)\,\Delta^i_{\text{reac}}\tilde{S}_\text{g}\Big)\frac{\tilde{i}}{2\tilde{F}}\,. \tag{3.77}$$

Heat generated due to electrochemical activation $\tilde{q}^\text{C}_{\text{pol}}$ is calculated with equation (1.15). As mentioned previously, this term is comparatively small on the anode side and therefore neglected. However, the released heat during sorption and desorption of water vapour into and out of the membrane has to be considered. The corresponding heat flux at the cathode is

$$\tilde{q}^\text{C}_{\text{sorp}} = (1-s)\tilde{j}_\text{w}\Delta_{\text{sorp}}\tilde{h}\,. \tag{3.78}$$

Due to the orientation of the coordinate system, for the anode side follows

$$\tilde{q}^\text{A}_{\text{sorp}} = -(1-s)\tilde{j}_\text{w}\Delta_{\text{sorp}}\tilde{h}\,. \tag{3.79}$$

The discussed heat flux source terms in the energy balance coupling conditions at the GDL-PEM interface, as well as the Joule heat source in the PEM, are summarised in fig. 5.

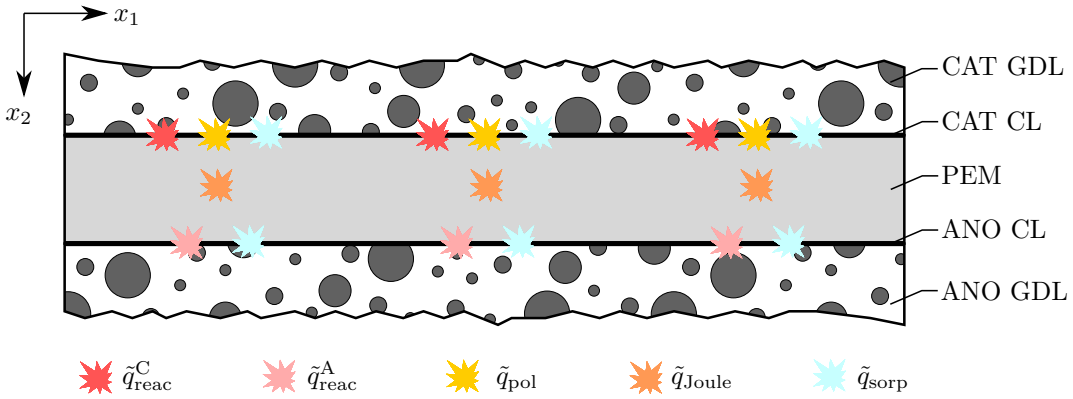

Figure 5: Heat flux source terms at the GDL-PEM interfaces and in the PEM.

Semi-empirical polynomial fits proposed by Springer et al. [5],

$$\lambda = \begin{cases} 0.043 + 17.81\,a_\text{w} - 39.85\,a_\text{w}^2 + 36.0\,a_\text{w}^3\,, & a_\text{w} \leq 1 \\ 14.0 + 1.4\,(a_\text{w} - 1)\,, & 1 < a_\text{w} \leq 3 \end{cases} \tag{3.80}$$

are used to relate the PEM water content λ to the GDL water vapour activity a_w, [2],

$$a_\text{w} = \frac{\tilde{p}^{\text{H}_2\text{O}}}{\tilde{p}_{\text{sat}}} + 2s\,. \tag{3.81}$$

The temperature $\tilde{T}$, computed from equations (3.74) and (3.75), and the normalised membrane water content λ, computed from equation (3.80), serve as Dirichlet boundary conditions on both membrane interfaces.

3.7 Boundary conditions

Various interchangeable PEMFC operating modes can be simulated with the present model by applying different sets of boundary conditions. In terms of mass transport, either mass driven or pressure driven operation is possible, prescribing the gas channel inlet velocity $\tilde{u}_{1,\mathrm{in}}$ or the inlet pressure $\tilde{p}_{\mathrm{in}}$. The outlet pressure is set as a boundary condition in both cases, e.g. to the ambient pressure $\tilde{p}_{\mathrm{amb}}$. Depending on the applied inlet temperature, the gas phase mass fractions $\tilde{\xi}_{\mathrm{g}}^{\alpha}$ are determined according to the desired gas relative humidity (RH). The BP temperature distribution in x_1-direction is used as a further boundary condition.

Additionally, the PEMFC can be operated in co- or counter-flow mode. For both cases anode dead-end operation with automated purging is possible, [1]. However, here only the pressure driven mode is practicable since a prescribed inlet velocity is physically not feasible.

For the electrochemical model, current and voltage driven operation is possible. For the latter, a uniform cell potential $\tilde{E}_{\mathrm{cell}}$ distribution is applied to the catalyst layers. For current driven mode one additional equation,

$$\tilde{i}_{\mathrm{cell}}(\tilde{t}) = \frac{1}{\tilde{L}} \int_0^{\tilde{L}} \tilde{i}(\tilde{x}_1, \tilde{t})\, \mathrm{d}\tilde{x}_1 \,, \tag{3.82}$$

is introduced to provide a closure for the current density distribution in the GDL inner slices. Here, the boundary condition is the cell current density $\tilde{i}_{\mathrm{cell}}$.

4
Numerical treatment

This section covers the numerical treatment of the presented PEMFC model and its implementation in Matlab®, [22]. In a first step towards the full multiphase model of the PEMFC, liquid water saturation is fixed at $s = 0$ in the entire domain. Due to the model formulation, the system of governing equations then is reduced automatically to a non-isothermal singlephase model, containing only one additional PDE for the conservation of energy, see appendix B. However, the temperature T appears as an additional intrinsic unknown and has to be accounted for in the electrochemical model, the equation of state and in the calculation of the PEM proton conductivity.

The procedure for spatial and temporal discretisation as well as linearisation in time of the governing nonlinear equations is adopted from the isothermal model and is summarised in the following for the sake of completeness. For details and the implicit coupling method between the GCs and GDLs the interested reader is referred to [1]. Furthermore, an imbalance check for the implemented conservation laws is presented.

4.1 Discretisation

4.1.1 Spatial domain

The spatial domains are treated with spectral methods. A continuous solution is sought in terms of Chebyshev polynomials of degree N, by determining the sought function values at the N computation nodes. Spectral methods show exponential convergence and thus, high accuracy with a comparatively small number of nodes. Gauss-Lobatto grid points,

$$x_i = \cos(i\pi/N)\,, \quad i = 0, \ldots, N \tag{4.1}$$

are used to discretise all domains of the model. The increased node densities at the boundaries avoid spurious oscillations caused by higher degree polynomials. To this end, also a spatial Gauss-Lobatto distribution of the inner slices in x_1-direction is chosen.

Spatial derivatives at discrete points x_i of a differentiable function $f(x)$, with $f(x_i) = f_i$, are found by multiplying the function with the differentiation matrix, e.g. for the first order derivative $D_{ij}^{(1)}$,

$$f_i' = \sum_j D_{ij}^{(1)} f_j\,. \tag{4.2}$$

The open source Matlab® package *chebfun* [23] is used to compute the entries of the analytically determinable dense differentiation matrices of different order.

According to the desired resolution depth, the number of computation nodes in the domains GC, GDL and PEM as well as the number of inner slices can be chosen independently, [1].

4.1.2 Time domain

The time derivative of a variable r at the current instance of time $(n+1)$ is approximated by a backward finite difference scheme of second order accuracy,

$$\left(\frac{\partial r}{\partial t}\right)^{(n+1)} = \frac{(1+2\alpha)r^{(n+1)} - (1-\alpha)^2 r^{(n)} + \alpha^2 r^{(n-1)}}{(1+\alpha)\Delta t^{(n+1)}} + \mathcal{O}\left(\Delta t^2\right), \tag{4.3}$$

which is capable of variable time stepping, whereat $\alpha = \Delta t^{(n+1)}/\Delta t^{(n)}$ represents the current time step ratio. The time step Δt within a range of $\Delta t_{\min} \dots \Delta t_{\max} \ll 1$ is adapted to the rate of change between of the current density and membrane water content, i.e. large time gradients of current density and membrane water content lead to decreasing time steps.

4.2 Linearisation in time (LIT)

As shown in section 3, a system of coupled nonlinear differential and algebraic equations has to be solved at each time step. To avoid numerically expensive Newton iterations, a linearisation of the governing equations with respect to the previous time step is applied. From Taylor series expansion one finds for a quadratic term rs at the current time step (n+1) the linear approximation

$$(rs)^{(n+1)} = r^{(n+1)}s^{(n)} + r^{(n)}s^{(n+1)} - r^{(n)}s^{(n)} + \mathcal{O}\left(\Delta t^2\right), \tag{4.4}$$

which operates at the same truncation error as the approximated time derivative in eq. (4.3). Applying eq. (4.4) consequently to all non-linear terms in the governing equations and coupling conditions finally yields a linear system of equations

$$\sum_j A_{ij}\, x_j = b_i \tag{4.5}$$

for the entire PEMFC model. This system has to be solved for each time step in an implicit manner, whereat the entries of A_{ij} and b_j have to be updated accordingly. The vector entries x_j represent the unknown variables from sections 3.2.1, 3.3.1, 3.4 and 3.5 at the corresponding grid points and the total unknown variable vector is built from the individual domain vectors,

$$\begin{aligned}\boldsymbol{x} = \big(&\boldsymbol{x}^{\mathrm{C}}_{\mathrm{GC}},\, \boldsymbol{x}^{\mathrm{A}}_{\mathrm{GC}},\, \boldsymbol{x}^{\mathrm{C}}_{\mathrm{GDL},1},\, \boldsymbol{x}_{\mathrm{PEM},1},\, \boldsymbol{x}^{\mathrm{A}}_{\mathrm{GDL},1},\, i_1,\, \boldsymbol{x}^{\mathrm{C}}_{\mathrm{GDL},2},\, \boldsymbol{x}_{\mathrm{PEM},2},\, \boldsymbol{x}^{\mathrm{A}}_{\mathrm{GDL},2},\, i_2,\, \dots,\\ &\boldsymbol{x}^{\mathrm{C}}_{\mathrm{GDL}n},\, \boldsymbol{x}_{\mathrm{PEM}n},\, \boldsymbol{x}^{\mathrm{A}}_{\mathrm{GDL}n},\, i_n\big)^T.\end{aligned} \tag{4.6}$$

For the additional temperature dependence due to the non-isothermal formulation, x_j of the isothermal model is extended and the entries for T are added below the ones of the already existing unknown variables u_1, p, ρ, ξ^{β}_{g}, $\xi^{\mathrm{N_2}}_{\mathrm{g}}$, $\xi^{\mathrm{H_2O}}_{\mathrm{g}}$, e.g. for the cathode GC:

$$\boldsymbol{x}^{\mathrm{C}}_{\mathrm{GC}} = \left(u_{1,1}, \dots, u_{1,n},\, \xi^{\beta}_{\mathrm{g}_{1,1}}, \dots, \xi^{\beta}_{\mathrm{g}_{1,n}}, \dots, \rho_{1,1}, \dots, \rho_{1,n},\, T_{1,1}, \dots, T_{1,n}\right). \tag{4.7}$$

The RHS vector b_j and the system matrix A_{ij} are extended to cover the non-isothermal model in a similar manner. The structure of the sparse system matrix A is plotted in fig. (6), where the single domains can be identified as bordered blocks along the principle diagonal. The coupling conditions between the domains are located at the minor diagonals. The dense submatrices represent the spatial derivatives from eq. (4.2).

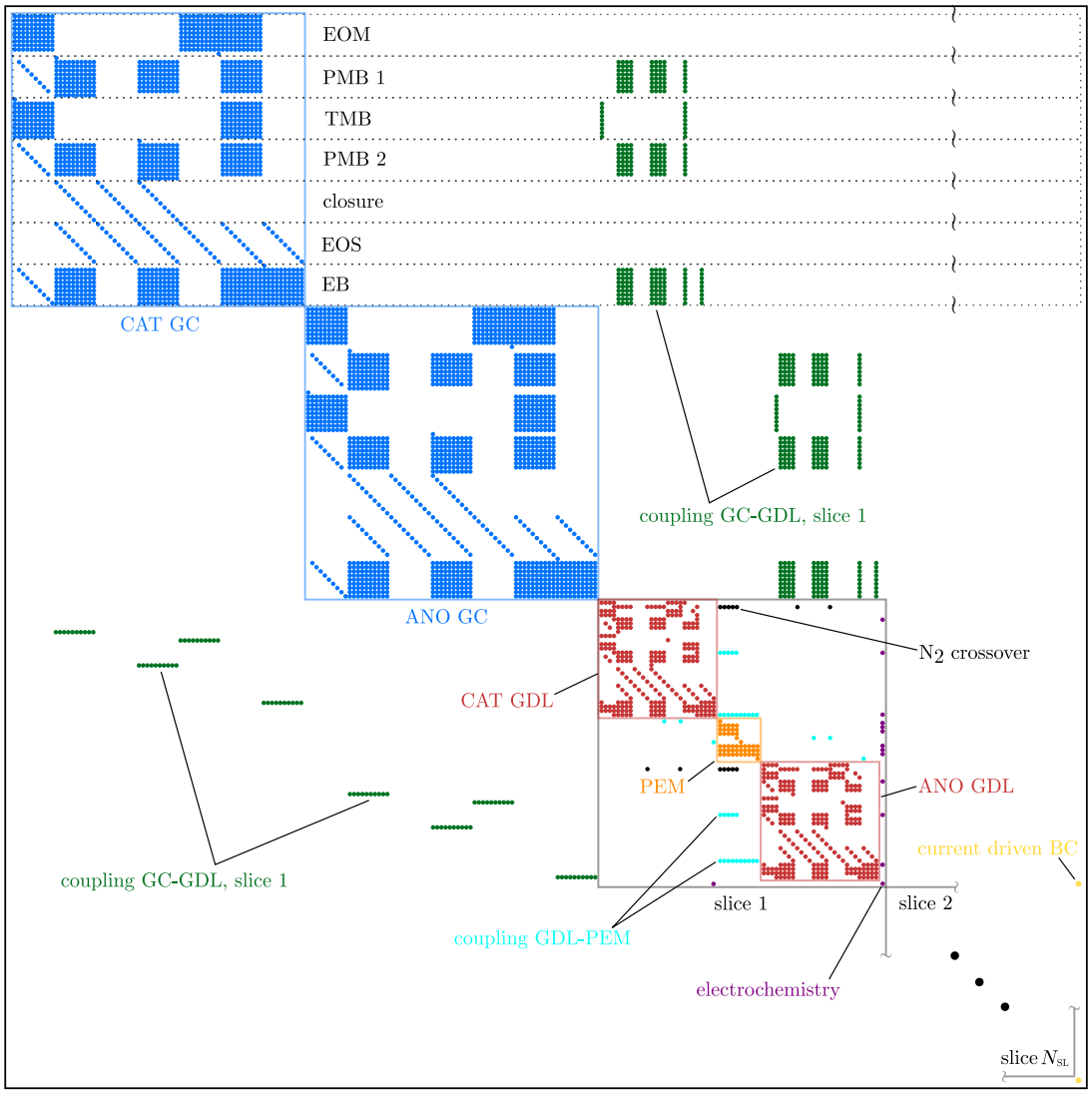

Figure 6: Structure of the sparse system matrix A for the non-isothermal singlephase PEMFC model as provided by the Matlab command `spy(A)`. Identification of the domains: cathode and anode GCs (blue) and inner slices containing GDLs (red), PEM (orange) and the equation for electrochemistry (purple). Coupling conditions: GC-GDL (green), GDL-PEM (cyan), N_2-crossover (black). For current driven mode one additional equation appears in the last row/column (yellow). The energy balance (EB) equations are added below the isothermal model equations from [1] in each domain. Identification of the other cathode GC equations: equation of motion (EOM), partial mass balance for species β (PMB 1) and H_2O (PMB 2), total mass balance (TMB), closure for species mass fractions and equation of state (EOS).

The dimension $N_A \times N_A$ of the new square matrix A, incorporating the non-isothermal model, is given by

$$N_A = N_\mathrm{u}\big(N_\mathrm{GC}^\mathrm{C} + N_\mathrm{GC}^\mathrm{A}\big) + N_\mathrm{SL}\big[N_\mathrm{u}\big(N_\mathrm{GDL}^\mathrm{C} + N_\mathrm{GDL}^\mathrm{A}\big) + 2\,N_\mathrm{PEM} + 1\big] + \delta_{i/u}\,, \tag{4.8}$$

where N_GC, N_GDL, N_PEM denote the number of computational nodes in the corresponding domains and $\delta_{i/u} = 0$ for voltage driven mode and $\delta_{i/u} = 1$ for current driven mode. The latter is due to the one additional equation for the cell current boundary condition, eq. (3.82), which operates in the last row/column of the system matrix A. The factor 2 accounts for the variables in the PEM: normalised water content λ and the newly added temperature T. N_SL and N_u denote the number of slices and the number of unknown variables for each grid point, respectively. In the non-isothermal model $N_\mathrm{u} = 7$. For the specific discretisation $N_\mathrm{GC}^\mathrm{C,A} = 10$, $N_\mathrm{GDL}^\mathrm{C,A} = 4$, $N_\mathrm{PEM} = 5$, $N_\mathrm{SL} = 5$, which is used for all the following simulations, the matrix A is of dimension $N_A \times N_A = 475^2$ with a sparsity of 0.9613 in the voltage driven mode. With the same discretisation, for comparison, the dimension of the system matrix of the isothermal model by [1] is $N_A \times N_A = 390^2$.

As in the isothermal model, values for material properties, e.g. the specific heat capacity of the gas mixture $\tilde{c}_{\mathrm{p_g}}$, are determined with respect to the previous time step to avoid additional nonlinearities in the governing equations. Small material property alterations with respect to time justify this simplification.

4.3 Conservation law imbalance check

The numerical deviation $\tilde{\Delta}$ from a general steady state conservation law for an arbitrary control volume $\tilde{CV}$, eq. (3.63), is calculated by

$$\tilde{\Delta} = \oint_{\partial\tilde{CV}} \left(\tilde{\theta}\tilde{\phi} - \tilde{\Sigma}\right) \mathrm{d}\tilde{S} - \tilde{\Gamma}\,, \tag{4.9}$$

where $\tilde{\Gamma}$ represents a general volumetric source term within the $\tilde{CV}$. To verify the simulations, the global imbalance is checked for each individual PEMFC domain as well as the total cell after each time step. This further allows to identify if a steady state is reached, as $\tilde{\Delta}$, which includes the time derivative $\partial_t(\tilde{\rho}\tilde{\phi})$ due to the steady state formulation of eq. (4.9), must approach zero.

Several simulations showed that a minimum number of $N_\mathrm{PEM} = 5$ computational nodes in the membrane is required to keep the energy equation imbalance at an acceptable level. For the discretisation mentioned in section 4.2 applied to the geometry of the 3D model by Cao et al. [24], imbalances $< 0.1\,\%$ relative to the incoming fluxes are achieved for all conservation laws. A larger number of grid points shows no significant decrease of the conservation law imbalance.

5
Results and discussion

The non-isothermal LIT model, implemented in Matlab® [22], is validated against steady-state 3D simulations performed by Cao et al. [24]. First, a benchmark polarisation curve is established to further investigate through-plane temperature distributions at different cell potentials. To validate the temporal thermal behaviour, steep changes in current density and inlet relative humidity are analysed and further compared with results by Wang et al. [25] and Wu et al. [26], respectively.

In contrast to the 3D model, the catalyst layers are not spatially resolved in the LIT model. Hence, they are added to the respective GDL domains and the assumption of an infinitely thin electrochemically active area at the GDL-PEM interface is maintained. All other geometrical dimensions are directly adopted from the 3D model. Fluid material properties such as binary diffusion coefficients, viscosity values or specific heats are related to the device temperature $\tilde{T} = 343.15\,\mathrm{K}$ from [1], as the deviation to the operating condition $\tilde{T} = 353.15\,\mathrm{K}$ is negligible. The gas inlet velocity is given by

$$\tilde{u}^{i}_{1,\mathrm{in}} = \iota_i \frac{\tilde{i}_r}{n_i \tilde{F}} \frac{\tilde{W}_{\mathrm{GDL}}}{\tilde{W}_{\mathrm{GC}}} \frac{\tilde{\mathcal{R}} \tilde{T}_{\mathrm{in}}}{\tilde{p}_{\mathrm{amb}}} \frac{1}{\xi_{\mathrm{g}}^{\beta}}\,, \tag{5.1}$$

where the stoichiometric factor $\iota_i = 3$ and the inlet relative humidity (RH) is set to 60 % on both sides. Co-flow mode is used for all the following simulations and no N_2 is fed to the FC. The applied boundary conditions are summarised in table 3, PEMFC geometry and material data used for all simulations is shown in table 5.

Parameter [unit]	Symbol	Value
Inlet temperature [K]	$\tilde{T}_{\mathrm{in}}$	353.15
Bipolar plates temperature [K]	$\tilde{T}_{\mathrm{BP}}$	353.15
Inlet gas mass fraction [−]		
O_2 cathode	$\xi_{\mathrm{g}}^{\mathrm{O_2}}$	0.1819
H_2O cathode	$\xi_{\mathrm{g}}^{\mathrm{H_2O}}$	0.8181
H_2 anode	$\xi_{\mathrm{g}}^{\mathrm{H_2}}$	0.2208
H_2O anode	$\xi_{\mathrm{g}}^{\mathrm{H_2O}}$	0.7792
Inlet relative humidity CAT/ANO [%]	RH	60/60
Stoichiometric factor CAT/ANO [−]	ι	3/3
Outlet pressure [Pa]		
Cathode	$\tilde{p}_{\mathrm{amb}}$	101 325
Anode	$\tilde{p}_{\mathrm{amb}}$	101 325

Table 3: PEMFC boundary conditions for the steady state validation against the 3D model by Cao et al. [24].

Since the exact values are not listed in the Cao publication [24], half-cell reaction entropies for the gaseous water product are calculated following the approach by Lampinen and Fomino [27], with the consequence that the anode half-cell reaction is endothermic, $\Delta_{\text{reac}}\tilde{S}^{\text{A}} = 399.2\,\text{kJ}\,\text{mol}^{-1}\,\text{K}^{-1}$ and the cathode half-cell reaction is exothermic, $\Delta_{\text{reac}}\tilde{S}^{\text{C}} = -442.4\,\text{kJ}\,\text{mol}^{-1}\,\text{K}^{-1}$. The reference polarisation curve and temperature profiles are obtained from the paper using the online tool *WebPlotDigitizer* [28].

5.1 Steady-state validation

To evaluate the LIT models' predictive capabilities by means of temperature distributions, a benchmark polarisation curve is established by altering the cell current density from 100 to 12 500 $\text{A}\,\text{m}^{-2}$. Two fitting parameters, the reference exchange current density $\tilde{i}_{0,r}$, eq. (3.62), and the second membrane conductivity fitting parameter $f_{\text{PEM},2}$, eq. (3.59), are manually modified to adjust the polarisation curve obtained by the LIT model to the results by Cao et al. A bigger reference exchange current density moves the polarisation curve towards a bigger cell potential, whereas a decrease of the second membrane conductivity fitting parameter rotates the curve in clockwise direction. Here, good agreement between the fitted LIT model (black) and the 3D model curve (magenta) is found for $\tilde{i}_{0,r} = 1 \times 10^{-3}\,\text{A}\,\text{m}^{-2}$ and $f_{\text{PEM},2} = 0.45$, see fig. 7. The unfitted LIT model results with $\tilde{i}_{0,r} = 0.2 \times 10^{-3}\,\text{A}\,\text{m}^{-2}$ from [1] are plotted in blue. For the parameters of the electrochemical model see table 5. Minor deviations of the polarisation curves are partly based on different models for the electrochemical reaction.

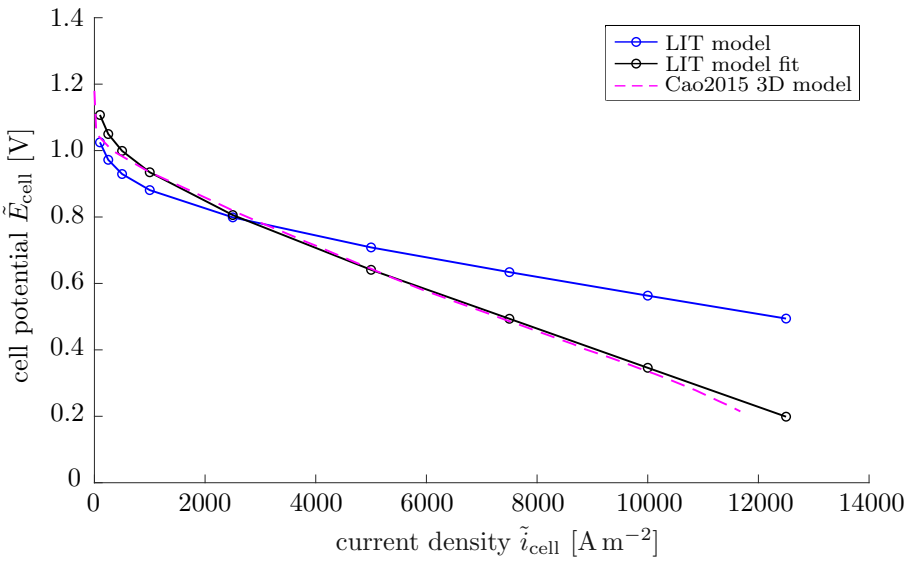

Figure 7: Polarisation curves of the unfitted (blue) and fitted (black) LIT model compared to the reference simulation (magenta) by Cao et al. [24]

Steady-state through-plane temperature distributions for the middle of the PEMFC (in x_1-direction) are then computed for two values of the thermal contact resistance (TCR) between the GDL and BP, $\tilde{R}_{\text{c}} = 0$ and $\tilde{R}_{\text{c}} = 9.375 \times 10^{-4}\,\text{m}^2\,\text{K}\,\text{W}$. Both fitting parameters are kept unchanged,

while the three different cell potentials $\tilde{E}_{\text{cell}} = 0.4, 0.6$ and $0.8\,\text{V}$ are applied as the boundary condition in voltage driven operation. The predicted temperature distributions for the case of no TCR are given in fig. 8a, the case of finite TCR is shown in fig. 8b: Dashed coloured lines represent the reference results for different cell potentials from Cao et al. [24], located at the BP-GC interface in x_3-direction. Respective solid lines show the LIT model results for the MEA (with markers) and the GC (no markers). The uniform LIT model BP boundary condition temperature is plotted in black. The vertical dotted black lines represent the domain interfaces, the aforementioned catalyst layer is indicated on both sides of the PEM.

The temperature maximum is found to be located in the cathode catalyst layer, where most of the heat is generated due to the exothermic half-cell reaction and activation losses. Predicted values for the temperatures in the MEA however, are much smaller in the LIT model compared to the 3D simulations for both TCR cases. This is partly because the bipolar plate and gas channel boundary conditions are applied differently in the two models: The LIT model assumes a uniform temperature distribution in both domains, the Cao model on the contrary, explicitly resolves the BP and GC temperature fields in x_2-direction, with the temperature boundary condition applied to the most outside layer of the domains. Furthermore, the outside GDL interface and the GC temperature is increasingly constrained to the BP temperature for $\tilde{R}_{\text{c}} \to 0$, as a consequence of the BP-GDL heat flux term in the LIT models' energy balance coupling condition in eq. (3.68). The discontinuity of the temperature due to a finite TCR at the BP-GDL interface becomes apparent in fig. 8b. However, the temperature offset relative to the boundary condition at the BP-GC-GDL interface is not matched.

In the case of no TCR, the anode GDL temperature gradient for $\tilde{E}_{\text{cell}} = 0.4\,\text{V}$ also appears to be predicted smaller in the LIT model, and is even directed in the opposite direction for the two bigger cell potential boundary conditions. Here, it comes into play, that for low current densities (big cell potentials) the Joule heating effect in the membrane is outweighed by the heat absorbed from the endothermic anode reaction, resulting in a heat sink and temperature drop below the bipolar plate temperature. On the contrary, the temperature gradients in the cathode GDL and in the PEM are in good agreement. In the case of finite TCR, simulated temperature gradients match the averaged gradients of the Cao model fairly accurately. However, the kink in GDL temperature distributions is not predicted by the LIT model, which yields an almost linear function. As the gradients in the MEA are similar in both models, the maximum temperature differences in the respective domains are also alike. Hence, if one assumes the LIT temperature profile in the MEA to start at the cathode BP/GC-GDL interface temperature calculated by the Cao model, a fairly similar result to the 3D simulation is obtained.

It should further be pointed out that the through-plane temperature distributions obtained by the present quasi-2D LIT model represent a temperature average in x_3-direction. Cao et al. showed in a prior work, [29], that MEA temperatures can be significantly lower under the BP plate than they are under the GC. This effect strongly depends on the anisotropy of the GDL. Greater anisotropy in terms of the GDLs thermal conductivity, meaning higher values for the in-plane direction, results in a more uniform temperature distribution in x_3-direction. However, the temperature profile obtained by Cao et al. is positioned at the BP-GC boundary and reflects the mean temperature in this direction well enough to determine that the LIT model results are too small.

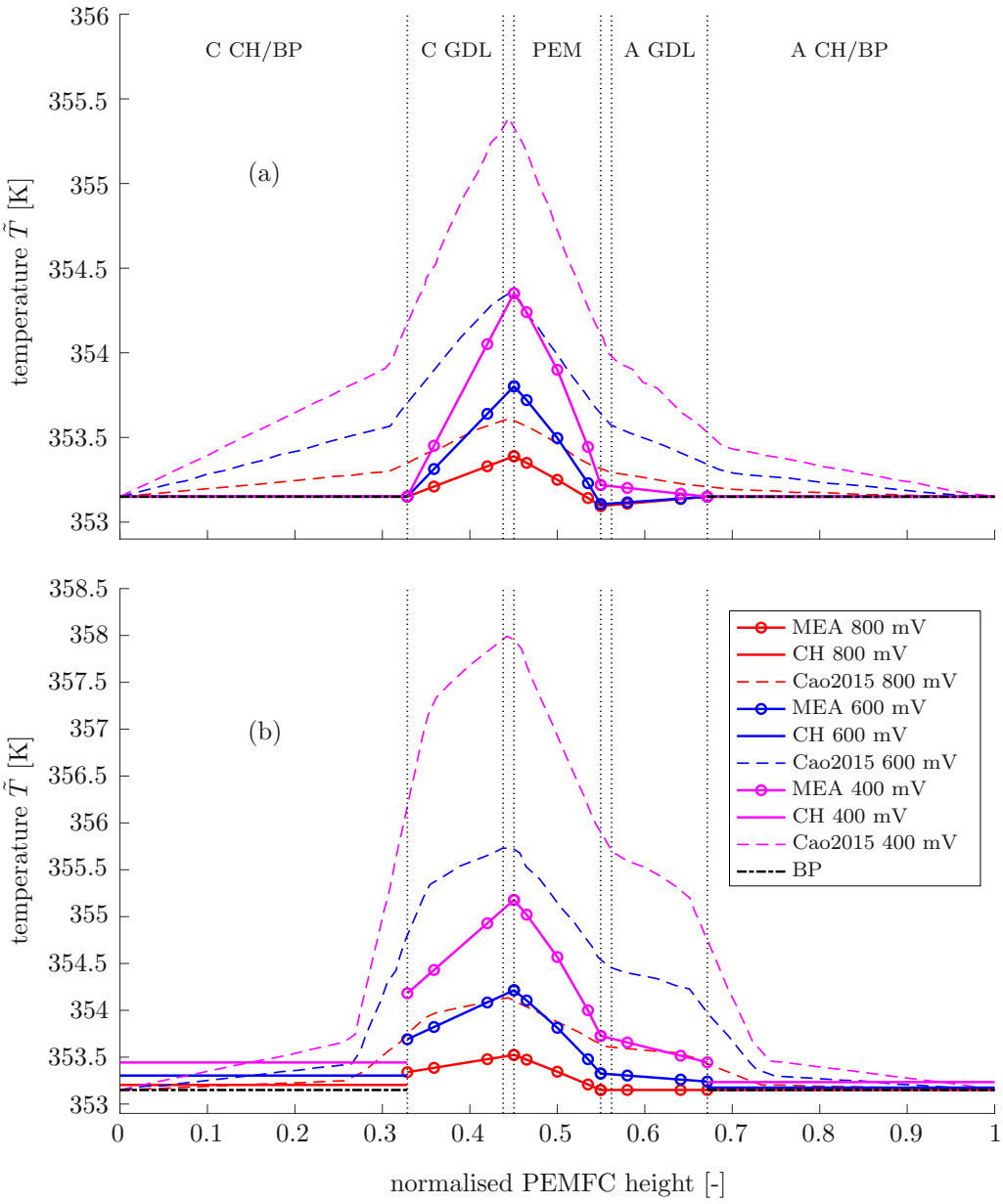

Figure 8: Through-plane temperature distributions, located in the middle of the x_1-direction, for different cell potentials: 0.8 V (red), 0.6 V (blue) and 0.4 V (magenta), simulated with the LIT model and the 3D model by Cao et al. [24] for comparison: (a) $\tilde{R}_c = 0$ and (b) $\tilde{R}_c = 9.375 \times 10^{-5}\,\mathrm{m^2\,K\,W}$.

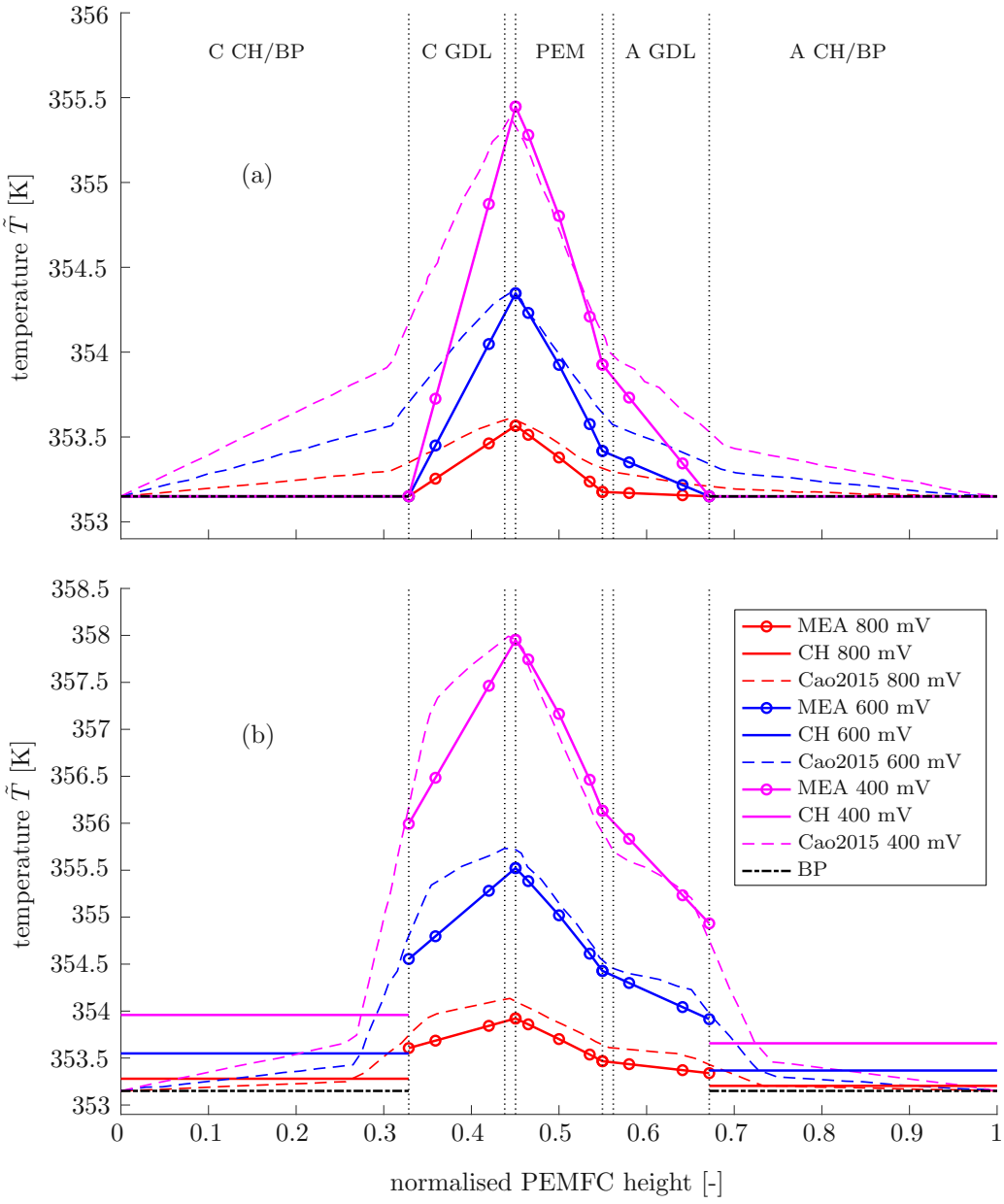

Figure 9: Through-plane temperature distributions, located in the middle of the x_1-direction, for different cell potentials: 0.8 V (red), 0.6 V (blue) and 0.4 V (magenta), simulated with the thermally fitted LIT model ($f_\mathrm{k} = 0.4$, $f_\mathrm{TCR} = 4$) and the 3D model by Cao et al. [24] for comparison: (a) $\tilde{R}_\mathrm{c} = 0$ and (b) $\tilde{R}_\mathrm{c} = 9.375 \times 10^{-5}\,\mathrm{m^2\,K\,W}$.

To achieve better predictive capabilities of the LIT model in terms of thermal PEMFC behaviour, the temperature distribution in the bipolar plates and gas channels as well as their influence on the MEA has to be accounted for parametrically. Therefore, two fitting factors for the TCR $\tilde{R}_\mathrm{c}$ and the GDL thermal conductivity $\tilde{k}_\mathrm{GDL}$ are introduced, such that

$$\tilde{R}_\mathrm{c}^* = f_\mathrm{TCR}\tilde{R}_\mathrm{c} \quad \text{and} \quad \tilde{k}_\mathrm{GDL}^* = f_\mathrm{k}\tilde{k}_\mathrm{GDL}\,. \tag{5.2}$$

They allow to match the 3D model more accurately without resolving an additional BP domain or the x_2-direction in the GC. For the case of no TCR, $\tilde{k}_\mathrm{GDL}$ is set to 40 % of the reference value by Cao et al. In the second case, the additional fitting factor $f_\mathrm{TCR} = 4$ is multiplied to the thermal contact resistance. The results of the thermally fitted LIT model are shown in fig. 9a for the no-TCR-reference case and in fig. 9b for the $\tilde{R}_\mathrm{c} = 9.375 \times 10^{-5}\,\mathrm{m^2\,K\,W}$ reference case.

The temperature maximums in the cathode catalyst layer predicted by the thermally fitted LIT model are in good agreement with the 3D simulations for both the no-TCR and the finite-TCR case. For the latter, also the BP-GC-GDL interface temperatures are matched closely, meaning that the TCR fitting parameter allows to simulate the temperature difference in the BPs and GCs. In the no TCR case this is not possible and as discussed earlier, the outer GDL temperatures are constrained to the BP temperature as a consequence of the boundary condition in eq. (3.68). As the LIT model predicts the same maximum temperature difference within the MEA as the 3D Cao model does for the whole BP-MEA assembly, steeper temperature gradients are obtained.

5.2 Dynamic simulation

To demonstrate the dynamic simulation capabilities of the non-isothermal LIT model, the thermal response to prescribed steep time gradients of the cell potential, current density and inlet relative humidity is presented in the following.

First, the dynamic change of the through plane temperature in the middle of the PEMFC in reaction to a 1 s long, smooth cell potential drop from 0.8 to 0.4 V is discussed: As depicted in fig. 10, the current density strongly increases after the step is applied at $\tilde{t} = 2\,\mathrm{s}$, rapidly generating more heat due to the electrochemical reaction in the catalyst layers and the Joule heating effect in the PEM. The increasing amount of heat is temporarily accumulated in the region around the cathode catalyst layer, as the heat (and mass) transport properties of the GDL and PEM are not sufficient enough for their immediate removal. The consequence is a temperature overshoot at $\tilde{t} = 5.372\,\mathrm{s}$, where the cathode CL reaches its maximum temperature of $\tilde{T} = 358.21\,\mathrm{K}$ before it slowly cools down to approach a steady state. The temperature remains constant at $\tilde{T} = 357.90\,\mathrm{K}$ approximately 10 s after the voltage drop was completed.

In this context, the extremely low computational cost of a LIT model simulation should be highlighted: For the 30 s time frame of the example above, the results are obtained within a computation time of 3 min where variable time stepping in the range $\Delta\tilde{t} = 0.001 \ldots 0.035\,\mathrm{s}$ is used. In total, 1860 time steps were applied, that is roughly 0.1 s/step. The computer platform used for all the presented simulations is a Dell XPS 13 notebook (Intel® Core™ i5-5200U 2.20 GHz CPU, 8 GB RAM). Although this system is not optimal for such simulations, the linearisation scheme applied for the governing equations, in combination with the use of spectral methods and adaptive time stepping, allows to investigate transient PEMFC phenomena with very low computational resources. The isothermal LIT model by Murschenhofer et al. [1] even achieved real-time capability. For comparison, Cao et al. [24] report a computation time of more than 5 h to simulate the

steady-state temperature profile on a $38 \times 16 \times 40$ grid, using a 3 GHz Dual Core CPU and 8 GB RAM system.

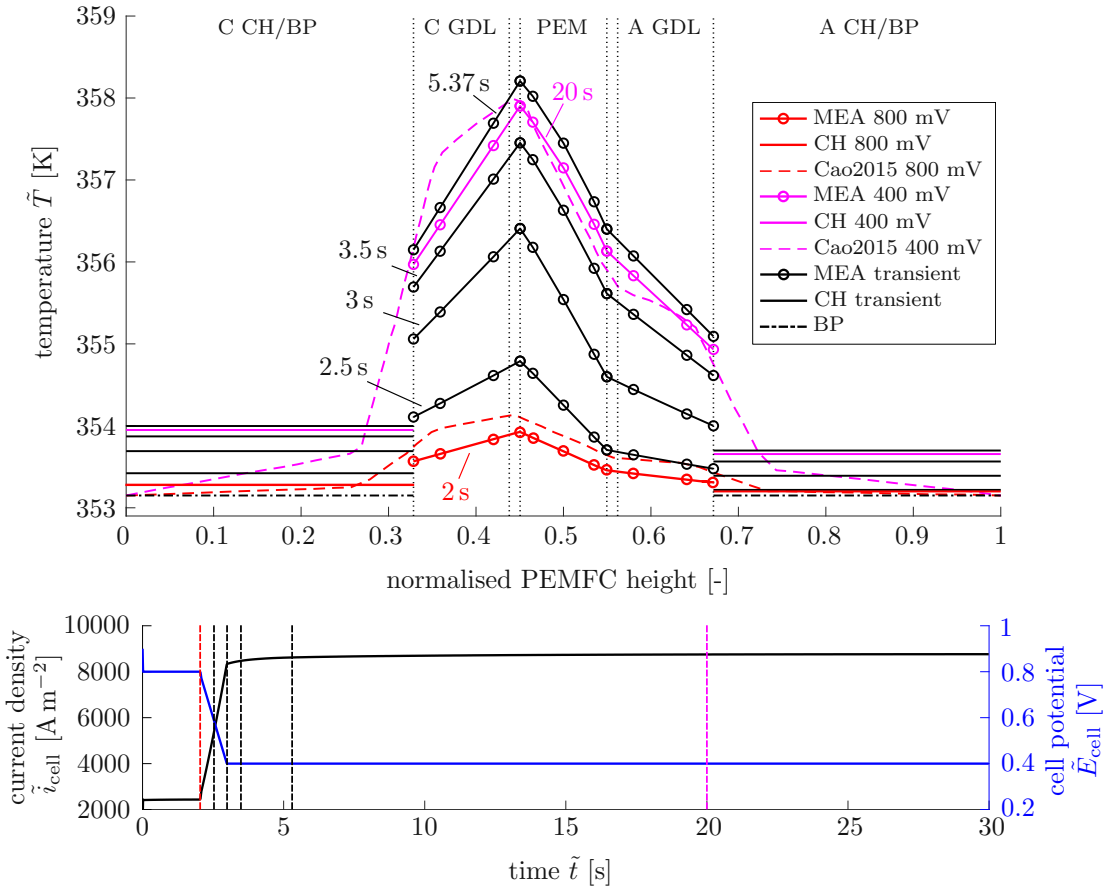

Figure 10: Dynamic change of the through-plane temperature distribution due to a cell potential drop from 0.8 (red) to 0.4 V (magenta), simulated with the thermally fitted LIT model ($f_{\mathrm{k}} = 0.4$, $f_{\mathrm{TCR}} = 4$). Dashed lines show the steady-state results by Cao et al. [24]. Black solid lines represent the MEA (with markers) and CH temperature distribution at different instances of time as indicated by dashed lines in the temporal evolution of the current density $\tilde{i}_{\mathrm{cell}}$ and cell potential $\tilde{E}_{\mathrm{cell}}$ plotted below.

The effect of overshooting temperature behaviour after a load change, as seen in fig. 10, was also observed in a very recent work by Wang et al. [25]. They used a multiphase 2D model with 4764 computational nodes to investigate transient temperature response to a large step in current density. LIT model simulations for the same current density changes are conducted for comparison, keeping all the other boundary conditions unchanged, see table 3. Starting from a steady state at 100 A m^{-2}, 1 s long steps to 6000, 10 000, 14 000, 18 000 and 20 000 A m^{-2} are applied at $\tilde{t} = 2$ s. The response of the average cathode catalyst layer temperature is shown in fig. 11.

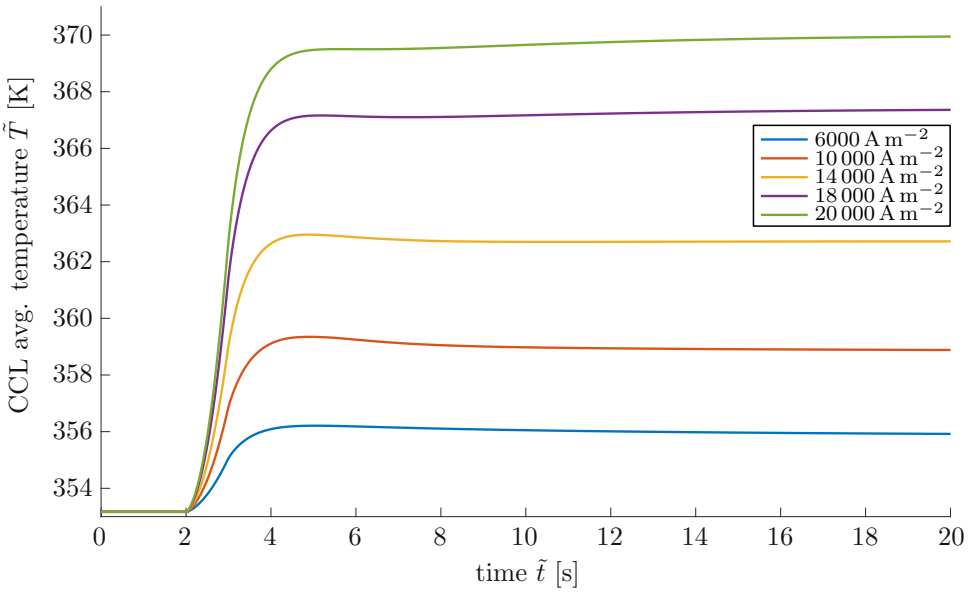

Figure 11: CCL average temperature responses to a 1 s long current density change at $\tilde{t} = 2\,\mathrm{s}$ from 100 to 6000, 10 000, 14 000, 18 000 and 20 000 A m^{-2} according to the LIT model.

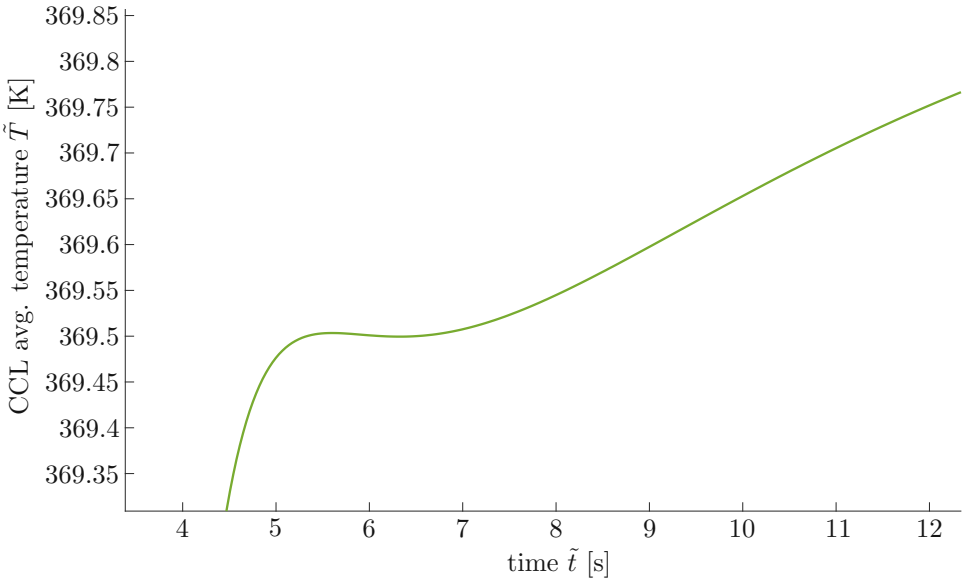

Figure 12: Zoom on the CCL average temperature response to a 1 s long current density change at $\tilde{t} = 2\,\mathrm{s}$ from 100 to 20 000 A m^{-2} according to the LIT model.

Here again, good qualitative agreement is found for the overall temporal behaviour of the cathode catalyst layer temperature. In both models a steady state is reached approximately 10 to 20 s after the step is applied. The predicted times from the LIT model simulations for the temperature to reach steady-state conditions are shown in table 4. Very similar transient behaviour is predicted by the LIT model for the cases 6000, 10 000 and 14 000 A m^{-2}, where a temperature overshoot appears after the current step is completed. In contrast to Wang et al. for the two largest current density steps, the CCL is exposed to a small temperature undershoot after a local temperature maximum is reached and before the temperature rises again to finally approach steady state, see fig. 12. The course of temperature is closely related to water transport in the PEM: Due to the electro-osmotic drag, water is accumulated at the cathode PEM interface. After the step is completed, water slowly diffuses back to the anode until the water content increases again.

To quantify the transient behaviour, the dimensionless temperature overshoot, [25],

$$\overline{\Delta T} = \frac{\tilde{T}_{\max} - \tilde{T}_{\text{steady}}}{\tilde{T}_{\text{steady}}} \tag{5.3}$$

is introduced. The corresponding values predicted by the LIT and Wang et al. model are listed in table 4. Similar to the multiphase model, the magnitude of the temperature overshoot also first increases with growing current step size to then decrease for the cases above 10 000 A m^{-2}. The temperature undershoot however, is only indicated for step sizes greater than 20 000 A m^{-2} in the work by Wang et al. This supposedly is due to the values for the dimensionless temperature overshoots that were generally predicted to be larger (about 8 times as much compared to the LIT model). Wang et al. argue that the instant rise of phase change latent heat between gaseous and membrane water is the main cause for the temperature overshoot, which is an effect that is not captured in the current LIT model. Varying overshoot magnitudes are also partly due to different material properties and relative humidity boundary conditions.

Step from 100 to [A m^{-2}]	6000	10 000	14 000	18 000	20 000
Time to steady state (LIT model) [s]	16.69	13.54	9.18	18.61	20.75
$\overline{\Delta T}$ (LIT model) [%]	0.10	0.14	0.06	−0.08	−0.14
$\overline{\Delta T}$ (Wang et al. [25]) [%]	0.80	1.10	0.95	0.43	0.13

Table 4: Time for the CCL temperature to reach steady state and dimensionless temperature overshoot values for current step sizes of different magnitude.

A third example of dynamic PEMFC operation is the rapid change of the relative humidity (RH) boundary condition. Wu et al. [26] report from 3D multiphase flow simulations that abrupt dehydration of the inlet gases causes a severe temperature drop in the first parts of the cell. The temperature even undercuts the BP boundary condition temporarily before a new steady state of the temperature field and current density is reached. Such a behaviour is also found in LIT model simulations, where the RH at the cathode and anode inlets is dropped from 60 to 20 % within 1 s. The cell potential is fixed at 0.4 V. To better illustrate the sub-cooling phenomenon, the GC length is extended to $\tilde{L} = 200$ mm, all other boundary conditions remain unchanged, see table 3. The temporal evolution of the temperature field in the green symmetry plane (fig. 2) is depicted in fig. 13, in which the gas channel inlets are located on the left.

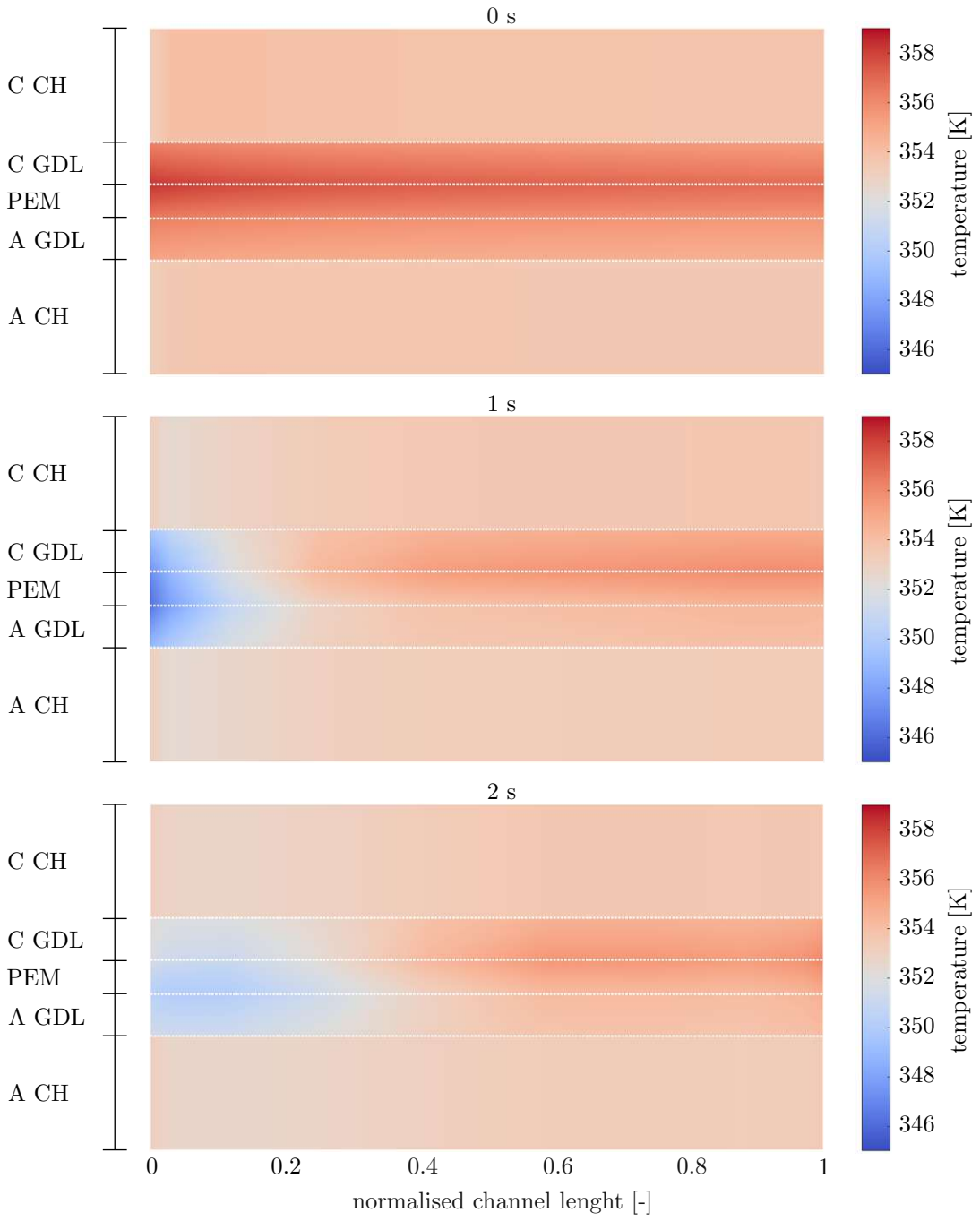

Figure 13: PEMFC temperature response to a 1 s long change of the inlet relative humidity at $\tilde{t} = 0\,\mathrm{s}$ from 60 to 20 % on the cathode and anode side according to the LIT model.

At $\tilde{t} = 0\,\mathrm{s}$ the smooth step is applied to the inlet RH. The temperature drops drastically within the first second, at $\tilde{t} = 0.941\,\mathrm{s}$ the minimum value of $\tilde{T} = 346.82\,\mathrm{K}$ is observed in the CCL. The cold spot then diffuses in the channel direction x_1 such that about one third of the MEA is cooled below the BP temperature at $\tilde{t} = 2\,\mathrm{s}$. Wu et al. [26] argue that the cooling effect is due to the sudden increase in evaporation of liquid water, which is in contradiction with the (single phase) LIT model results. It therefore seems as if also other dynamic processes affect the cooling behaviour during and after inlet gas dehydration. One of which is the dehydration of the membrane itself, as accumulated membrane water (and its enthalpy) is rapidly released into the adjacent gas diffusion layers to be transported further away. In the first seconds after the RH starts to change, the corresponding enthalpy fluxes outweigh the heat released by the electrochemical reaction and Joule effect. Only after some time this is inverted and the cell heats up again to approach steady-state conditions at approximately $\tilde{t} = 50\,\mathrm{s}$. Here, the temporal behaviour of the PEMFC temperature and current density is in good qualitative agreement with the results by Wu et al. [26]. However, exact quantitative comparison, e.g. of the temperature drop, is difficult, as various parameters have influence on the thermal response to a dehydration event. The Wu multiphase model neglects the TCR at the BP-GDL interface and therefore in general predicts smaller MEA temperatures, comparable with fig. 9. LIT model simulations show that the temperature drop relative to the temperature at the beginning is also decreased for smaller TCRs. Nonetheless, for vanishing TCR the LIT model still predicts greater thermal perturbation after a steep change in RH. Aside from varying material properties or boundary conditions, a reason for that might be the assumption of equilibrium between GDL and membrane water. Here, Wu et al. use a finite-rate transfer model that limits mass and enthalpy fluxes at the GDL-PEM interfaces.

Parameter [unit], source	Symbol	Value
PEMFC length [m], [24]	$\tilde{L}$	0.05, 0.20
Anode & cathode GC		
Height [m], [24]	$\tilde{H}_{\mathrm{GC}}$	1.00×10^{-3}
Width [m], [24]	$\tilde{H}_{\mathrm{WC}}$	762×10^{-6}
Conv. heat transfer coefficient [$\mathrm{W\,m^{-2}\,K^{-1}}$], [24]	$\tilde{\alpha}$	1000
Anode & cathode GDL		
Height [m], [24]	$\tilde{H}_{\mathrm{GC}}$	272.7×10^{-6}
Width [m], [24]	$\tilde{H}_{\mathrm{GC}}$	2.00×10^{-3}
Porosity [-], [24]	ε	0.6
Bruggemann exponent [-], [1]	q	1.5
Hydraulic permeability [$\mathrm{m^2}$], [1]	$\tilde{\kappa}$	10.7×10^{-15}
Thermal conductivity [$\mathrm{W\,m^{-1}\,K^{-1}}$], [24]	$\tilde{k}_{\mathrm{GDL}}$	$4.33 f_{\mathrm{k}}$
Thermal contact resistance (TCR) [$\mathrm{m^2\,K\,W^{-1}}$], [24]	$\tilde{R}_{\mathrm{c}}$	$0,\ 98.75 \times 10^{-6} f_{\mathrm{TCR}}$
Thermal fitting parameter [-]	$f_{\mathrm{k}};\ f_{\mathrm{TCR}}$	0.4; 4
Anode & cathode CL		
Thickness [m], [24]	$\tilde{H}_{\mathrm{CL}}$	28.7×10^{-6}
Electrode roughness [-], [1]	$\tilde{a}_{\mathrm{C}}\tilde{L}_{\mathrm{C}}$	500
Activation energy for $\mathrm{O_2}$ reduction on Pt [$\mathrm{J\,mol^{-1}}$], [1]	$\tilde{E}_{\mathrm{act}}$	66×10^{3}
Reference exchange current density [$\mathrm{A\,m^{-2}}$]	$\tilde{i}_{0,r}$	1×10^{-3}
Open circuit potential [V], [1]	$\tilde{E}_{\mathrm{OC}}$	1.192
Reference $\mathrm{O_2}$ partial pressure [Pa], [1]	$\tilde{p}_{\mathrm{O_2},r}$	101250
Reference temperature for $\tilde{i}_0$ [K], [1]	$\tilde{T}_{0,r}$	298.15
Pressure dependency coefficient [-], [1]	γ_{C}	1
Membrane		
Thickness [m], [24]	$\tilde{H}_{\mathrm{PEM}}$	230×10^{-6}
Density [$\mathrm{kg\,m^{-3}}$], [1]	$\tilde{\rho}_{\mathrm{PEM}}$	2024.7
Equivalent weight [$\mathrm{kg\,mol^{-1}}$], [1]	$\tilde{\mathrm{EW}}$	1.1
$\mathrm{N_2}$ permeance at $\tilde{T} = 343.15\,\mathrm{K}$ [$10^9 \mathrm{mol\,s^{-1}\,m^{-1}\,Pa^{-1}}$], [1]	$\tilde{k}_{\mathrm{N_2}}$	$251.7 + 37.3\lambda$
Water diffusion coefficient at $\tilde{T} = 343.15\,\mathrm{K}$ [$10^9 \mathrm{m^2\,s^{-1}}$], [1]	$\tilde{\mathcal{D}}_{\mathrm{w}}$	$89.227\lambda \times 10^{-12}$
Electro-osmotic drag coefficient at $\tilde{T} = 343.15\,\mathrm{K}$ [-], [1]	$\tilde{C}_{\mathrm{drag}}$	0.1578λ
Ionic conductivity fitting parameter [-]	$f_{\mathrm{PEM1}};\ f_{\mathrm{PEM2}}$	1; 0.45
Thermal conductivity [$\mathrm{W\,m^{-1}\,K^{-1}}$], [24]	$\tilde{k}_{\mathrm{PEM}}$	0.95

Table 5: Geometrical dimensions and material properties of the PEMFC used in the simulations.

6
Conclusion and outlook

A dynamical multiphase flow PEMFC model, described by non-linear equations within a quasi-2D approach, is proposed in this work. The case of non-isothermal single phase flow is further implemented to extend the model by Murschenhofer et al. [1].

Starting from a general set of balance equations for multiphase flow, the computationally more efficient multiphase mixture equations are derived. For the gas channel domains, homogeneous flow is assumed. Within the gas-diffusion-layers capillary effects are considered, following the theoretical work by Wang and Cheng [8] on multiphase, multicomponent transport in capillary porous media. Furthermore, the additional energy balance equation for the proton exchange membrane is derived.

The non-dimensional governing equations are then found from the previously derived 3D integral conservation laws by applying the quasi-2D approach presented in [1]. This approach allows to capture the heat and mass fluxes outside of the considered 2D plane. Coupling conditions between two adjacent domains are rigorously derived from Kotchine's theorem. A dimensional analysis further specifies the relative impact of the different transport mechanisms within the PEMFC. Calculations showed that gas diffusion must be accounted for in both the gas channels and porous layers. The associated enthalpy flux has to be considered as well.

In a first step towards multiphase simulations, the non-isothermal single phase case of the presented model is further implemented in Matlab®. A Chebyshev collocation method, providing high accuracy with few computation nodes, is used for the discretisation of the spatial domains. Time derivatives are approximated by a backward finite difference scheme of second order accuracy, which is capable of adaptive time stepping. Moreover, a linearisation scheme for the nonlinear governing equations is introduced, which avoids numerically expensive Newton iterations at each time step and hence assures fast computation, [1].

The extended quasi-2D linearised in time (LIT) model is validated in detail against various higher resolving multiphase simulations. The adaption of fitting parameters allows to accurately reproduce the polarisation curve of the experimentally validated 3D PEMFC model by Cao et al. [24]. Steady state temperature distributions at different cell potentials are further used for reference. For identical material parameters the LIT model yields lower temperatures in the membrane electrode assembly, due to neglected through-plane heat fluxes in the bipolar plates and gas channels. However, the implementation of additional fitting parameters for the GDLs' thermal conductivity and thermal contact resistance of the BP-GDL interface matches the 3D model results. The steady state temperature values and gradients inside the membrane-electrode-assembly agree very well at different cell potentials. In dynamical simulations, the LIT model is further able to capture effects such as catalyst layer temperature transients due to a steep increase in current density, as reported by Wang et al. [25], and PEMFC subcooling after an abrupt dehydration of the inlet gases as reported by Wu et al. [26]. The results for all the performed simulations were obtained within minutes of simulation time, even though the used computer platform is a Dell XPS 13 notebook (Intel® Core™ i5-5200U 2.20 GHz CPU, 8 GB RAM). The LIT model therefore is especially suited for widespread dynamical parameter studies and control unit adjustments. Real-time capability as in the isothermal model [1] could further be achieved with a more powerful computer platform.

For future investigations, several improvements are conceivable. The full numerical implementation of the presented governing equations for multiphase flow poses the most significant leap forward in the predictive capabilities of the LIT PEMFC model. Here, a convenient treatment for the step-like definition of the liquid water saturation function, eq. (3.12), has to be found. Two approaches are possible: Firstly, to evaluate all liquid phase related equations fully explicitly after each time step, or secondly, to develop an appropriate model to calculate the mass exchange rate between the liquid and gas phase. The latter would allow to solve the full set of governing equations in an implicit way. Further improvements, also applicable to the single phase case, include the adaption of a finite-rate transfer model for the GDL-PEM interfaces, e.g. as presented in [26], and to consider the BPs' and GCs' through-plane heat fluxes in the governing equations.

References

[1] D. Murschenhofer, D. Kuzdas, S. Braun, and S. Jakubek. A real-time capable quasi-2D proton exchange membrane fuel cell model. *Energy Conversion and Management* **162** (2018), pp. 159–175.

[2] K. Jiao and X. Li. Water transport in polymer electrolyte membrane fuel cells. *Progress in Energy and Combustion Science* **37** (2011), pp. 221–291.

[3] F. Barbir. *PEM Fuel Cells*. Second Edition. Academic Press, Boston (2013).

[4] J. Ramousse, O. Lottin, S. Didierjean, and D. Maillet. Heat sources in proton exchange membrane (PEM) fuel cells. *Journal of Power Sources* **192** (2009), pp. 435–441.

[5] T. Springer, T. Zawodzinski, and S. Gottesfeld. Polymer electrolyte fuel cell model. *Journal of The Electrochemical Society* **138** (1991), pp. 2334–2342.

[6] P. Stephan et al. *VDI-Wärmeatlas*. Springer, Berlin/Heidelberg (2019).

[7] C. E. Brennen. *Fundamentals of Multiphase Flow*. Cambridge University Press (2005).

[8] C. Wang and P. Cheng. A multiphase mixture model for multiphase, multicomponent transport in capillary porous media—I. Model development. *International Journal of Heat and Mass Transfer* **39** (1996), pp. 3607–3618.

[9] A. Cook. Enthalpy diffusion in multicomponent flows. *Physics of Fluids* **21** (2009).

[10] C. Wang and P. Cheng. Multiphase Flow and Heat Transfer in Porous Media. *Advances in Heat Transfer* **30** (1997), pp. 93–182.

[11] J. Spurk and N. Aksel. *Strömungslehre. Einführung in die Theorie der Strömungen*. Springer, Berlin/Heidelberg (2019).

[12] R. Shah and A. London. *Laminar Flow Forced Convection in Ducts. A Source Book for Compact Heat Exchanger Analytical Data*. Advances in Geophysics. Academic Press (1978).

[13] E. L. Cussler. *Diffusion: Mass Transfer in Fluid Systems*. 3rd ed. Cambridge University Press (2009).

[14] Y. Wang and C.-Y. Wang. A Nonisothermal, Two-Phase Model for Polymer Electrolyte Fuel Cells. *Journal of The Electrochemical Society* **153** (2006).

[15] Z. Wang, C. Wang, and K. Chen. Two-phase flow and transport in the air cathode of proton exchange membrane fuel cells. *Journal of Power Sources* **94** (2001), pp. 40–50.

[16] A. A. Kulikovsky. *Analytical Modeling of Fuel Cells*. Second Edition. Elsevier (2019).

[17] H. D. Baehr and K. Stephan. *Wärme- und Stoffübertragung*. 6. Auflage. Springer (2006).

[18] U. Pasaogullari and C.-Y. Wang. Two-Phase Modeling and Flooding Prediction of Polymer Electrolyte Fuel Cells. *Journal of The Electrochemical Society* **152** (2005).

[19] O. Burheim, P. Vie, J. Pharoah, and S. Kjelstrup. Ex situ measurements of through-plane thermal conductivities in a polymer electrolyte fuel cell. *Journal of Power Sources* **195** (2010), pp. 249–256.

[20] S. Flügge. *Principles of Classical Mechanics and Field Theory*. Encyclopedia of Physics. Springer (1960).

[21] G. Karimi, X. Li, and P. Teertstra. Measurement of through-plane effective thermal conductivity and contact resistance in PEM fuel cell diffusion media. *Electrochimica Acta* **55** (2010), pp. 1619–1625.

[22] The MathWorks Inc. *MATLAB®*. Version 9.9 (R2020b).

[23] T. A. Driscoll, N. Hale, and L. N. Trefethen, eds. *Chebfun Guide*. Pafnuty Publications, Oxford (2014).

[24] T.-F. Cao et al. Modeling the temperature distribution and performance of a PEM fuel cell with thermal contact resistance. *International Journal of Heat and Mass Transfer* **87** (2015), pp. 544–556.

[25] Q. Wang et al. Study on the thermal transient of cathode catalyst layer in proton exchange membrane fuel cell under dynamic loading with a two-dimensional model. *Chemical Engineering Journal* **433** (2022).

[26] H. Wu, P. Berg, and X. Li. Modeling of PEMFC Transients with Finite-Rate Phase-Transfer Processes. *Journal of The Electrochemical Society* **157** (2010).

[27] M. Lampinen and M. Fomino. Analysis of different energy scales in chemical thermodynamics and estimation of free energy and enthalpy changes for half cell reactions. *Acta Polytechnica Scandinavica, Chemical Technology and Metallurgy Series* (1993), p. 45.

[28] *WebPlotDigitizer*. `https://automeris.io/WebPlotDigitizer/`. Accessed: 2022-03.

[29] T.-F. Cao et al. Numerical investigation of the coupled water and thermal management in PEM fuel cell. *Applied Energy* **112** (2013), pp. 1115–1125.

[30] *NIST Chemistry WebBook*. `https://webbook.nist.gov/chemistry/fluid/`. Accessed: 2022-03.

A
Governing equations for multiphase flow

In the following, the governing equations for the non-isothermal two-phase flow PEMFC model are derived from their corresponding integral conservation laws following the quasi-2D approach presented in section 3.1.

A.1 Gas channel

To account for the different orientation of the GC-GDL interface surface at the cathode (C) and anode (A) side in the chosen coordinate system, the following auxilliary variable is introduced

$$\delta_i = \begin{cases} 1, & i = \mathrm{C}\,, \\ -1, & i = \mathrm{A}\,. \end{cases} \tag{A.1}$$

A.1.1 Total mass balance

The total mass balance in integral form reads

$$\int_{\tilde{CV}} \frac{\partial \tilde{\rho}}{\partial \tilde{t}}\,\mathrm{d}\tilde{V} + \oint_{\partial \tilde{CV}} \tilde{\rho}\tilde{\boldsymbol{u}} \cdot \boldsymbol{n}\,\mathrm{d}\tilde{S} = 0\,. \tag{A.2}$$

First, the volume integral is evaluated for the given control volume $\tilde{CV}$ fixed in space, see fig. 3. As the density depends on the $\tilde{x}_1$-direction only, $\tilde{\rho}(\tilde{\boldsymbol{x}}, \tilde{t}) = \bar{\tilde{\rho}}(\tilde{x}_1, \tilde{t})$, one finds

$$\begin{aligned} \int_{\tilde{CV}} \frac{\partial \tilde{\rho}}{\partial \tilde{t}}\,\mathrm{d}\tilde{V} &= \int_0^{\tilde{W}_{\mathrm{GC}}} \int_0^{\tilde{H}_{\mathrm{GC}}} \int_{\tilde{x}_1^*}^{\tilde{x}_1^*+\Delta\tilde{x}_1} \frac{\partial \tilde{\rho}}{\partial \tilde{t}}\,\mathrm{d}\tilde{x}_1\mathrm{d}\tilde{x}_2\mathrm{d}\tilde{x}_3 = \tilde{W}_{\mathrm{GC}}\tilde{H}_{\mathrm{GC}} \int_{\tilde{x}_1^*}^{\tilde{x}_1^*+\Delta\tilde{x}_1} \frac{\partial \bar{\tilde{\rho}}}{\partial \tilde{t}}\,\mathrm{d}\tilde{x}_1 \\ &\approx \tilde{W}_{\mathrm{GC}}\tilde{H}_{\mathrm{GC}}\Delta\tilde{x}_1 \frac{\partial \bar{\tilde{\rho}}}{\partial \tilde{t}}\bigg|_{\tilde{x}_1^*+\Delta\tilde{x}_1/2} = \tilde{W}_{\mathrm{GC}}\tilde{H}_{\mathrm{GC}}\Delta\tilde{x}_1 \frac{\partial \bar{\tilde{\rho}}}{\partial \tilde{t}}\bigg|_{\tilde{x}_1^*} + \mathcal{O}\big(\Delta\tilde{x}_1^2\big)\,. \end{aligned} \tag{A.3}$$

Evaluation of the closed surface integral over $\partial\tilde{CV}$ yields

$$\begin{aligned} \oint_{\partial \tilde{CV}} \tilde{\rho}\tilde{\boldsymbol{u}} \cdot \boldsymbol{n}\,\mathrm{d}\tilde{S} = \int_0^{\tilde{W}_{\mathrm{GC}}} \int_0^{\tilde{H}_{\mathrm{GC}}} \bar{\tilde{\rho}}\tilde{u}_1\Big|_{\tilde{x}_1^*+\Delta\tilde{x}_1} - \bar{\tilde{\rho}}\tilde{u}_1\Big|_{\tilde{x}_1^*} \mathrm{d}\tilde{x}_2\mathrm{d}\tilde{x}_3 \\ + \delta_i \int_0^{\tilde{W}_{\mathrm{GDL}}} \int_{\tilde{x}_1^*}^{\tilde{x}_1^*+\Delta\tilde{x}_1} \varepsilon\tilde{\rho}_{\mathrm{GDL}}\tilde{u}_{2,\mathrm{GDL}}\,\mathrm{d}\tilde{x}_1\mathrm{d}\tilde{x}_3\,, \end{aligned} \tag{A.4}$$

where the last term represents the mass exchange between the GC and GDL. Here the index GDL indicates the value at the adjacent GDL layer. Using the definition of the cross-sectional average

velocity from eq. (3.13) and Taylor series expansion at $\tilde{x}_1^*$ yields for the first term

$$\int_0^{\tilde{W}_{\mathrm{GC}}} \int_0^{\tilde{H}_{\mathrm{GC}}} \bar{\tilde{\rho}}\tilde{u}_1\Big|_{\tilde{x}_1^*+\Delta\tilde{x}_1} - \bar{\tilde{\rho}}\tilde{u}_1\Big|_{\tilde{x}_1^*} \mathrm{d}\tilde{x}_2\mathrm{d}\tilde{x}_3 = \tilde{W}_{\mathrm{GC}}\tilde{H}_{\mathrm{GC}}\left(\bar{\tilde{\rho}}\bar{\tilde{u}}_1\Big|_{\tilde{x}_1+\Delta\tilde{x}_1} - \bar{\tilde{\rho}}\bar{\tilde{u}}_1\Big|_{\tilde{x}_1}\right)$$
$$= \tilde{W}_{\mathrm{GC}}\tilde{H}_{\mathrm{GC}}\Delta\tilde{x}_1\frac{\partial(\bar{\tilde{\rho}}\bar{\tilde{u}}_1)}{\partial\tilde{x}_1}\Big|_{\tilde{x}_1^*} + \mathcal{O}\big(\Delta\tilde{x}_1^2\big)\,. \quad \text{(A.5)}$$

For the GC-GDL interface, whereat $\tilde{u}_2(\tilde{\boldsymbol{x}},\tilde{t}) = \bar{\tilde{u}}_2(\tilde{x}_2,\tilde{t})$ in the GDL, follows

$$\int_0^{\tilde{W}_{\mathrm{GDL}}} \int_{\tilde{x}_1^*}^{\tilde{x}_1^*+\Delta\tilde{x}_1} \varepsilon\tilde{\rho}_{\mathrm{GDL}}\tilde{u}_{2,\mathrm{GDL}}\,\mathrm{d}\tilde{x}_1\mathrm{d}\tilde{x}_3 = \tilde{W}_{\mathrm{GDL}}\int_{\tilde{x}_1^*}^{\tilde{x}_1^*+\Delta\tilde{x}_1} \varepsilon\bar{\tilde{\rho}}_{\mathrm{GDL}}\bar{\tilde{u}}_{2,\mathrm{GDL}}\,\mathrm{d}\tilde{x}_1$$
$$\approx \tilde{W}_{\mathrm{GDL}}\Delta\tilde{x}_1\varepsilon\bar{\tilde{\rho}}_{\mathrm{GDL}}\bar{\tilde{u}}_{2,\mathrm{GDL}}\Big|_{\tilde{x}_1^*+\Delta\tilde{x}_1/2} = \tilde{W}_{\mathrm{GDL}}\Delta\tilde{x}_1\varepsilon\bar{\tilde{\rho}}_{\mathrm{GDL}}\bar{\tilde{u}}_{2,\mathrm{GDL}}\Big|_{\tilde{x}_1^*} + \mathcal{O}\big(\Delta\tilde{x}_1^2\big)\,. \quad \text{(A.6)}$$

Note that the first integral spans over the GDL width $\tilde{W}_{\mathrm{GDL}}$, not only the GC-GDL interface width $\tilde{W}_{\mathrm{GC}}$, to account for the whole mass flow in the GDL domain. Hence, this term represents the total (multiphase) mass transfer between GC and GDL at the interface. Putting together the individual terms yields the dimensional formulation of the total mass balance in the GC

$$\frac{\partial\tilde{\rho}}{\partial\tilde{t}} + \frac{\partial(\tilde{\rho}\tilde{u}_1)}{\partial\tilde{x}_1} = -\delta_i\frac{\tilde{W}_{\mathrm{GDL}}}{\tilde{W}_{\mathrm{GC}}\tilde{H}_{\mathrm{GC}}}\varepsilon\tilde{\rho}_{\mathrm{GDL}}\tilde{u}_{2,\mathrm{GDL}}\,, \quad \text{(A.7)}$$

where the bar indicating average quantities is omitted for better readability. By means of characteristic reference quantities, presented in appendix C, the dimensionless form of the continuity equations in the GC domain can be written as

$$\frac{\partial\rho}{\partial t} + \frac{\partial(\rho u_1)}{\partial x_1} = -K_{\mathrm{cm}}\,\varepsilon\rho_{\mathrm{GDL}}u_{2,\mathrm{GDL}}\,. \quad \text{(A.8)}$$

A.1.2 Liquid phase mass balance

The integral form of the liquid phase mass balance reads

$$\int_{\tilde{C}V}\frac{\partial(\tilde{\rho}_{\mathrm{l}}s)}{\partial\tilde{t}}\,\mathrm{d}\tilde{V} + \oint_{\partial\tilde{C}V}\tilde{\rho}_{\mathrm{l}}s\tilde{\boldsymbol{u}}_{\mathrm{l}}\cdot\boldsymbol{n}\,\mathrm{d}\tilde{S} = \int_{\tilde{C}V}\tilde{\dot{m}}\,\mathrm{d}\tilde{V}\,, \quad \text{(A.9)}$$

where $\tilde{\dot{m}}$ indicates the mass transfer rate into the liquid phase. Since the liquid phase density is assumed to be constant everywhere in the PEMFC and the its velocity is equal to the multiphase mixture velocity in the HFM, evaluation of the integrals in a similar manner to the total mass balance yields (bars omitted)

$$\tilde{\rho}_{\mathrm{l}}\frac{\partial s}{\partial\tilde{t}} + \tilde{\rho}_{\mathrm{l}}\frac{\partial(s\tilde{u}_1)}{\partial\tilde{x}_1} = \tilde{\dot{m}} - \delta_i\frac{\tilde{W}_{\mathrm{GDL}}}{\tilde{W}_{\mathrm{GC}}\tilde{H}_{\mathrm{GC}}}\varepsilon\tilde{\rho}_{\mathrm{l}}s_{\mathrm{GDL}}\tilde{u}_{\mathrm{l},2,\mathrm{GDL}}\,. \quad \text{(A.10)}$$

With the definition of the phase velocity within the multiphase mixture, eq. (2.42),

$$\varepsilon\tilde{\rho}_{\mathrm{l}}s_{\mathrm{GDL}}\tilde{u}_{\mathrm{l},2,\mathrm{GDL}} = \tilde{\psi}_{2,\mathrm{GDL}} + \varepsilon\zeta_{\mathrm{GDL}}\tilde{\rho}_{\mathrm{GDL}}\tilde{u}_{2,\mathrm{GDL}}\,, \quad \text{(A.11)}$$

one finds

$$\tilde{\rho}_\mathrm{l}\frac{\partial s}{\partial \tilde{t}}+\tilde{\rho}_\mathrm{l}\frac{\partial(s\tilde{u}_1)}{\partial \tilde{x}_1}=\tilde{\dot{m}}-\delta_i\frac{\tilde{W}_\mathrm{GDL}}{\tilde{W}_\mathrm{GC}\tilde{H}_\mathrm{GC}}\left[\tilde{\psi}_{2,\mathrm{GDL}}+\varepsilon\zeta_\mathrm{GDL}\tilde{\rho}_\mathrm{GDL}\tilde{u}_{2,\mathrm{GDL}}\right]. \tag{A.12}$$

Here $\psi_{2,\mathrm{GDL}}$ is the capillary diffusion flux of the liquid phase at the GC-GDL interface

$$\tilde{\psi}_{2,\mathrm{GDL}}=\frac{\sqrt{\varepsilon\tilde{\kappa}}\,\cos(\theta_\mathrm{c})\,\tilde{\varsigma}_\mathrm{l}}{\tilde{\nu}_\mathrm{GDL}}\,\zeta_\mathrm{GDL}(1-\zeta_\mathrm{GDL})(J'(s))_\mathrm{GDL}\left(\frac{\partial s}{\partial \tilde{x}_2}\right)_\mathrm{GDL}. \tag{A.13}$$

Introduction of characteristic reference quantities then yields the dimensionless formulation of the liquid phase mass balance in the GC domains

$$\frac{\partial s}{\partial t}+\frac{\partial(su_1)}{\partial x_1}=\dot{m}-K_\mathrm{cl1}\,\psi_{2,\mathrm{GDL}}-K_\mathrm{cl2}\,\varepsilon\,\zeta_\mathrm{GDL}\rho_\mathrm{GDL}u_{2,\mathrm{GDL}}\,, \tag{A.14}$$

with the dimensionless capillary diffusion flux of the liquid phase at the GC-GDL interface

$$\psi_{2,\mathrm{GDL}}=\frac{\zeta_\mathrm{GDL}(1-\zeta_\mathrm{GDL})}{\nu_\mathrm{GDL}}(J'(s))_\mathrm{GDL}\left(\frac{\partial s}{\partial x_2}\right)_\mathrm{GDL}. \tag{A.15}$$

A.1.3 Conservation of species

The integral equation for the conservation of species α within the multiphase mixture reads

$$\int_{\tilde{CV}}\frac{\partial(\tilde{\rho}\xi^\alpha)}{\partial\tilde{t}}\,\mathrm{d}\tilde{V}+\oint_{\partial\tilde{CV}}\tilde{\rho}\xi^\alpha\tilde{\boldsymbol{u}}\cdot\boldsymbol{n}\,\mathrm{d}\tilde{S}=-\oint_{\partial\tilde{CV}}\tilde{\boldsymbol{j}}^\alpha\cdot\boldsymbol{n}\,\mathrm{d}\tilde{S}\,. \tag{A.16}$$

Evaluation of the integrals yields

$$\frac{\partial(\tilde{\rho}\xi^\alpha)}{\partial\tilde{t}}+\frac{\partial(\tilde{\rho}\xi^\alpha\tilde{u}_1)}{\partial\tilde{x}_1}=-\frac{\partial\tilde{j}_1^\alpha}{\partial\tilde{x}_1}-\delta_i\frac{\tilde{W}_\mathrm{GDL}}{\tilde{W}_\mathrm{GC}\tilde{H}_\mathrm{GC}}\left[\tilde{j}^\alpha_{2,\mathrm{GDL}}+\varepsilon\tilde{\rho}_\mathrm{GDL}\xi^\alpha_\mathrm{GDL}\tilde{u}_{2,\mathrm{GDL}}\right]. \tag{A.17}$$

The last term on the RHS represents the total species flux between GC and GDL due to Fickian diffusion in the gas phase and convective multiphase transport. For the capillary porous GDL, two-phase system ($\tilde{\boldsymbol{\psi}}_\mathrm{g}=-\tilde{\boldsymbol{\psi}}_\mathrm{l}$), the latter is expressed as

$$\varepsilon\tilde{\rho}_\mathrm{GDL}\xi^\alpha_\mathrm{GDL}\tilde{u}_{2,\mathrm{GDL}}=\left(\xi^\alpha_{\mathrm{l,GDL}}-\xi^\alpha_{\mathrm{g,GDL}}\right)\tilde{\psi}_{2,\mathrm{GDL}}+\varepsilon\gamma_{\alpha,\mathrm{GDL}}\tilde{\rho}_\mathrm{GDL}\xi^\alpha_\mathrm{GDL}\tilde{u}_{2,\mathrm{GDL}}\,, \tag{A.18}$$

which is a direct consequence of the multiphase species transport in the MMM, see 2.4.3. For the partial mass balance in the GC follows

$$\begin{aligned}\frac{\partial(\tilde{\rho}\xi^\alpha)}{\partial\tilde{t}}+\frac{\partial(\tilde{\rho}\xi^\alpha\tilde{u}_1)}{\partial\tilde{x}_1}&=-\frac{\partial\tilde{j}_1^\alpha}{\partial\tilde{x}_1}\\&\quad-\frac{\tilde{W}_\mathrm{GDL}}{\tilde{W}_\mathrm{GC}\tilde{H}_\mathrm{GC}}\left[\tilde{j}^\alpha_{2,\mathrm{GDL}}+\left(\xi^\alpha_{\mathrm{l,GDL}}-\xi^\alpha_{\mathrm{g,GDL}}\right)\tilde{\psi}_{2,\mathrm{GDL}}+\varepsilon\gamma_{\alpha,\mathrm{GDL}}\tilde{\rho}_\mathrm{GDL}\xi^\alpha_\mathrm{GDL}\tilde{u}_{2,\mathrm{GDL}}\right].\end{aligned} \tag{A.19}$$

Inserting the definition of the multiphase mixture mass fraction, eq. (2.17), as well as TMB, eq. (A.7), and LMB, eq. (A.12), into the equation above yields for constant liquid phase density and constant mass fractions within the liquid phase ($\xi_\mathrm{l}^{\mathrm{H_2O}}=1$)

$$(1-s)\tilde{\rho}_\mathrm{g}\frac{\partial\xi^\alpha_\mathrm{g}}{\partial\tilde{t}}+(1-s)\tilde{\rho}_\mathrm{g}\tilde{u}_1\frac{\partial\xi^\alpha_\mathrm{g}}{\partial\tilde{x}_1}=-\frac{\partial\tilde{j}_1^\alpha}{\partial\tilde{x}_1}-\left(\xi^\alpha_\mathrm{l}-\xi^\alpha_\mathrm{g}\right)\tilde{\dot{m}}-\delta_i\frac{\tilde{W}_\mathrm{GDL}}{\tilde{W}_\mathrm{GC}\tilde{H}_\mathrm{GC}}\tilde{j}^\alpha_{2,\mathrm{GDL}}\,. \tag{A.20}$$

For the reactant species β ($= O_2/H_2$) and H_2O follows

$$(1-s)\tilde{\rho}_\mathrm{g}\frac{\partial \xi_\mathrm{g}^\beta}{\partial \tilde{t}} + (1-s)\tilde{\rho}_\mathrm{g}\tilde{u}_1\frac{\partial \xi_\mathrm{g}^\beta}{\partial \tilde{x}_1} = -\frac{\partial \tilde{j}_1^\beta}{\partial \tilde{x}_1} + \xi_\mathrm{g}^\beta \tilde{\dot{m}} - \delta_i \frac{\tilde{W}_\mathrm{GDL}}{\tilde{W}_\mathrm{GC}\tilde{H}_\mathrm{GC}}\tilde{j}_{2,\mathrm{GDL}}^\beta\,, \tag{A.21}$$

$$(1-s)\tilde{\rho}_\mathrm{g}\frac{\partial \xi_\mathrm{g}^{H_2O}}{\partial \tilde{t}} + (1-s)\tilde{\rho}_\mathrm{g}\tilde{u}_1\frac{\partial \xi_\mathrm{g}^{H_2O}}{\partial \tilde{x}_1} = -\frac{\partial \tilde{j}_1^{H_2O}}{\partial \tilde{x}_1} - (1-\xi_\mathrm{g}^{H_2O})\tilde{\dot{m}} - \delta_i \frac{\tilde{W}_\mathrm{GDL}}{\tilde{W}_\mathrm{GC}\tilde{H}_\mathrm{GC}}\tilde{j}_{2,\mathrm{GDL}}^{H_2O}\,. \tag{A.22}$$

By means of characteristic reference quantities, the dimensionless form of the corresponding conservation equations yield

$$(1-s)\rho_\mathrm{g}\left[\frac{\partial \xi_\mathrm{g}^\beta}{\partial t} + u_1\frac{\partial \xi_\mathrm{g}^\beta}{\partial x_1}\right] = -K_{\mathrm{cs}1}\frac{\partial j_1^\beta}{\partial x_1} + K_\rho\,\xi_\mathrm{g}^\beta \dot{m} - K_{\mathrm{cs}2}\,j_{2,\mathrm{GDL}}^\beta\,, \tag{A.23}$$

$$(1-s)\rho_\mathrm{g}\left[\frac{\partial \xi_\mathrm{g}^{H_2O}}{\partial t} + u_1\frac{\partial \xi_\mathrm{g}^{H_2O}}{\partial x_1}\right] = -K_{\mathrm{cs}1}\frac{\partial j_1^{H_2O}}{\partial x_1} - K_\rho\left(1-\xi_\mathrm{g}^{H_2O}\right)\dot{m} - K_{\mathrm{cs}2}\,j_{2,\mathrm{GDL}}^{H_2O}\,. \tag{A.24}$$

The dimensionless form of the two diffusive species fluxes in the GCs is given by

$$j_1^\beta = -(1-s)\rho_\mathrm{g}\left(\mathcal{D}_{\beta,\beta}\frac{\partial \xi_\mathrm{g}^\beta}{\partial x_1} + \mathcal{D}_{\beta,H_2O}\frac{\partial \xi_\mathrm{g}^{H_2O}}{\partial x_1}\right), \tag{A.25}$$

$$j_1^{H_2O} = -(1-s)\rho_\mathrm{g}\left(\mathcal{D}_{H_2O,\beta}\frac{\partial \xi_\mathrm{g}^\beta}{\partial x_1} + \mathcal{D}_{H_2O,H_2O}\frac{\partial \xi_\mathrm{g}^{H_2O}}{\partial x_1}\right), \tag{A.26}$$

whereas the third flux is used to close the system,

$$j_1^\beta + j_1^{H_2O} + j_1^{N_2} = 0\,. \tag{A.27}$$

A.1.4 Conservation of energy

No mechanical power is fed to the system and gravitational effects are neglected in the quasi-2D formulation. Hence, the integral equation for the conservation of energy reads

$$\int_{\tilde{CV}} \frac{\partial(\tilde{\rho}\tilde{h})}{\partial \tilde{t}}\,\mathrm{d}\tilde{V} + \oint_{\partial\tilde{CV}} \tilde{\rho}\tilde{h}\tilde{\boldsymbol{u}}\cdot\boldsymbol{n}\,\mathrm{d}\tilde{S} = -\oint_{\partial\tilde{CV}} \tilde{\boldsymbol{r}}\cdot\boldsymbol{n}\,\mathrm{d}\tilde{S} - \oint_{\partial\tilde{CV}} \tilde{\boldsymbol{q}}\cdot\boldsymbol{n}\,\mathrm{d}\tilde{S} + \int_{\tilde{CV}} \tilde{Q}_\mathrm{source}\,\mathrm{d}\tilde{V}\,. \tag{A.28}$$

Here, $\tilde{\boldsymbol{r}}$ denotes diffusive enthalpy fluxes from eq. (3.6). In the GC the heat flux $\tilde{\boldsymbol{q}}$ consists of two components: One for the convective heat transfer between BPs/GDL and fluid and one describing thermal conduction in the fluid. The prior dimensional analysis shows that the latter is negligible, as well as kinetic energy and friction stresses. For the heat flux follows

$$\tilde{\boldsymbol{q}} = \tilde{\alpha}\left(\tilde{T} - \tilde{T}_\mathrm{BP/GDL}\right)\boldsymbol{n}\,. \tag{A.29}$$

In contrary to mass and enthalpy transport the surface integral for the GC-GDL interface containing heat fluxes is evaluated for the actual contact area between GC and GDL only. The remaining heat

flux is transported directly to the bipolar plates. Hence, the closed heat flux surface integral over $\partial \tilde{CV}$ can be decomposed as

$$\oint_{\partial \tilde{CV}} \tilde{\boldsymbol{q}} \cdot \boldsymbol{n} \, \mathrm{d}\tilde{S} = \int_0^{\tilde{W}_{\mathrm{GC}}} \int_{\tilde{x}_1^*}^{\tilde{x}_1^*+\Delta\tilde{x}_1} \tilde{q}_{\mathrm{BP}} \, \mathrm{d}\tilde{x}_1 \mathrm{d}\tilde{x}_3 + 2 \int_0^{\tilde{H}_{\mathrm{GC}}} \int_{\tilde{x}_1^*}^{\tilde{x}_1^*+\Delta\tilde{x}_1} \tilde{q}_{\mathrm{BP}} \, \mathrm{d}\tilde{x}_1 \mathrm{d}\tilde{x}_2 + \int_0^{\tilde{W}_{\mathrm{GC}}} \int_{\tilde{x}_1^*}^{\tilde{x}_1^*+\Delta\tilde{x}_1} \tilde{q}_{\mathrm{GDL}} \, \mathrm{d}\tilde{x}_1 \mathrm{d}\tilde{x}_3 \,. \quad \text{(A.30)}$$

The heat source term $\tilde{Q}_{\mathrm{source}}$ is due to the evaporation/condensation of water and is calculated from eq. (1.20). Evaluating all the integrals in the energy balance finally yields

$$\frac{\partial(\tilde{\rho}\tilde{h})}{\partial \tilde{t}} + \frac{\partial(\tilde{\rho}\tilde{h}\tilde{u}_1)}{\partial \tilde{x}_1} = -\frac{\partial \tilde{r}_1}{\partial \tilde{x}_1} - \frac{\tilde{\alpha}}{\tilde{H}_{\mathrm{GC}}}\left(\tilde{T} - \tilde{T}_{\mathrm{BP}}\right) - 2\frac{\tilde{\alpha}}{\tilde{W}_{\mathrm{GC}}}\left(\tilde{T} - \tilde{T}_{\mathrm{BP}}\right) - \frac{\tilde{\alpha}_{\mathrm{GDL}}}{\tilde{H}_{\mathrm{GC}}}\left(\tilde{T} - \tilde{T}_{\mathrm{GDL}}\right) + \Delta_{\mathrm{lv}}\tilde{H}\,\tilde{\dot{m}}_1 - \delta_i \frac{\tilde{W}_{\mathrm{GDL}}}{\tilde{W}_{\mathrm{GC}}\tilde{H}_{\mathrm{GC}}}\left[\varepsilon\tilde{\rho}_{\mathrm{GDL}}\tilde{h}\tilde{u}_{2,\mathrm{GDL}} + \tilde{r}_{2,\mathrm{GDL}}\right]. \quad \text{(A.31)}$$

Inserting the TMB, eq. (A.7), into the equation above and considering the MMM formulation for convective enthalpy fluxes simplifies the GC energy balance to

$$\tilde{\rho}\frac{\partial \tilde{h}}{\partial \tilde{t}} + \tilde{\rho}\tilde{u}_1\frac{\partial \tilde{h}}{\partial \tilde{x}_1} = -\frac{\partial \tilde{r}_1}{\partial \tilde{x}_1} - \frac{\tilde{\alpha}}{\tilde{H}_{\mathrm{GC}}}\left(\tilde{T} - \tilde{T}_{\mathrm{BP}}\right) - 2\,\frac{\tilde{\alpha}}{\tilde{W}_{\mathrm{GC}}}\left(\tilde{T} - \tilde{T}_{\mathrm{BP}}\right) - \frac{\tilde{\alpha}_{\mathrm{GDL}}}{\tilde{H}_{\mathrm{GC}}}\left(\tilde{T} - \tilde{T}_{\mathrm{GDL}}\right) + \Delta_{\mathrm{lv}}\tilde{H}\,\tilde{\dot{m}} - \delta_i \frac{\tilde{W}_{\mathrm{GDL}}}{\tilde{W}_{\mathrm{GC}}\tilde{H}_{\mathrm{GC}}}\tilde{r}_{2,\mathrm{GDL}}\,. \quad \text{(A.32)}$$

With the definition of the mixture enthalpy, eq. (3.10), decomposition of the enthalpy diffusion flux into its two constituents, eq. (3.6), and introduction of characteristic reference values, the dimensionless formulation of the conservation of energy in the GC domain then can be written as

$$\rho\frac{\partial(c_{\mathrm{p}}T)}{\partial t} + \rho u_1\frac{\partial(c_{\mathrm{p}}T)}{\partial x_1} = -K_{\mathrm{ce1}}\frac{\partial(T j_1^{\beta})}{\partial x_1} - K_{\mathrm{ce2}}\frac{\partial(T j_1^{\mathrm{H_2O}})}{\partial x_1} - K_{\mathrm{ce3}}\,(T - T_{\mathrm{BP}}) - 2\,K_{\mathrm{ce4}}\,(T - T_{\mathrm{BP}}) - K_{\mathrm{ce5}}\,(T - T_{\mathrm{GDL}}) + K_{\mathrm{ce6}}\,\dot{m} - K_{\mathrm{ce7}}\,T j_{2,\mathrm{GDL}}^{\beta} - K_{\mathrm{ce8}}\,T j_{2,\mathrm{GDL}}^{\mathrm{H_2O}}\,. \quad \text{(A.33)}$$

A.1.5 Conservation of momentum

The integral formulation of the conservation of momentum for the homogeneous multiphase mixture reads

$$\int_{\tilde{CV}} \frac{\partial(\tilde{\rho}\tilde{\boldsymbol{u}})}{\partial \tilde{t}}\,\mathrm{d}\tilde{V} + \oint_{\partial \tilde{CV}} \tilde{\rho}\tilde{\boldsymbol{u}}(\tilde{\boldsymbol{u}}\cdot\boldsymbol{n})\,\mathrm{d}\tilde{S} = -\oint_{\partial \tilde{CV}} \tilde{p}\boldsymbol{n}\,\mathrm{d}\tilde{S} + \oint_{\partial \tilde{CV}} \tilde{\mu}_{\mathrm{g}}\left(\tilde{\nabla}\otimes\tilde{\boldsymbol{u}} + \left(\tilde{\nabla}\otimes\tilde{\boldsymbol{u}}\right)^T\right)\cdot\boldsymbol{n}\,\mathrm{d}\tilde{S}. \quad \text{(A.34)}$$

In the HFM only surface forces on the continuous phase, in this case the gas phase, have to be considered. The derivation of the 1D governing equation is identical to that of [1] and yields

$$\frac{\partial(\tilde{\rho}\tilde{u}_1)}{\partial \tilde{t}} + F_{u^2}\frac{\partial(\tilde{\rho}\tilde{u}_1^2)}{\partial \tilde{x}_1} + \frac{\partial \tilde{p}_{\mathrm{g}}}{\partial \tilde{x}_1} = 2\,\frac{\partial}{\partial \tilde{x}_1}\left(\tilde{\mu}_{\mathrm{g}}\frac{\partial \tilde{u}_1}{\partial \tilde{x}_1}\right) - F_c\frac{\tilde{W}_{\mathrm{GC}}\,\tilde{H}_{\mathrm{GC}}}{\tilde{W}_{\mathrm{GC}}\,\tilde{H}_{\mathrm{GC}}}\frac{16}{\tilde{D}_{\mathrm{H}}}\tilde{\mu}_{\mathrm{g}}\tilde{u}_1\,. \quad \text{(A.35)}$$

For the dimensionless formulation follows

$$\frac{\partial(\rho u_1)}{\partial t} + F_{u^2}\frac{\partial(\rho u_1^2)}{\partial x_1} + \frac{\partial p_\mathrm{g}}{\partial x_1} = -K_\mathrm{cu}\,\mu_\mathrm{g} u_1\,. \tag{A.36}$$

A.2 Gas-diffusion-layer

Due to the absence of walls inside the GDL, the velocity and temperature profile are assumed to be constant across x_1 and x_3. Therefore, within the quasi-2D concept the GDL can immediately be treated 1D for each corresponding inner slice. For details see [1].

A.2.1 Total mass balance

Evaluating the total mass balance from eq. (A.2) for a control volume with dimensions $\tilde{W}_\mathrm{GDL} \times \tilde{W}_\mathrm{SL} \times \Delta\tilde{x}_2$ in an analogous way to the GC yields

$$\frac{\partial\tilde{\rho}}{\partial\tilde{t}} + \frac{\partial(\tilde{\rho}\tilde{u}_2)}{\partial\tilde{x}_2} = 0\,, \tag{A.37}$$

and for the dimensionless form follows

$$\frac{\partial\rho}{\partial t} + \frac{\partial(\rho u_2)}{\partial x_2} = 0\,. \tag{A.38}$$

In contrary to the the GC, no source term appears at the RHS.

A.2.2 Liquid phase mass balance

The liquid phase mass balance reads

$$\int_{\tilde{CV}} \frac{\partial(\tilde{\rho}_\mathrm{l} s)}{\partial\tilde{t}}\,\mathrm{d}\tilde{V} + \oint_{\partial\tilde{CV}} \tilde{\rho}_\mathrm{l} s\tilde{\boldsymbol{u}}_\mathrm{l}\cdot\boldsymbol{n}\,\mathrm{d}\tilde{S} = \int_{\tilde{CV}} \tilde{\dot{m}}\,\mathrm{d}\tilde{V}. \tag{A.39}$$

Evaluation of the integrals yields

$$\tilde{\rho}_\mathrm{l}\frac{\partial s}{\partial\tilde{t}} + \frac{\partial(\tilde{\rho}_\mathrm{l} s\tilde{u}_{\mathrm{l},2})}{\partial\tilde{x}_2} = \tilde{\dot{m}} \tag{A.40}$$

Using the definition of the phase velocities from the MMM, eq. (2.42), this can be rewritten as

$$\tilde{\rho}_\mathrm{l}\frac{\partial s}{\partial\tilde{t}} + \frac{\partial(\zeta\tilde{\rho}\tilde{u}_2)}{\partial\tilde{x}_2} = \tilde{\dot{m}} - \frac{1}{\varepsilon}\frac{\partial\tilde{\psi}_2}{\partial\tilde{x}_2}\,, \tag{A.41}$$

with the capillary diffusion flux of the liquid phase

$$\tilde{\psi}_2 = \frac{\sqrt{\varepsilon\tilde{\kappa}}\,\cos(\theta_\mathrm{c})\,\tilde{\varsigma}}{\tilde{\nu}}\,\zeta(1-\zeta)\,J'(s)\,\frac{\partial s}{\partial\tilde{x}_2}\,. \tag{A.42}$$

By means of characteristic reference quantities, the dimensionless form of the liquid phase mass balance in the GDL yields

$$\frac{\partial s}{\partial t} + K_\rho\frac{\partial(\zeta\rho u_2)}{\partial x_2} = \dot{m} - \frac{K_\mathrm{gl}}{\varepsilon}\frac{\partial\psi_2}{\partial x_2}\,, \tag{A.43}$$

with the dimensionless liquid phase capillary diffusion flux

$$\psi_2 = \frac{\zeta(1-\zeta)}{\nu}\,J'(s)\frac{\partial s}{\partial x_2}\,. \tag{A.44}$$

A.2.3 Conservation of species

The integral form of the conservation of species α in the GDL reads

$$\varepsilon \int_{C\tilde{V}} \frac{\partial(\tilde{\rho}\xi^{\alpha})}{\partial \tilde{t}}\,\mathrm{d}\tilde{V} + \varepsilon \oint_{\partial C\tilde{V}} \gamma_{\alpha}\tilde{\rho}\xi^{\alpha}\tilde{\boldsymbol{u}}\cdot\boldsymbol{n}\,\mathrm{d}\tilde{S} = -\oint_{\partial C\tilde{V}} \tilde{\boldsymbol{j}}^{\alpha}\cdot\boldsymbol{n}\,\mathrm{d}\tilde{S} - \oint_{\partial C\tilde{V}} (\xi_{\mathrm{l}}^{\alpha}-\xi_{\mathrm{g}}^{\alpha})\tilde{\boldsymbol{\psi}}\cdot\boldsymbol{n}\,\mathrm{d}\tilde{S}\,. \quad \text{(A.45)}$$

Evaluation of the integrals yields

$$\varepsilon\left[\frac{\partial(\tilde{\rho}\xi^{\alpha})}{\partial\tilde{t}} + \frac{\partial(\gamma_{\alpha}\tilde{\rho}\xi^{\alpha}\tilde{u}_2)}{\partial\tilde{x}_2}\right] = -\frac{\partial\tilde{j}_2^{\alpha}}{\partial\tilde{x}_2} - \frac{\partial}{\partial\tilde{x}_2}\Big((\xi_{\mathrm{l}}^{\alpha}-\xi_{\mathrm{g}}^{\alpha})\tilde{\psi}_2\Big)\,. \quad \text{(A.46)}$$

For the reactant species β and H_2O follows

$$\varepsilon\left[\frac{\partial(\tilde{\rho}_{\mathrm{g}}(1-s)\xi_{\mathrm{g}}^{\beta})}{\partial\tilde{t}} + \frac{\partial(\gamma_{\beta}\tilde{\rho}_{\mathrm{g}}(1-s)\xi_{\mathrm{g}}^{\beta}\tilde{u}_2)}{\partial\tilde{x}_2}\right] = -\frac{\partial\tilde{j}_2^{\beta}}{\partial\tilde{x}_2} + \frac{\partial(\xi_{\mathrm{g}}^{\beta}\tilde{\psi}_2)}{\partial\tilde{x}_2}\,, \quad \text{(A.47)}$$

$$\varepsilon\tilde{\rho}_{\mathrm{l}}\left[\frac{\partial s}{\partial\tilde{t}} + \frac{\partial(\gamma_{\mathrm{H_2O}}s\tilde{u}_2)}{\partial\tilde{x}_2}\right] + \varepsilon\left[\frac{\partial(\tilde{\rho}_{\mathrm{g}}(1-s)\xi_{\mathrm{g}}^{\mathrm{H_2O}})}{\partial\tilde{t}} + \frac{\partial(\gamma_{\mathrm{H_2O}}\tilde{\rho}_{\mathrm{g}}(1-s)\xi_{\mathrm{g}}^{\mathrm{H_2O}}\tilde{u}_2)}{\partial\tilde{x}_2}\right] =$$
$$-\frac{\partial\tilde{j}_2^{\mathrm{O_2}}}{\partial\tilde{x}_2} - \frac{\partial}{\partial\tilde{x}_2}\Big(\Big(\xi_{\mathrm{l}}^{\mathrm{H_2O}}-\xi_{\mathrm{g}}^{\mathrm{H_2O}}\Big)\tilde{\psi}_2\Big)\,. \quad \text{(A.48)}$$

By means of characteristic reference quantities, the dimensionless form of the conservation of species equations for the GDL domain yield

$$\varepsilon\left[\frac{\partial(\rho_{\mathrm{g}}(1-s)\xi_{\mathrm{g}}^{\beta})}{\partial t} + \frac{\partial(\gamma_{\beta}\rho_{\mathrm{g}}(1-s)\xi_{\mathrm{g}}^{\beta}u_2)}{\partial x_2}\right] = -\frac{\partial j_2^{\beta}}{\partial x_2} + K_{\mathrm{gs}}\frac{\partial(\xi_{\mathrm{g}}^{\beta}\psi_2)}{\partial x_2}\,, \quad \text{(A.49)}$$

$$\frac{\varepsilon}{K_{\rho}}\left[\frac{\partial s}{\partial t} + \frac{\partial(\gamma_{\mathrm{H_2O}}su_2)}{\partial x_2}\right] + \varepsilon\left[\frac{\partial(\rho_{\mathrm{g}}(1-s)\xi_{\mathrm{g}}^{\mathrm{H_2O}})}{\partial t} + \frac{\partial(\gamma_{\mathrm{H_2O}}\rho_{\mathrm{g}}(1-s)\xi_{\mathrm{g}}^{\mathrm{H_2O}}u_2)}{\partial x_2}\right] =$$
$$-\frac{\partial j_2^{\mathrm{H_2O}}}{\partial x_2} - K_{\mathrm{gs}}\frac{\partial}{\partial x_2}\big((1-\xi_{\mathrm{g}}^{\mathrm{H_2O}})\psi_2\big)\,. \quad \text{(A.50)}$$

Here, the two diffusive species fluxes in dimensionless form are given by

$$j_2^{\beta} = -(\varepsilon(1-s))^{1.5}\rho_{\mathrm{g}}\left(\mathcal{D}_{\beta,\beta}\frac{\partial\xi_{\mathrm{g}}^{\beta}}{\partial x_2} + \mathcal{D}_{\beta,\mathrm{H_2O}}\frac{\partial\xi_{\mathrm{g}}^{\mathrm{H_2O}}}{\partial x_2}\right), \quad \text{(A.51)}$$

$$j_2^{\mathrm{H_2O}} = -(\varepsilon(1-s))^{1.5}\rho_{\mathrm{g}}\left(\mathcal{D}_{\mathrm{H_2O},\beta}\frac{\partial\xi_{\mathrm{g}}^{\beta}}{\partial x_2} + \mathcal{D}_{\mathrm{H_2O},\mathrm{H_2O}}\frac{\partial\xi_{\mathrm{g}}^{\mathrm{H_2O}}}{\partial x_2}\right), \quad \text{(A.52)}$$

whereas the third flux is used to close the system,

$$j_2^{\beta} + j_2^{\mathrm{H_2O}} + j_2^{\mathrm{N_2}} = 0\,. \quad \text{(A.53)}$$

A.2.4 Conservation of energy

The integral form of the conservation of energy in the GDL reads

$$(1-\varepsilon)\int_{\tilde{C}\tilde{V}}\frac{\partial(\tilde{\rho}_\mathrm{s}\tilde{h}_s)}{\partial\tilde{t}}\mathrm{d}\tilde{V}+\varepsilon\int_{\tilde{C}\tilde{V}}\frac{\partial(\tilde{\rho}\tilde{h})}{\partial\tilde{t}}\mathrm{d}\tilde{V}+\varepsilon\oint_{\partial\tilde{C}\tilde{V}}\gamma_\mathrm{h}\tilde{\rho}\tilde{h}\tilde{\boldsymbol{u}}\cdot\boldsymbol{n}\,\mathrm{d}\tilde{S}=-\oint_{\partial\tilde{C}\tilde{V}}\tilde{\boldsymbol{r}}\cdot\boldsymbol{n}\,\mathrm{d}\tilde{S}$$
$$-\oint_{\partial\tilde{C}\tilde{V}}\tilde{\boldsymbol{q}}\cdot\boldsymbol{n}\,\mathrm{d}\tilde{S}-\oint_{\partial\tilde{C}\tilde{V}}\left(\tilde{h}_\mathrm{l}-\tilde{h}_\mathrm{g}\right)\tilde{\boldsymbol{\psi}}\cdot\boldsymbol{n}\,\mathrm{d}\tilde{S}+\int_{\tilde{C}\tilde{V}}\tilde{Q}_\mathrm{source}\,\mathrm{d}\tilde{V}\quad(\mathrm{A}.54)$$

Dimensional analysis shows that Joule heating in the GDL is negligible and the only relevant heat source term is due to the latent heat of water evaporation and condensation. Hence, evaluation of the integrals yields

$$(1-\varepsilon)\frac{\partial(\tilde{\rho}_\mathrm{s}\tilde{h}_\mathrm{s})}{\partial\tilde{t}}+\varepsilon\left[\frac{\partial(\tilde{\rho}\tilde{h})}{\partial\tilde{t}}+\frac{\partial(\gamma_\mathrm{h}\tilde{\rho}\tilde{h}\tilde{u}_2)}{\partial\tilde{x}_2}\right]=-\frac{\partial\tilde{r}_2}{\partial\tilde{x}_2}-\frac{\partial\tilde{q}_2}{\partial\tilde{x}_2}-\frac{\partial}{\partial\tilde{x}_2}\left(\left(\tilde{h}_\mathrm{l}-\tilde{h}_\mathrm{g}\right)\tilde{\psi}_2\right)+\Delta_\mathrm{lv}\tilde{H}\,\tilde{\dot{m}}\,.\quad(\mathrm{A}.55)$$

The non-dimensional formulation of the energy balance in the GDL domain then reads

$$K_\mathrm{ge1}\,(1-\varepsilon)\frac{\partial T}{\partial t}+\varepsilon\left[\frac{\partial(\rho c_\mathrm{p}T)}{\partial t}+\frac{\partial(\gamma_\mathrm{h}\rho c_\mathrm{p}Tu_2)}{\partial x_2}\right]=-K_\mathrm{ge2}\frac{\partial(Tj_2^{\beta})}{\partial x_2}-K_\mathrm{ge3}\frac{\partial(Tj_2^{\mathrm{H_2O}})}{\partial x_2}$$
$$+K_\mathrm{ge4}\frac{\partial}{\partial x_2}\left(k_\mathrm{eff}\frac{\partial}{\partial x_2}T\right)+K_\mathrm{ge5}\,\varepsilon\,\dot{m}-K_\mathrm{ge6}\frac{\partial(T\psi_2)}{\partial x_2}+K_\mathrm{ge7}\frac{\partial(c_{\mathrm{p_g}}T\psi_2)}{\partial x_2}\,.\quad(\mathrm{A}.56)$$

A.2.5 Conservation of momentum

As in the GC domain, the derivation for the equation of motion in the GDL is identical to [1]. The second RHS term in the integral equation for the conservation of momentum,

$$\int_{\tilde{C}\tilde{V}}\frac{\partial(\tilde{\rho}\tilde{\boldsymbol{u}})}{\partial\tilde{t}}\,\mathrm{d}\tilde{V}+\oint_{\partial\tilde{C}\tilde{V}}\tilde{\rho}\tilde{\boldsymbol{u}}(\tilde{\boldsymbol{u}}\cdot\boldsymbol{n})\,\mathrm{d}\tilde{S}=-\oint_{\partial\tilde{C}\tilde{V}}\tilde{p}\boldsymbol{n}\,\mathrm{d}\tilde{S}+\int_{\tilde{C}\tilde{V}}\varepsilon\frac{\tilde{\mu}}{\tilde{\kappa}}\tilde{\boldsymbol{u}}\,\mathrm{d}\tilde{V}$$
$$+\oint_{\partial\tilde{C}\tilde{V}}\tilde{\mu}\left(\tilde{\nabla}\otimes\tilde{\boldsymbol{u}}+\left(\tilde{\nabla}\otimes\tilde{\boldsymbol{u}}\right)^T\right)\cdot\boldsymbol{n}\,\mathrm{d}\tilde{S}\,.\quad(\mathrm{A}.57)$$

represents the source term for the additional pressure drop in the porous layers. By means of characteristic reference quantities, the dimensionless formulation of the equation of motion in the GDL domain yields

$$\frac{\partial(\rho u_2)}{\partial t}+F_{u^2}\frac{\partial(\rho u^2)}{\partial x_2}+\frac{\partial p}{\partial x_2}=-K_\mathrm{gu1}\,\mu u_2+K_\mathrm{gu2}\frac{\partial}{\partial x_2}\left(\mu\frac{\partial u_2}{\partial x_2}\right).\quad(\mathrm{A}.58)$$

B

Governing equations for non-isothermal single phase flow

The non-dimensional governing equations for the case of non-isothermal single phase flow, where liquid saturation is fixed at $s = 0$, further used for all the presented simulations in section 5, are presented in the following. The corresponding source terms are listed in table 6. The PEM model remains unchanged. For the GC and GDL domain $a = 1$ and $a = 2$, respectively.

Total mass balance:

$$\frac{\partial \rho_\mathrm{g}}{\partial t} + \frac{\partial (\rho_\mathrm{g} u_a)}{\partial x_a} = S_m \,, \tag{B.1}$$

Species mass balances:

$$\rho_\mathrm{g} \frac{\partial \xi_\mathrm{g}^\beta}{\partial t} + \rho_\mathrm{g} u_a \frac{\partial \xi_\mathrm{g}^\beta}{\partial x_a} = S_s^\beta \,, \tag{B.2}$$

$$\rho_\mathrm{g} \frac{\partial \xi_\mathrm{g}^{\mathrm{H_2O}}}{\partial t} + \rho_\mathrm{g} u_a \frac{\partial \xi_\mathrm{g}^{\mathrm{H_2O}}}{\partial x_a} = S_s^{\mathrm{H_2O}} \,, \tag{B.3}$$

Energy balance:

$$\rho_\mathrm{g} \frac{\partial (c_\mathrm{p} T)}{\partial t} + \rho_\mathrm{g} u_a \frac{\partial (c_\mathrm{p} T)}{\partial x_a} = S_e \,, \tag{B.4}$$

Momentum balance:

$$\frac{\partial (\rho_\mathrm{g} u_a)}{\partial t} + F_{\mathrm{u},a} \frac{\partial (\rho_\mathrm{g} u_a^2)}{\partial x_a} + \frac{\partial p}{\partial x_a} = S_u \,, \tag{B.5}$$

Closure equation:

$$\sum_\alpha \xi_\mathrm{g}^\alpha = 1 \,, \tag{B.6}$$

Equation of state:

$$K_\mathrm{eos}\, T \rho_\mathrm{g} \sum_\alpha \frac{\xi^\alpha}{M^\alpha} = p \,. \tag{B.7}$$

The two diffusive species fluxes in dimensionless form are given by

$$j_a^\beta = -\varepsilon^q \rho_\mathrm{g} \left(\mathcal{D}_{\beta,\beta} \frac{\partial \xi_\mathrm{g}^\beta}{\partial x_a} + \mathcal{D}_{\beta,\mathrm{H_2O}} \frac{\partial \xi_\mathrm{g}^{\mathrm{H_2O}}}{\partial x_a} \right) , \tag{B.8}$$

$$j_a^{\mathrm{H_2O}} = -\varepsilon^q \rho_\mathrm{g} \left(\mathcal{D}_{\mathrm{H_2O},\beta} \frac{\partial \xi_\mathrm{g}^\beta}{\partial x_a} + \mathcal{D}_{\mathrm{H_2O},\mathrm{H_2O}} \frac{\partial \xi_\mathrm{g}^{\mathrm{H_2O}}}{\partial x_a} \right) , \tag{B.9}$$

whereas the third flux is used to close the system,

$$j_a^\beta + j_a^{\mathrm{H_2O}} + j_a^{\mathrm{N_2}} = 0 \,. \tag{B.10}$$

	gas channels $(a = 1)$
S_m	$-K_\mathrm{cm}\,\varepsilon\rho_\mathrm{g}u_2$
S_u	$-K_\mathrm{cu1}\,\mu u_1$
S_s^β	$-K_\mathrm{cs1}\,\dfrac{\partial j_1^\beta}{\partial x_1} - K_\mathrm{cs2}\,j_2^\beta$
$S_\mathrm{s}^{\mathrm{H_2O}}$	$-K_\mathrm{cs1}\,\dfrac{\partial j_1^{\mathrm{H_2O}}}{\partial x_1} - K_\mathrm{cs2}\,j_2^{\mathrm{H_2O}}$
S_e	$q - K_\mathrm{ce1}\,\dfrac{\partial(Tj_1^\beta)}{\partial x_1} - K_\mathrm{ce2}\,\dfrac{\partial(Tj_1^{\mathrm{H_2O}})}{\partial x_1} - K_\mathrm{ce7}\,Tj_2^\beta - K_\mathrm{ce8}\,Tj_2^{\mathrm{H_2O}}$
q	$-K_\mathrm{ce3}\,(T - T_\mathrm{BP}) - 2\,K_\mathrm{ce4}\,(T - T_\mathrm{BP}) - K_\mathrm{ce5}\,(T - T_\mathrm{GDL})$
	gas diffusion layers $(a = 2)$
S_m	0
S_u	$-K_\mathrm{gu1}\;\mu u_2 + K_\mathrm{gu2}\,\dfrac{\partial}{\partial x_2}\left(\mu\dfrac{\partial u_2}{\partial x_2}\right)$
S_s^β	$-\dfrac{1}{\varepsilon}\dfrac{\partial j_2^\beta}{\partial x_2}$
$S_\mathrm{s}^{\mathrm{H_2O}}$	$-\dfrac{1}{\varepsilon}\dfrac{\partial j_2^{\mathrm{H_2O}}}{\partial x_2}$
S_e	$-K_\mathrm{ge1}\,\dfrac{\partial T}{\partial t} - K_\mathrm{ge2}\,\dfrac{\partial(Tj_2^\beta)}{\partial x_2} - K_\mathrm{ge3}\,\dfrac{\partial(Tj_2^{\mathrm{H_2O}})}{\partial x_2} + K_\mathrm{ge4}\dfrac{\partial q}{\partial x_2}$
q	$k_\mathrm{eff}\dfrac{\partial T}{x_2}$

Table 6: The non-dimensional source terms for the conservation laws of the non-isothermal single phase model in the GC and GDL domain.

The extended single phase model consists of five PDEs for mass, heat and momentum transfer, and two algebraic expressions for the gas mass faction closure condition and the equation of state. Seven unknown variables are identified:

- velocity u_a,
- pressure p,
- gas density ρ_g,
- β mass fraction ξ_g^β,
- $\mathrm{N_2}$ mass fraction $\xi_\mathrm{g}^{\mathrm{O_2}}$,
- $\mathrm{H_2O}$ mass fraction $\xi_\mathrm{g}^{\mathrm{H_2O}}$,
- temperature T.

C
Dimensionless groups

To obtain the governing equations in non-dimensional form, each variable is consequently replaced by a dimensionless variable multiplied by a characteristic reference value, e.g. for an arbitrary variable $\tilde{s}$

$$\tilde{s} = \tilde{s}_r s \,, \tag{C.1}$$

where $\tilde{s}$, $\tilde{s}_r$ and s denote the dimensional, characteristic reference and dimensionless variable, respectively. The characteristic reference variables for each domain are listed in table 7.

$(\tilde{\cdot})_r$	GC, $a=1$		GDL, $a=2$		PEM
	cathode	anode	cathode	anode	
E_{cell}	-	-	-	-	E_{OC}
i	-	-	-	-	i_r
p	$\rho_{\text{air}} u_{1,\text{in}}^2$	$\rho_{\text{H}_2} u_{1,\text{in}}^2$	$\rho_{\text{air}} \dfrac{\mathcal{D}_{\text{O}_2,\text{H}_2\text{O}}^2}{H_{\text{GDL}}^2}$	$\rho_{\text{H}_2} \dfrac{\mathcal{D}_{\text{H}_2,\text{H}_2\text{O}}^2}{H_{\text{GDL}}^2}$	-
T	T_r	T_r	T_r	T_r	T_r
t	$\dfrac{L}{u_{1,\text{in}}}$	$\dfrac{L}{u_{1,\text{in}}}$	$\dfrac{H_{\text{GDL}}^2}{\mathcal{D}_{\text{O}_2,\text{H}_2\text{O}}}$	$\dfrac{H_{\text{GDL}}^2}{\mathcal{D}_{\text{H}_2,\text{H}_2\text{O}}}$	$\dfrac{H_{\text{PEM}}^2}{\mathcal{D}_{\text{w}}}$
u	$u_{1,\text{in}}$	$u_{1,\text{in}}$	$\dfrac{\mathcal{D}_{\text{O}_2,\text{H}_2\text{O}}}{H_{\text{GDL}}}$	$\dfrac{\mathcal{D}_{\text{H}_2,\text{H}_2\text{O}}}{H_{\text{GDL}}}$	-
x_a	L	L	H_{GDL}	H_{GDL}	H_{PEM}
$\mathcal{D}$	$\mathcal{D}_{\text{O}_2,\text{H}_2\text{O}}$	$\mathcal{D}_{\text{H}_2,\text{H}_2\text{O}}$	$\mathcal{D}_{\text{O}_2,\text{H}_2\text{O}}$	$\mathcal{D}_{\text{H}_2,\text{H}_2\text{O}}$	$\mathcal{D}_{\text{w}}$
M	M^{O_2}	M^{H_2}	M^{O_2}	M^{H_2}	-
μ	μ_{air}	μ_{H_2}	μ_{air}	μ_{H_2}	-
ρ	ρ_{air}	ρ_{H_2}	ρ_{air}	ρ_{H_2}	ρ_{PEM}
c_{p}	$c_{\text{p}}^{\text{air}}$	$c_{\text{p}}^{\text{H}_2}$	$c_{\text{p}}^{\text{air}}$	$c_{\text{p}}^{\text{H}_2}$	$c_{\text{p}}^{\text{PEM}}$
k	k_{air}	k_{H_2}	k_{s}	k_{s}	k_{PEM}
σ	-	-	-	-	σ_r

Table 7: Characteristic reference values used to obtain the dimensionless formulation of the governing equations. Since all entries are dimensional values, tilde is omitted for simplicity.

Commonly used dimensionless groups such as the Reynolds number Re, Schmidt number Sc and Péclet number Pe, as well as the density ratio between the gas and liquid phase are defined in table 8. The dimensionless groups that appear in the governing equations for the PEM, sec. 3.4, GC, sec. 3.2.1, and GDL domain, sec. 3.3.1, are listed in table 9, 10 and 11, respectively. Due to the orientation of the coordinate system, the dimensionless groups for the GC-GDL coupling fluxes in the GC conservation equations have a negative sign on the anode side. The numerical values of the dimensional groups are computed with the reference values from the validation, see table 5 and 12.

Dimensionless group	Value cathode	Value anode
$\mathrm{Re} = \dfrac{\tilde{u}_r\,\tilde{D}_\mathrm{H}\,\tilde{\rho}_r}{\tilde{\mu}_r}$	419	202
$\mathrm{Sc} = \dfrac{\tilde{\mu}_r}{\tilde{\mathcal{D}}_r\,\tilde{\rho}_r}$	611×10^{-3}	379.5×10^{-3}
$\mathrm{Pe}_\mathrm{GC} = \dfrac{\tilde{u}_{1,r}\,\tilde{L}}{\tilde{\mathcal{D}}_r}$	14.80×10^{3}	4.45×10^{3}
$\mathrm{Pe}_\mathrm{GDL} = \dfrac{\tilde{u}_{1,r}\,\tilde{H}_\mathrm{GDL}}{\tilde{\mathcal{D}}_r}$	83.68	25.16
$K_\rho = \dfrac{\tilde{\rho}_r}{\tilde{\rho}_\mathrm{l}}$	1×10^{-3}	235.6×10^{-6}

Table 8: Commonly used dimensionless groups.

Dimensionless group	Value
$K_\mathrm{mw} = \dfrac{\tilde{\mathrm{EW}}\,\tilde{t}_r\,C_{\mathrm{drag},r}\,\tilde{i}_r}{\tilde{\rho}_\mathrm{PEM}\,\tilde{F}\,\tilde{H}_\mathrm{PEM}}$	18.01
$K_\mathrm{me1} = \dfrac{\tilde{\mathrm{EW}}\,\tilde{c}_\mathrm{p}^\mathrm{PEM}}{\tilde{M}^{\mathrm{H_2O}}\,\tilde{c}_\mathrm{p}^\mathrm{w}}$	15.92
$K_\mathrm{me2} = K_\mathrm{mw}$	18.01
$K_\mathrm{me3} = \dfrac{\tilde{\mathrm{EW}}\,\tilde{t}_r\,\tilde{k}_r}{\tilde{M}^\mathrm{w}\,\tilde{\rho}_\mathrm{PEM}\,\tilde{c}_\mathrm{p}^\mathrm{w}\,\tilde{H}_\mathrm{PEM}^2}$	61.88×10^{3}
$K_\mathrm{me4} = \dfrac{\tilde{\mathrm{EW}}\,\tilde{t}_r\,i_r^2}{\tilde{M}^{\mathrm{H_2O}}\,\tilde{\rho}_\mathrm{PEM}\,\tilde{c}_\mathrm{p}^{\mathrm{H_2O}}\,\tilde{T}_r\,\tilde{\sigma}_r}$	9.562×10^{3}

Table 9: Dimensionless groups for the membrane domain.

Dimensionless group	Value cathode	Value anode
$K_{\mathrm{cm}}^{\mathrm{C}} = \dfrac{\tilde{W}_{\mathrm{GDL}}\,\tilde{L}}{\tilde{W}_{\mathrm{GC}}\,\tilde{H}_{\mathrm{GC}}}\dfrac{1}{\mathrm{Pe}_{\mathrm{GDL}}} = -K_{\mathrm{cm}}^{\mathrm{A}}$	1.568	−5.262
$K_{\mathrm{cl1}}^{\mathrm{C}} = \dfrac{\tilde{W}_{\mathrm{GDL}}}{\tilde{W}_{\mathrm{GC}}\,\tilde{H}_{\mathrm{GC}}}\dfrac{\tilde{L}}{\tilde{H}_{\mathrm{GDL}}}\dfrac{\sqrt{\varepsilon\tilde{\kappa}}\,\cos(\theta_{\mathrm{c}})\,\tilde{\varsigma}_{\mathrm{l}}}{\tilde{\rho}_{\mathrm{l}}\,\tilde{u}_{1,r}\,\tilde{\nu}_r} = -K_{\mathrm{cl1}}^{\mathrm{A}}$	57.4×10^{-3}	27.8×10^{-3}
$K_{\mathrm{cl2}}^{\mathrm{C}} = \dfrac{\tilde{W}_{\mathrm{GDL}}\,\tilde{L}}{\tilde{W}_{\mathrm{GC}}\,\tilde{H}_{\mathrm{GC}}}\dfrac{K_\rho}{\mathrm{Pe}_{\mathrm{GDL}}} = -K_{\mathrm{cl2}}^{\mathrm{A}}$	9.033×10^{-6}	-6.942×10^{-6}
$K_{\mathrm{cs1}}^{\mathrm{C,A}} = \dfrac{1}{\mathrm{Pe}_{\mathrm{GC}}}$	67.57×10^{-6}	224.7×10^{-6}
$K_{\mathrm{cs2}}^{\mathrm{C,A}} = K_{\mathrm{cm}}^{\mathrm{C,A}}$	1.568	5.216
$K_{\mathrm{ce1}}^{\mathrm{C,A}} = \dfrac{(\tilde{c}_{\mathrm{p}}^{\beta} - \tilde{c}_{\mathrm{p}}^{\mathrm{N_2}})}{\tilde{c}_{\mathrm{p},r}}\dfrac{1}{\mathrm{Pe}_{\mathrm{GC}}}$	-7.661×10^{-6}	208.5×10^{-6}
$K_{\mathrm{ce2}}^{\mathrm{C,A}} = \dfrac{(\tilde{c}_{\mathrm{p}}^{\mathrm{H_2O}} - \tilde{c}_{\mathrm{p}}^{\mathrm{N_2}})}{\tilde{c}_{\mathrm{p},r}}\dfrac{1}{\mathrm{Pe}_{\mathrm{GC}}}$	63.88×10^{-6}	14.87×10^{-6}
$K_{\mathrm{ce3}}^{\mathrm{C,A}} = \dfrac{\tilde{L}}{\tilde{H}_{\mathrm{GC}}}\dfrac{\tilde{\alpha}}{\tilde{\rho}_r\,\tilde{c}_{\mathrm{p},r}\,\tilde{u}_{1,r}}$	6.529	1.977
$K_{\mathrm{ce4}}^{\mathrm{C,A}} = \dfrac{\tilde{L}}{\tilde{W}_{\mathrm{GC}}}\dfrac{\tilde{\alpha}}{\tilde{\rho}_r\,\tilde{c}_{\mathrm{p},r}\,\tilde{u}_{1,r}}$	4.975	1.507
$K_{\mathrm{ce5}}^{\mathrm{C,A}} = \dfrac{\tilde{L}}{\tilde{H}_{\mathrm{GC}}}\dfrac{\tilde{\alpha}_{\mathrm{GDL}}}{\tilde{\rho}_r\,\tilde{c}_{\mathrm{p},r}\,\tilde{u}_{1,r}}$	6.529	1.977
$K_{\mathrm{ce6}}^{\mathrm{C,A}} = \dfrac{\tilde{\rho}_{\mathrm{l}}\,\Delta_{\mathrm{lv}}\tilde{H}}{\tilde{\rho}_r\,\tilde{c}_{\mathrm{p},r}\,\tilde{T}_r}$	6.427×10^{3}	1.946×10^{3}
$K_{\mathrm{ce7}}^{\mathrm{C}} = \dfrac{\tilde{W}_{\mathrm{GDL}}\,\tilde{L}}{\tilde{W}_{\mathrm{GC}}\,\tilde{H}_{\mathrm{GC}}}\dfrac{(\tilde{c}_{\mathrm{p}}^{\beta} - \tilde{c}_{\mathrm{p}}^{\mathrm{N_2}})}{\tilde{c}_{\mathrm{p},r}}\dfrac{1}{\mathrm{Pe}_{\mathrm{GDL}}} = -K_{\mathrm{ce7}}^{\mathrm{A}}$	-1×10^{-3}	-27.4×10^{-3}
$K_{\mathrm{ce8}}^{\mathrm{C}} = \dfrac{\tilde{W}_{\mathrm{GDL}}\,\tilde{L}}{\tilde{W}_{\mathrm{GC}}\,\tilde{H}_{\mathrm{GC}}}\dfrac{(\tilde{c}_{\mathrm{p}}^{\mathrm{H_2O}} - \tilde{c}_{\mathrm{p}}^{\mathrm{N_2}})}{\tilde{c}_{\mathrm{p},r}}\dfrac{1}{\mathrm{Pe}_{\mathrm{GDL}}} = -K_{\mathrm{ce8}}^{\mathrm{A}}$	8.4×10^{-3}	-2×10^{-3}
$K_{\mathrm{cu}}^{\mathrm{C,A}} = F_{\mathrm{c}}\dfrac{\tilde{L}}{\tilde{D}_{\mathrm{H}}}\dfrac{8}{\mathrm{Re}}$	1.104	2.28
$K_{\mathrm{ceos}} = \dfrac{\tilde{\mathcal{R}}\,\tilde{T}_r}{\tilde{u}_{1,r}^2\,\tilde{M}_r}$	917.6	14.57×10^{3}

Table 10: Dimensionless groups for the gas channel domain.

Dimensionless group	Value cathode	Value anode
$K_{\mathrm{gl}}^{\mathrm{C,A}} = \dfrac{\sqrt{\varepsilon\tilde{\kappa}}\,\cos(\theta_{\mathrm{c}})\,\tilde{\varsigma}_{\mathrm{l}}}{\tilde{\rho}_{\mathrm{l}}\,\tilde{\mathcal{D}}_r\,\tilde{\nu}_r}$	-36.6×10^{-3}	-5.3×10^{-3}
$K_{\mathrm{gs}}^{\mathrm{C,A}} = \dfrac{\sqrt{\varepsilon\tilde{\kappa}}\,\cos(\theta_{\mathrm{c}})\,\tilde{\varsigma}_{\mathrm{l}}}{\tilde{\rho}_r\,\tilde{\mathcal{D}}_r\,\tilde{\nu}_r}$	-35.93	-22.63
$K_{\mathrm{ge1}}^{\mathrm{C,A}} = \dfrac{\tilde{\rho}_{\mathrm{s}}\,\tilde{c}_{\mathrm{p,s}}}{\tilde{\rho}_r\,\tilde{c}_{\mathrm{p}}}$	192.6	58.34
$K_{\mathrm{ge2}}^{\mathrm{C,A}} = \dfrac{(\tilde{c}_{\mathrm{p}}^{\beta} - \tilde{c}_{\mathrm{p}}^{\mathrm{N_2}})}{\tilde{c}_{\mathrm{p},r}}$	-113.4×10^{-3}	927.7×10^{-3}
$K_{\mathrm{ge3}}^{\mathrm{C,A}} = \dfrac{(\tilde{c}_{\mathrm{p}}^{\mathrm{H_2O}} - \tilde{c}_{\mathrm{p}}^{\mathrm{N_2}})}{\tilde{c}_{\mathrm{p},r}}$	945.5×10^{-3}	66.3×10^{-3}
$K_{\mathrm{ge4}}^{\mathrm{C,A}} = \dfrac{\tilde{k}_r}{\tilde{\rho}_r\,\tilde{c}_{\mathrm{p},r}\,\tilde{\mathcal{D}}_r}$	50.07	4.559
$K_{\mathrm{ge5}}^{\mathrm{C,A}} = K_{\mathrm{ce6}}^{\mathrm{C,A}}$	6.427×10^3	1.946×10^3
$K_{\mathrm{ge6}}^{\mathrm{C,A}} = \dfrac{\sqrt{\varepsilon\tilde{\kappa}}\,\cos(\theta_{\mathrm{c}})\,\tilde{\varsigma}_{\mathrm{l}}}{\tilde{\rho}_r\,\tilde{\mathcal{D}}_r\,\tilde{\nu}_r}\,\dfrac{\tilde{c}_{\mathrm{p,l}}}{\tilde{c}_{\mathrm{p},r}}$	-148.8	-6.562
$K_{\mathrm{ge7}}^{\mathrm{C,A}} = K_{\mathrm{gs}}^{\mathrm{C,A}}$	-35.93	-22.63
$K_{\mathrm{gu1}}^{\mathrm{C,A}} = \dfrac{\tilde{H}_{\mathrm{GDL}}^2}{\tilde{\kappa}}\,\varepsilon\,\mathrm{Sc}$	29.3×10^3	18.20×10^3
$K_{\mathrm{gu2}}^{\mathrm{C,A}} = 2\,\mathrm{Sc}$	1.222	758.9×10^{-3}
$K_{\mathrm{geos}} = \dfrac{\tilde{\mathcal{R}}\,\tilde{T}_r\,\tilde{H}_{\mathrm{GDL}}^2}{\tilde{\mathcal{D}}_r^2\,\tilde{M}_r}$	6.426×10^6	9.221×10^6

Table 11: Dimensionless groups for the gas diffusion layer domain.

Note that the dimensional groups underestimate the effect of mass and enthalpy diffusion. The computed values for the binary diffusion coefficients are up to 10^4 times the chosen reference value $\tilde{\mathcal{D}}_{\mathrm{r}}$.

The hydraulic diameter $\tilde{D}_{\mathrm{H}}$ to calculate the Reynolds number Re for a rectangular duct is defined as, [1],

$$\tilde{D}_{\mathrm{H}} = \frac{2\tilde{H}_{\mathrm{GC}}\tilde{W}_{\mathrm{GC}}}{\tilde{H}_{\mathrm{GC}} + \tilde{W}_{\mathrm{GC}}}\,. \tag{C.2}$$

For details on the correction and shape factors, see also [1].

Parameter [unit], reference	Symbol	Value
PEMFC temperature [K], [24]	$\tilde{T}_r$	353.15
Inlet velocity [$\mathrm{m\,s^{-1}}$], (assumed)	$\tilde{u}_{1,r}$	10
Molar mass O_2 [$\mathrm{kg\,mol^{-1}}$], [6]	$\tilde{M}_{\mathrm{O_2}}$	31.9988×10^{-3}
Molar mass H_2 [$\mathrm{kg\,mol^{-1}}$], [6]	$\tilde{M}_{\mathrm{H_2}}$	2.016×10^{-3}
Dynamic viscosity air [Pa s], [6]	$\tilde{\mu}_{\mathrm{air}}$	20.56×10^{-6}
Dynamic viscosity H_2 [Pa s], [30]	$\tilde{\mu}_{\mathrm{H_2}}$	9.813×10^{-6}
Density air [$\mathrm{kg\,m^{-3}}$], [6]	$\tilde{\rho}_{\mathrm{air}}$	1.015
Density H_2 [$\mathrm{kg\,m^{-3}}$], [30]	$\tilde{\rho}_{\mathrm{H_2}}$	0.0706
Density liquid H_2O [$\mathrm{kg\,m^{-3}}$], [6]	$\tilde{\rho}_{\mathrm{l}}$	977.75
Density GDL matrix [$\mathrm{kg\,m^{-3}}$], (assumed)	$\tilde{\rho}_{\mathrm{s}}$	440
Specific heat capacity air [$\mathrm{J\,kg^{-1}\,K^{-1}}$], [6]	$\tilde{c}_{\mathrm{p}}^{\mathrm{air}}$	1009
Specific heat capacity H_2 [$\mathrm{J\,kg^{-1}\,K^{-1}}$], [30]	$\tilde{c}_{\mathrm{p_g}}^{\mathrm{H_2}}$	14 419
Specific heat capacity N_2 [$\mathrm{J\,kg^{-1}\,K^{-1}}$], [30]	$\tilde{c}_{\mathrm{p_g}}^{\mathrm{N_2}}$	1042
Specific heat capacity H_2O [$\mathrm{J\,kg^{-1}\,K^{-1}}$], [6]	$\tilde{c}_{\mathrm{p_g}}^{\mathrm{H_2O}}$	1987
Specific heat capacity liquid H_2O [$\mathrm{J\,kg^{-1}\,K^{-1}}$], [6]	$\tilde{c}_{\mathrm{p_l}}$	4188
Enthalpy of evaporation [$\mathrm{kJ\,kg^{-1}}$], [6]	$\Delta_{\mathrm{lv}}\tilde{H}$	2333
Specific heat capacity GDL matrix [$\mathrm{J\,kg^{-1}\,K^{-1}}$], (assumed)	$\tilde{c}_{\mathrm{p}}^{\mathrm{s}}$	890
Thermal conductivity air [$\mathrm{W\,m^{-1}\,K^{-1}}$], [6]	$\tilde{k}_{\mathrm{air}}$	0.029 51
Thermal conductivity H_2 [$\mathrm{W\,m^{-1}\,K^{-1}}$], [30]	$\tilde{k}_{\mathrm{H_2}}$	0.206 88
Binary diffusion coefficient O_2-H_2O [$\mathrm{m^2\,s^{-1}}$], [1]	$\tilde{\mathcal{D}}_{\mathrm{O_2-H_2O}}$	26.52×10^{-6}
Binary diffusion coefficient H_2-H_2O [$\mathrm{m^2\,s^{-1}}$], [1]	$\tilde{\mathcal{D}}_{\mathrm{H_2-H_2O}}$	112.36×10^{-6}
Surface tension liquid H_2O [$\mathrm{N\,m^{-1}}$], [6]	ς_{l}	64.48×10^{-3}
Contact angle [°], (assumed)	θ_{c}	120
Reference ionic conductivity [$\mathrm{S\,m^{-1}}$], (assumed)	σ_r	0.2
Reference current density [$\mathrm{A\,m^{-2}}$], [1]	$\tilde{i}_r$	14 000

Table 12: Reference values. Fluid properties for $\tilde{T} = 343.15\,\mathrm{K}$ and $\tilde{p} = 1\,\mathrm{bar}$.